Two-Stage DOA Estimation via Multi-Aperture FOCUSS in Distributed Radar Systems

M.Sc. Thesis

Ming Mo
Supervisor: Prof. Alexander Yarovoy, Rutkay Guneri

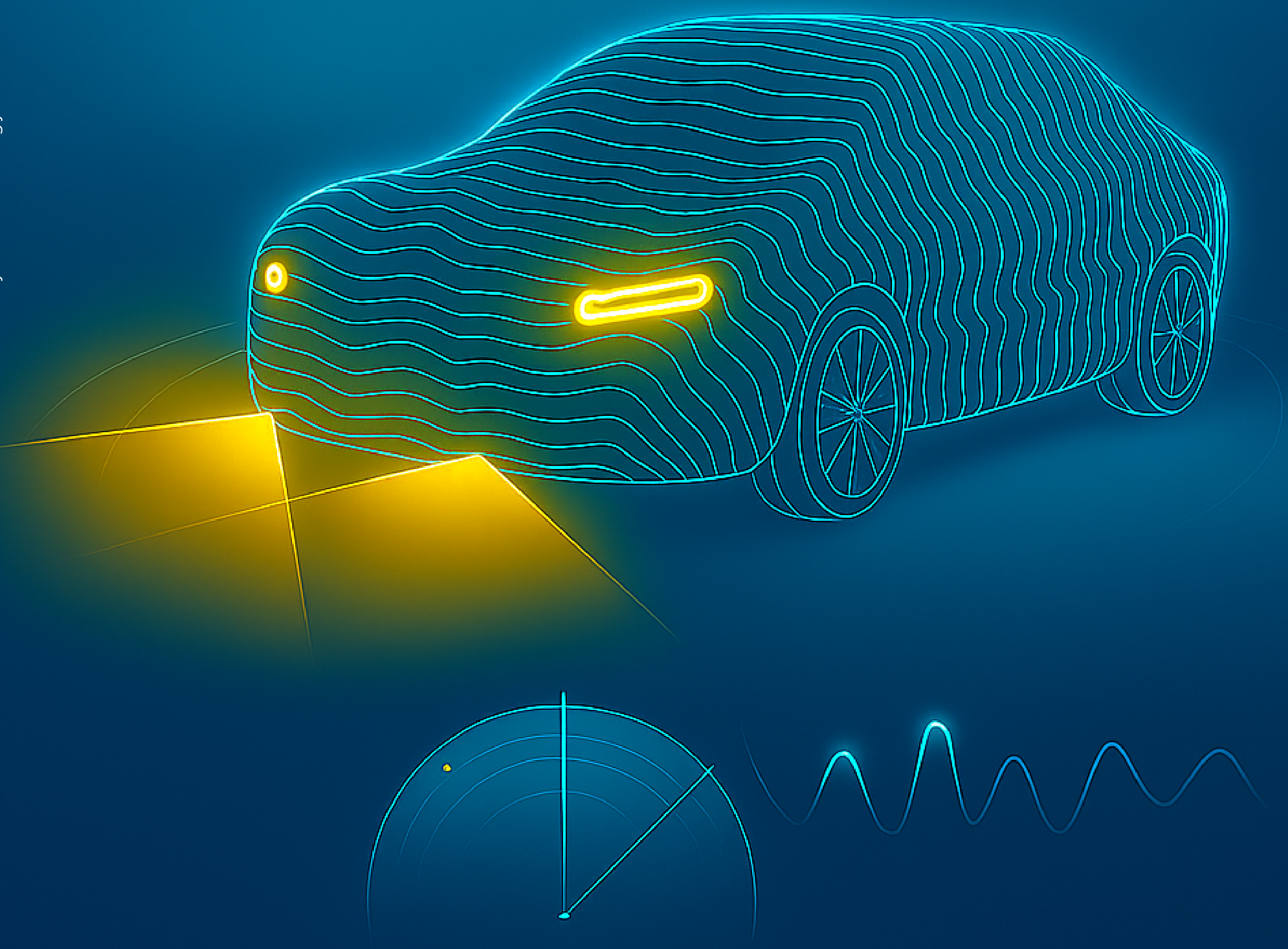

Delft University of Technology

TU Delft

Two-Stage DOA Estimation via Multi-Aperture FOCUSS in Distributed Radar Systems

M.Sc. Thesis

by

Ming Mo

Supervisor: Prof. Alexander Yarovoy

Daily Supervisor: Rutkay Guneri

Student Number:	5992095
Group:	Microwave Sensing, Signals and Systems (MS3)
Faculty:	Faculty Electrical Engineering, Mathematics and Computer Science
Project Duration:	February, 2025 – November, 2025
Thesis committee:	Prof. DSc. Alexander Yarovoy, TU Delft, supervisor
	Dr. Geethu Joseph, TU Delft
	Rutkay Guneri, TU Delft, daily supervisor

TU Delft

Preface

This thesis marks the completion of my Master's studies in the Wireless Communication and Sensing (WiCoS) track at Delft University of Technology. Throughout this journey, I have grown both academically and personally. Looking back, I am deeply grateful to all the individuals and institutions that have made this experience possible and meaningful.

First and foremost, I would like to express my heartfelt gratitude to my supervisors, Prof. Alexander Yarovoy and PhD researcher Rutkay Guneri. I am especially grateful to Prof. Yarovoy for proposing a research topic that was not only intellectually stimulating but also highly relevant to real-world applications. Despite his demanding schedule as the head of the MS^3 group, he generously devoted his time and attention to guiding my work. Our meetings were always concise, yet insightful, and his strategic vision played a crucial role in shaping the direction of this thesis.

I am equally grateful to Rutkay for his continuous and hands-on support throughout this project. From the early stages of formulation to the final stages of implementation and evaluation, Rutkay offered timely feedback, patiently helped me resolve complex technical issues, and ensured that I stayed on track. His dedication, depth of understanding, and clarity in communication have had a profound impact on both the quality of this thesis and my own growth as a researcher.

I would also like to thank the entire Microwave Sensing, Signals, and Systems (MS^3) group for providing a dynamic and collaborative research environment. The academic atmosphere of the group encouraged curiosity and independent thinking, while weekly seminars offered opportunities to engage in cutting-edge research. I particularly would like to acknowledge the PhD students in the group who kindly offered their time to answer my questions and discuss ideas—your guidance often led me past technical bottlenecks and inspired new directions.

My appreciation extends to TU Delft and the Faculty of Electrical Engineering, Mathematics and Computer Science (EEMCS), whose rigorous academic framework laid a solid foundation for my work. As someone who transitioned from a background in physics, I faced initial challenges in adapting to the interdisciplinary nature of this program. However, well-structured courses and hands-on projects, along with the support of instructors and peers, allowed me to bridge the knowledge gap and gain confidence in my abilities. The past two years of study have provided me with much more than I had anticipated—not just in terms of knowledge, but also in how I approach problems and conduct research.

I am also grateful to my friends and fellow students, whose companionship made this journey more enjoyable and less stressful. Late-night discussions, shared frustrations, and small victories were all part of a collective experience that I will always cherish.

Lastly, I owe my deepest thanks to my family. Your unwavering support—both emotional and financial—has been the foundation upon which I could pursue this path. Your belief in me has been a constant source of motivation, especially during moments of doubt and difficulty.

Ming Mo
Delft, November 2025

Abstract

This thesis investigates direction-of-arrival (DOA) estimation in a distributed MIMO FMCW automotive radar system consisting of two radar nodes that form four effective apertures (two mono-static and two bi-static). A two-stage DOA estimation framework is developed with the goal of achieving super-resolution accuracy while avoiding excessive computational burden. In the process of analyzing both non-coherent and coherent sparse reconstruction strategies, several key challenges are addressed, including aperture diversity, numerical instability in sparse recovery, inter-radar phase misalignment, and the severe sidelobe behavior induced by large distributed baselines.

In the first stage, coarse DOA estimates are obtained through conventional beamforming, followed by a range–velocity–geometry based data-association method that assigns the four aperture snapshots to the underlying physical targets. In the second stage, fine DOA estimation is performed using sparse reconstruction. Both non-coherent fusion (Block FOCUSS) and coherent fusion (phase-aligned FOCUSS) are examined, and the severe ill-conditioning induced by dense fine-angle grids is mitigated by three numerical remedies: adaptive extra regularization, a sparse virtual-array configuration, and a non-uniform angular grid. A complete phase-synchronization and geometric phase-compensation model is further derived to enable coherent stacking of the four apertures into a unified virtual array.

Simulation results demonstrate the contrasting behaviors of non-coherent and coherent reconstruction, revealing the benefits but also the instability of coherent processing when the baseline between radar nodes becomes large. In particular, the coherent virtual array exhibits severe sidelobe growth due to non-uniform element spacing. To address this issue, a modified array configuration is proposed based on controlled sparse spacing and embedded dense subarrays, which significantly suppresses sidelobes and improves coherent reconstruction stability.

Extensive Monte-Carlo simulations evaluate the framework under various DOA separations, ranges, SNR levels, RCS differences, and baseline lengths. The results show that the proposed methods achieve reliable data association and high angular resolution, while the modified configuration enables robust coherent processing even under large distributed baselines.

Contents

Nomenclature

Abbreviations

ADC	Analog-to-Digital Converter
AF	Ambiguity Function
BF	Beamforming
BEV	Bird's Eye View
BOMP	Block Orthogonal Matching Pursuit
BP	Basis Pursuit
BPDN	Basis Pursuit Denoising
CP	Chirp Processing
CS	Compressive Sensing
CSI	Channel State Information
DOA	Direction of Arrival
DOD	Direction of Departure
DTW	Detection Window
FA	False Alarm
FFT	Fast Fourier Transform
FMCW	Frequency Modulated Continuous Wave
FOCUSS	FOCal Underdetermined System Solver
FOV	Field of View
LSE	Least Squares Estimation
LOS	Line of Sight
MIMO	Multiple-Input Multiple-Output
MLW	Main Lobe Width
MSE	Mean Square Error
MMSE	Minimum Mean Square Error
PFA	Probability of False Alarm
PR	Probability of Resolution
PRI	Pulse Repetition Interval
PSD	Power Spectral Density
RCS	Radar Cross Section
RMSE	Root Mean Square Error

RV	Range-Velocity
SNR	Signal-to-Noise Ratio
SR	Sparse Recovery
ULA	Uniform Linear Array
V2X	Vehicle-to-Everything

Symbols

α	Chirp slope coefficient (B/T_c)
f_c	Carrier frequency of the radar waveform
B	Bandwidth of the FMCW chirp
T_c	Duration of each chirp
λ	Wavelength corresponding to f_c
τ	Round-trip delay
d	Inter-element spacing in ULA
d_m	Distance from origin to subarray m
N_r	Number of ADC samples per chirp
N_c	Number of chirps per frame
M	Number of radar subsystems
M_1, M_2	Radar node 1 and 2 respectively
N	Number of virtual elements per sensor
L	Number of total virtual apertures
R	Target range
v	Target radial velocity
K	Number of targets
θ	Target angle of arrival (AOA) in local coordinates
θ_g	DOA in global coordinates
$\phi(\theta)$	DOA relative to radar node M1
$\psi(\theta)$	DOA relative to radar node M2
$\mathbf{a}(\theta)$	Steering vector
$\mathbf{A}_p(\theta)$	Steering matrix at aperture p
$\mathbf{x}_p$	Local sparse spectrum at aperture p
$\mathbf{y}_p$	Measurement vector from aperture p
$\mathbf{n}_p$	Additive noise at aperture p
$\mathbf{A}(\theta)$	Stacked steering matrix for grid θ
$\mathbf{x}$	Global sparse angular spectrum
$\mathbf{y}$	Stacked observation vector
$\mathbf{G}$	Regularized Gram matrix

$\mathbf{R}_S$	Covariance of target signals
A	Complex amplitude of a target
$\Phi_p(\theta)$	Phase compensation term at aperture p
$\beta_p(\theta)$	Aperture-specific phase correction term
$\hat{\Delta}$	Estimated phase offset between radar nodes
N_{MC}	Number of Monte Carlo simulations
†	Moore-Penrose pseudo-inverse symbol

1
Introduction

1.1. Motivation

In current automotive radar technology, the range and velocity resolutions are already relatively satisfactory; however, there is considerable potential to improve the angular resolution without significantly increasing the hardware cost. Achieving high angular resolution is essential for automotive radar systems to enable precise object detection and tracking, especially in safety-critical scenarios such as lane change assistance, blind spot monitoring, and autonomous driving. For a uniform linear array (ULA), the angular resolution of 3 dB can be approximated by the following:

$$\Delta\theta \approx \frac{0.886\lambda}{D}, \tag{1.1}$$

where λ is the wavelength and L is the physical aperture length of the array. Applying this to a typical array working at 77 GHz, the angular resolution is approximately **8.44°**[1]. However, industrial applications for automotive radar typically require an angular resolution of around **1 °** [2, 3], which means that methods to improve angular resolutions are needed.

LiDAR is an alternative sensor that is used for autonomous driving. An angular resolution of approximately 0.1 ° could be achieved with long-range LiDAR sensors [4]. However, the use of LiDAR is expensive and highly sensitive to environmental conditions such as fog, rain, and dust. This greatly reduces reliability and makes it difficult to use in challenging weather conditions.

Several strategies have been explored to improve the angular resolution of an automotive radar, each presenting specific limitations.

- **Aperture Expansion:** Theoretical angular resolution improves with larger array apertures, but the physical space available in a vehicle severely limits feasible aperture sizes. For example, the far-field of a 77 GHz radar with **9.86 centimeters** aperture starts from 5 meters. Targets closer than 5 meters are in the near-field of the radar. This configuration results in an angular resolution of approximately **2 °**, which remains insufficient. In addition, increasing the physical aperture size requires more antenna elements, which directly leads to higher hardware cost. Therefore, physical aperture expansion is not a viable standalone solution.
- **High-Resolution Signal Processing (e.g., MUSIC, ESPRIT):** These methods provide enhanced resolution [5] under certain conditions but assume *non-correlated source signals*, which conflict with the nature of radar returns that are typically highly correlated. Therefore, these methods have certain limitations in improving the angular resolution of radar systems [6].

- **Operating at Higher Frequencies:** While higher carrier frequencies theoretically improve resolution, they also increase hardware complexity, propagation losses, and system cost, making them impractical for large-scale deployment in consumer vehicles.

Given these limitations, combining **bistatic radar configurations with sparse reconstruction (SR)** offers a promising alternative that can provide significantly higher resolutions with fewer limitations and costs [4, 7].

Sparse reconstruction has shown significant value in radar systems in several typical application domains—namely, **namely pulse compression**, **radar imaging**, and **DOA estimation** [8]. Among these, radar imaging and DOA estimation share key features: they benefit from **sparse signal representations**, rely on **dictionary-based models**, and aim to achieve **super-resolution** by applying similar algorithms.

However, as illustrated in Figure 1.1, the number of studies focused on **sparse reconstruction for the estimation of bi-static radar DOA** remains extremely limited compared to other combinations of key words such as SR + Imaging or SR + Radar. The intersecting area of all three keywords—*CS or SR*, *DOA*, and *bi-static*—contains only **8 papers**, highlighting a substantial research gap.

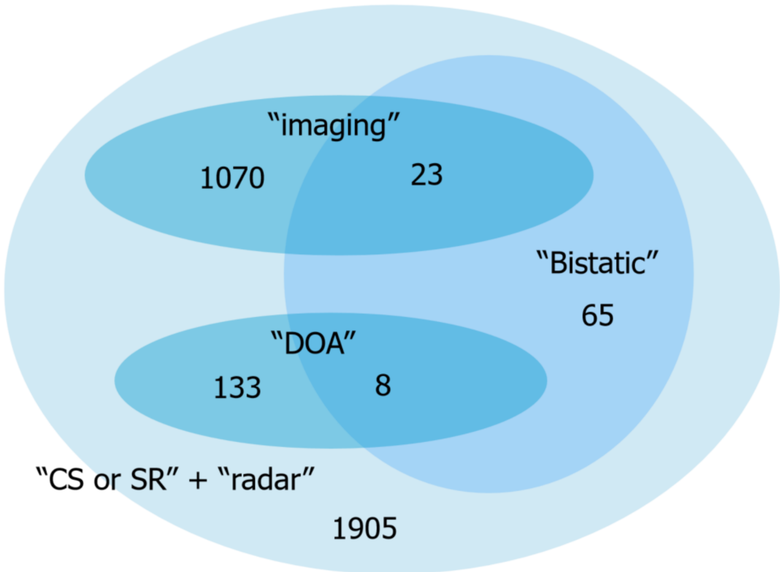

Figure 1.1: Venn diagram of paper counts under different key words combinations

The key features can be attributed to the following:

- **Bi-static vs. Mono-static Radar:**
  - More complex system geometry
  - Higher model dimension (DOD-DOA joint estimation)
  - Lack of unified dictionary and steering models
- **DOA Estimation vs. Radar Imaging:**
  - Higher sensitivity to off-grid and modeling errors
  - Require a higher resolution
  - Imaging tasks align better with grid-based SR frameworks

In summary, compared to traditional methods, the combination of sparse reconstruction and bistatic radar offers the potential for high angular resolution with reduced hardware cost and fewer spatial constraints. However, existing research in this area remains limited, and several challenges, such as model complexity and algorithmic robustness, still need to be addressed.

1.2. Literature Review

Automotive radar is widely used in driver assistance systems due to its robustness in poor weather and lighting conditions. Currently use direction-of-arrival (DoA) estimation methods, such as MUSIC and ESPRIT, have been extensively studied and achieve good performance, but they still face limitations in angular resolution.

Sparse reconstruction (SR) has emerged as a promising alternative, enabling high-resolution processing with fewer measurements. It has been applied in three main areas of radar: pulse compression, radar imaging, and DoA estimation. Among these, radar imaging and DoA estimation are most relevant to this work. SR-based methods in these areas will be reviewed in the following sections.

1.2.1. Current DOA Algorithms

Currently used advanced DOA estimation algorithms, particularly MUSIC and ESPRIT, have been widely applicated for their high-resolution capabilities. MUSIC estimates DOAs by exploiting the orthogonality between the noise subspace and the array steering vectors, identifying peaks in the resulting spatial spectrum. Although it offers high resolution, its performance degrades with coherent sources and incurs high computational cost, especially in multidimensional searches.

To address these issues, Belfiori [6] and Zhang [9] have proposed improved MUSIC-based approaches. Belfiori et al. targeted the problem of coherent sources and range-angle coupling in FMCW MIMO radar by introducing a coherent 2D MUSIC algorithm enhanced with spatial smoothing. In contrast, Zhang et al. focused on reducing the computational burden in bi-static MIMO radar by introducing a reduced-dimension MUSIC algorithm that decouples the 2D search into simpler subproblems. Although both methods aim to improve the practical applicability of MUSIC, they still inherit its sensitivity to coherent sources and structured array requirements.

ESPRIT-based methods provide an alternative by avoiding spectral search and directly estimating DOAs through algebraic operations. In [10], a 2D unitary ESPRIT algorithm has been proposed to jointly estimate DOD and DOA in bi-static MIMO radars, with the added benefit of automatic parameter pairing. Karmous [11] further improved ESPRIT to better handle coherent signals and low SNR environments, demonstrating sub-0.1° DOA estimation errors in simulation. Despite their improvements, both methods require strict array structures and remain sensitive to noise and snapshot limitations.

In summary, MUSIC and ESPRIT remain the foundational algorithms for DOA estimation, and recent work has improved their robustness and efficiency, as outlined in Table 1.1. However, shared limitations persist, including SNR sensitivity, limited array flexibility, and a general lack of explicit quantitative validation for angular resolution improvement. These limitations motivate the exploration of alternative frameworks, such as sparse reconstruction, which are discussed in the following sections.

Table 1.1: Comparison of DOA estimation methods under different physical models

References	Configuration	Methods	Advantages	Disadvantages
[6]	Monostatic ULA	MUSIC with spatial smoothing	• Handles coherent targets • Improved resolution	• Resolution degrades under low SNR or few snapshots • High complexity
[9]	bi-static ULA	Reduced-Dimension MUSIC		
[10]	bi-static ULA	2-D Unitary ESPRIT	• No spectral peak search required • Lower computational cost	• Less array flexibility • Less robust under low SNR or few snapshots
[11]	Monostatic ULA	Improved ESPRIT		

1.2.2. Sparse Reconstruction in DOA Estimation

Sparse reconstruction (SR) has emerged as an efficient method for estimating the direction of arrival (DOA), primarily by exploiting the inherent sparsity of radar signals in the spatial domain. Unlike traditional methods, SR algorithms can achieve super-resolution, robustness to coherent sources, and good performance with fewer antenna elements and snapshots.

In the context of bi-static radar systems, several studies have adopted Orthogonal Matching Pursuit (OMP) for its simplicity and computational efficiency. Chen [12] and Shoaib [13]'s study applied OMP to different bi-static array geometries: co-prime linear arrays and uniform circular arrays (UCA), respectively. Chen et al. demonstrated superior estimation performance by exploiting the larger virtual aperture provided by co-prime arrays, also deriving theoretical Cramér-Rao Lower Bounds (CRLB) to benchmark performance. Extending the practical validation of OMP, Shoaib et al. confirmed its robustness and good localization accuracy using real-field data in passive radar setups. However, their methods based on the OMP algorithm remain sensitive to prior knowledge of the sparsity level and limited resolution improvement compared to other SR methods.

Beyond OMP, other bi-static approaches utilize norm-based regularization techniques for sparse recovery. In Anusha's report [14], a Fusion FOCUSS algorithm for bi-static ULA configurations is proposed, based on an l_p-norm formulation with $0 < p < 1$. In parallel, Liu [15] employed LASSO, a convex optimization approach grounded in the l_1-norm, for bi-static MIMO radar with random arrays. Both methods aim to exploit sparsity to achieve high-resolution DOA estimation. While Fusion FOCUSS supports non-coherent processing across multiple sensors and offers improved resolution, Liu's model also enables velocity estimation, making it particularly relevant for dynamic automotive scenarios. However, they share common limitations: both are sensitive to parameter selection and noise, and LASSO, in particular, suffers from degraded performance in the presence of correlated dictionaries. In terms of computational behavior, the l_p-norm approach of FOCUSS can promote sparser solutions than LASSO, but this often comes at the cost of stability and robustness. Conversely, LASSO provides a more stable optimization path, but is generally more susceptible to dictionary structure and tuning challenges.

In the mono-static radar context, more recent developments have focused on enhancing robustness and computational efficiency. Roldan [16] introduced a sectorized Bayesian SR method based on the relevance vector machine (RVM) for the single-snapshot DOA estimation. Their method significantly reduced computational cost while preserving high resolution but was affected by estimation errors near the boundaries between angular sectors and showed sensitivity to noise. Complementarily, in [17], a group-sparse ADMM-based SR approach is proposed that improves robustness under low-SNR conditions by incorporating prior scene information into the design of both transmitter and receiver. Although high accuracy is achieved, the dependence of this method on accurate priors and relatively high complexity can limit its adaptability to rapidly changing environments.

In summary, SR-based methods in DOA estimation offer clear advantages over traditional techniques, including improved angular resolution, reduced hardware complexity, and robustness to coherent signals and limited snapshots , as highlighted in Table 1.2. However, challenges such as sensitivity to parameter selection, the integration of non-coherent scenarios, and velocity estimation capabilities remain open research areas. Addressing these issues is key to the advancement of practical automotive radar applications.

Table 1.2: Comparison of SR applications in DOA estimation

<table>
<tr><th>References</th><th colspan="2">Configuration</th><th>Methods</th><th>Advantages</th><th>Disadvantages</th></tr>
<tr><td>[12]</td><td rowspan="4">bi-static</td><td>ULA</td><td>FOCUSS</td><td>• High resolution
• Feasibility of non-coherent processing</td><td>• Sensitive to noise and parameter selection</td></tr>
<tr><td>[13]</td><td>Random arrays</td><td>LASSO</td><td>• High resolution
• Velocity estimation feasible</td><td>• Sensitive to parameter selection
• Poor Performance with Correlated Dictionaries</td></tr>
<tr><td>[14]</td><td>Co-prime array</td><td>OMP</td><td rowspan="2">• Low complexity
• Suitable for real data</td><td rowspan="2">• Limited resolution
• Needs prior for sparsity
• Noise sensitive</td></tr>
<tr><td>[15]</td><td>UCA passive radar</td><td>OMP</td></tr>
<tr><td>[16]</td><td rowspan="2">Monostatic</td><td>ULA</td><td>Sectorized BCS (based on RVM)</td><td>• High resolution
• Faster convergence</td><td>• Edge leakage between sector
• Noise sensitive</td></tr>
<tr><td>[17]</td><td>ULA</td><td>Group sparse ADMM</td><td>• High accuracy
• Improved robustness under low-SNR condition</td><td>• Sensitive to target priors
• Higher complexity</td></tr>
</table>

1.2.3. Sparse Reconstruction in Radar Imaging

Sparse reconstruction has attracted growing interest in radar imaging due to its ability to reconstruct high-resolution images from fewer measurements by exploiting sparsity. Compared to traditional methods, SR-based techniques offer reduced system complexity, improved resolution, and greater robustness under sparse aperture or multipath conditions.

In [18] and [19], resolution degradation in bi-static radar imaging is tackled. The former proposed a Fast Smoothed L0 (FSL0) algorithm for 3D imaging on bi-static MIMO radar, enhancing resolution with fewer antennas. The latter addressed bi-static ISAR imaging under sparse apertures using Regularized Orthogonal Matching Pursuit (ROMP). Both methods used sparsity to reduce sidelobes and improve image quality. FSL0 improved efficiency through prior-based region selection, while ROMP showed better robustness under data loss. However, FSL0 depended on accurate prior thresholds, and ROMP remained sensitive to noise.

Abdalla and Muqaibel [20] proposed a ghost suppression method for through-the-wall radar imaging (TWRI), using a SR-based bi-static setup and exploiting the aspect-dependent characteristics of multi-path ghosts. A weighted fusion of sub-aperture measurements was used to distinguish real targets from ghosts. The approach avoided reliance on detailed knowledge of the scene. However, its performance drops when the aspect diversity is limited, such as in narrow-view or restricted environments.

Lu [21] presented a 2D hybrid OMP algorithm for mono-static SAR imaging using FMCW radar. Modeling the scene as a 2D sparse matrix, the method significantly reduced memory and computation compared to 1D OMP, while maintaining high resolution. However, it remained sensitive to dictionary coherence and parameter tuning.

In summary, SR-based radar imaging methods demonstrate strong capabilities in improving resolution and operating under reduced data conditions as emphasized in Table 1.3. Common advantages include robustness to sparse sampling and lower computational load. However, most methods remain sensitive to noise, parameter selection, and prior assumptions. Furthermore, similar to CS-based DOA estimation, few studies address incoherent processing strategies, which limits their applicability in multisensor or distributed systems. These gaps present opportunities for more flexible and adaptive SR imaging frameworks.

Table 1.3: Comparison of sparse reconstruction methods in radar imaging

References	Configuration	Methods	Advantages	Disadvantages
[18]	bi-static ULA	Fast SL0	• High resolution • Robust to noise • Real-time capability	• Sensitive to grid resolution and initial region selection
[19]	bi-static ULA	ROMP (Regularized OMP)	• High resolution • Better sidelobe suppression	• Sensitive to sparsity setting and noise
[20]	bi-static ULA	YALL1	• Effective ghost suppression • Reduce measurement samples	• High complexity • Sensitive to parameter selection
[21]	Monostatic SAR	2D hybrid OMP	• Reduces sidelobes • Clearly resolves weak targets	• Needs prior sparsity • Sensitive to noise

1.2.4. Summary

Based on the reviewed literature, the main findings and limitations of SR-based radar imaging and DOA estimation methods can be summarized as follows.

Key Advantages

- **High angular resolution**: SR methods can surpass classical resolution limits by exploiting signal sparsity.
- **Tolerance to source coherence**: Unlike subspace methods, SR handles coherent signals effectively.
- **Reduced hardware and data requirements**: Accurate estimation is achievable with fewer sensors and snapshots.

Common Limitations

- **Parameter sensitivity**: Performance depends heavily on prior settings (e.g., sparsity level, regularization, noise variance).
- **Noise vulnerability**: Many methods are less robust under low SNR or correlated noise.
- **Computational complexity**: Some algorithms (e.g., nonconvex solvers) are too slow for real-time use.

Open Problems

- **Lack of coherent fusion**: Most studies remain at the signal processing of a single aperture and lack the processing of multiple apertures either coherent or incoherent.
- **Lack of utilization of velocity information**: Current DOA studies mainly rely on fast-time snapshots, overlooking Doppler information that could support data association.
- **Limited resolution evaluation**: Most studies lack a quantitative evaluation of angular resolution and the few report only modest gains (1°–5°), which are still insufficient.

In general, commonly used SR algorithms can be categorized into four classes: greedy algorithms (e.g. OMP), convex optimization methods (e.g. LASSO), Bayesian approaches (e.g. SBL, RVM) and iterative reweighted methods (e.g., FOCUSS, FSL0). Each category exhibits different trade-offs in terms of computational complexity, resolution performance, and robustness to parameter selection.

Based on the literature review, their overall performance is summarized in Table 1.4. Greedy algorithms are computationally efficient but less accurate and sensitive to sparsity settings. Convex methods provide a balance between speed and resolution, but require careful tuning of regularization parameters. Bayesian methods achieve the highest accuracy, but suffer from high complexity and parameter dependence. Iterative reweighted algorithms offer strong resolution with moderate robustness and acceptable speed.

Table 1.4: Comparison of SR Algorithm Types in Computation, Accuracy, and Parameter Robustness

Algorithms	**Complexity (Speed)**	**Accuracy (Resolution)**	**Parameter Sensitivity**
Greedy	★★★★☆(Fastest)	★★☆☆☆(Moderate)	★★☆☆☆(Sensitive to K)
Convex Optimization	★★★☆☆(Efficient)	★★★☆☆(Good)	★☆☆☆☆(Very sensitive to λ)
Bayesian Methods	★★☆☆☆(Slower)	★★★★★(Very High)	★★★☆☆(Moderate)
Iterative Reweighted	★★☆☆☆(Slower)	★★★★☆(High)	★★★★☆(Relatively robust)

1.3. Objective and Novelty

This thesis aims to develop a robust and high-resolution angle estimation framework for dual-node automotive FMCW MIMO radar systems. By leveraging both mono-static and bi-static channels formed between two radar nodes, we propose a multi-aperture DOA estimation architecture that enables coherent or incoherent information fusion under a single-snapshot setting.

The core objective is to realize a two-stage DOA estimation pipeline:

- First, a coarse DOA estimation is obtained independently from each aperture using conventional beamforming. Based on the joint range and velocity consistency, single-snapshot four-tuples are associated across the four apertures.
- Then, a fine-grained sparse DOA estimation is performed on a high-resolution angular grid within a narrowed field of view, unified across all apertures via global coordinate mapping.

Two distinct fusion strategies are examined:

- An **incoherent model**, in which phase synchronization between radar nodes is not required. Each aperture constructs its own measurement equation and they are fused via a block-sparse model using block-FOCUSS:
$$\mathbf{y}_p = \mathbf{A}_p(\theta_g)\mathbf{x}_p, \quad p = 1, 2, 3, 4 \tag{1.2}$$
- A **coherent model** assuming strict phase synchronization. All virtual apertures are coherently aligned and concatenated into a single joint sparse recovery model.
$$\mathbf{y} = \begin{bmatrix} \mathbf{y}_1 \\ \mathbf{y}_2 \\ \mathbf{y}_3 \\ \mathbf{y}_4 \end{bmatrix}, \quad \mathbf{A} = \begin{bmatrix} \mathbf{A}_1(\theta_g) \\ \mathbf{A}_2(\theta_g) \\ \mathbf{A}_3(\theta_g) \\ \mathbf{A}_4(\theta_g) \end{bmatrix}, \quad \mathbf{y} = \mathbf{A}\mathbf{x} \tag{1.3}$$

The main novelties of this work are summarized as follows:

1. A snapshot-level four-tuple association mechanism is proposed, which integrates coarse DOA, range, and velocity features to associate measurements across four apertures. Unlike traditional radar-track-based data fusion methods that rely on temporal coherence, this strategy enables multi-aperture integration based on a single snapshot, addressing a relatively underexplored gap in current literature.
2. A refined sparse DOA estimation strategy is developed within a narrow and high-resolution field-of-view (FOV), using the FOCUSS algorithm. This work investigates multiple solutions to numerical instabilities inherent to fine-grid reconstruction, including adaptive regularization, sparse array configuration and grid conditioning strategies.
3. A robust phase alignment framework is formulated for coherent processing in distributed radar systems. It combines automatic inter-node phase synchronization with geometry-aware per-aperture phase compensation, yielding a unified model that ensures angular alignment across virtual apertures under practical system constraints.
4. A novel large-baseline coherent aperture fusion model is proposed to suppress sidelobes while preserving high angular resolution. This framework exploits the resolution benefits of extended aperture while mitigating the sidelobes commonly induced by large inter-node spacing.
5. A two-stage DOA estimation framework is used, from coarse beamforming to fine sparse recovery. Unlike conventional two-stage designs, this structure directly supports snapshot-level association,

accurate angular pre-localization, and low-sidelobe support for subsequent large-aperture coherent processing.

1.4. Research Framework and Thesis Outline

1.4.1. Research Framework

The general research framework of this thesis is shown in Fig. 1.2. The proposed system aims to achieve accurate and high-resolution DOA estimation for automotive radar networks using both mono-static and bi-static apertures.

First, the FMCW signals received from the four apertures (M1→M1, M2→M2, M1→M2, M2→M1) are dechirped to obtain the baseband beat signals. A three-dimensional data cube (fast time $\times$ slow time $\times$ virtual channels) is then constructed for each aperture, from which range–velocity maps are generated via 2-D FFT processing.

Next, a coarse estimate of DOA is performed on each range-velocity band using a conventional beamforming method. The coarse DOA results, together with range and Doppler information, are used in the **data association** stage to identify and group the four snapshots corresponding to the same physical target state.

After data association, two fine DOA estimation branches are implemented:

- **Block-FOCUSS Non-Coherent Estimation:** Each aperture is processed independently, and the results are fused using a block-sparse FOCUSS algorithm. This method does not require strict phase alignment between radar systems, providing a computationally efficient baseline for comparison.
- **Coherent-FOCUSS Estimation with Phase Compensation:** First, a phase synchronization step is performed to estimate the unknown intersystem phase offset. Then, a dedicated **phase compensation** stage is applied according to the path length difference between the apertures to align the phase references. Once phase alignment is achieved, the virtual arrays of all apertures are coherently stacked, forming an extended virtual aperture. Sparse reconstruction is finally performed using the FOCUSS algorithm on a fine-angular grid, yielding improved angular resolution and robustness.

This two-stage framework, coarse DOA estimation with data association, followed by fine sparse reconstruction with optional coherent combination, ensures good resolution and robust DOA estimation even for closely spaced targets.

Overall, the proposed framework provides a complete solution for high-resolution and robust target localization in multi-target scenarios.

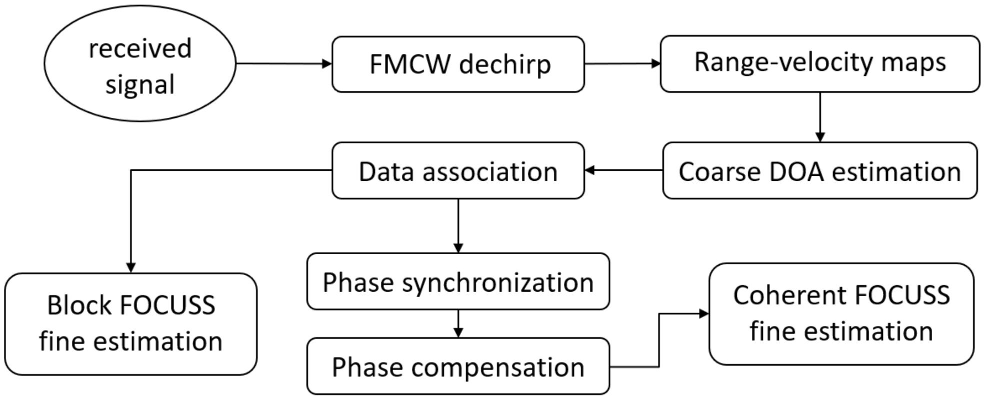

Figure 1.2: Research framework

1.4.2. Thesis Outline

This thesis is organized into six main chapters followed by the final conclusion.

Chapter 2 introduces the distributed FMCW radar architecture considered in this work and develops the corresponding signal and array models. The mono-static and bi-static virtual apertures are defined, the near-field/far-field assumptions are clarified, and a unified multi-aperture measurement model is derived as the basis for subsequent processing.

Chapter 3 describes the signal pre-processing chain and the coarse stage of the proposed two-stage framework. It covers dechirping, 2-D FFT range–velocity processing, and snapshot extraction from the RV map. Conventional Bartlett beamforming is then applied to obtain coarse DOA estimates, which are transformed into the global coordinate system and used, together with range and velocity information, in the multi-aperture data-association procedure.

Chapter 4 presents the complete non-coherent fine-estimation branch based on Block FOCUSS. The sparse reconstruction model for DOA estimation is formulated in the global coordinate system, followed by a detailed description of the FOCUSS and Block FOCUSS algorithms. The chapter then analyzes numerical instability issues caused by dense angular grids and introduces three remedies: adaptive regularization, sparse array configuration, and a non-uniform angle axis. Finally, Monte-Carlo simulations are conducted to evaluate the non-coherent model under different ranges, SNR levels, and other conditions.

Chapter 5 develops the coherent fine-estimation branch using phase-aligned FOCUSS. A modified topology and phase-compensated steering matrices are introduced, and a coherent stacked observation model is formulated. A phase-synchronization framework is derived and analyzed, including the π-ambiguity issue, followed by numerical and simulation results. The chapter also investigates the angular ambiguity function of the coherent virtual array and compares coherent and non-coherent performance under varying ranges, SNR levels, RCS differences, and baseline lengths.

Chapter 6 addresses a key practical challenge that arises when the inter-radar baseline becomes large: severe sidelobes in the coherent DOA spectrum. The angular ambiguity function is studied for different inter-element spacings, and the relation between grating lobes and array spacing is analyzed. Based on these insights, a modified array configuration is proposed that combines sparse spacing with embedded dense subarrays to compress sidelobes while avoiding grating lobes within the fine-estimation field of view. The performance of this configuration is then evaluated through simulations.

Finally, Chapter 7 summarizes the main findings of the thesis, discusses the limitations of the current work, and outlines possible directions for future research.

1.5. Conclusion

This chapter has introduced the motivation and context of this thesis, emphasizing the challenges of DOA estimation in distributed bistatic MIMO FMCW radar systems and the need for high-resolution yet computationally feasible processing frameworks. The limitations of conventional single-aperture beamforming, the complications introduced by bistatic Doppler inconsistencies, and the difficulty of performing coherent processing across spatially separated radars have been outlined.

To address these issues, a two-stage DOA estimation framework has been proposed, combining coarse beamforming with sparse-reconstruction-based fine estimation. The key research questions, contributions, and technical challenges—including aperture diversity, numerical instability in coherent sparse recovery, phase synchronization, and large-baseline sidelobe behavior—have been identified and discussed.

The remainder of the thesis develops the proposed methodology in detail, presents a comprehensive simulation-based evaluation, and investigates a modified array configuration that enables stable coherent processing under large distributed baselines.

2

System and Signal Model

This chapter establishes the foundation of the proposed research by describing the configuration of the radar system, the modeling assumptions, and the signal formulation. It specifies the spatial layout of the mono-static and bi-static apertures, clarifies the near-field or far-field conditions under which the analysis is valid, and derives the mathematical model of the received FMCW signals. These definitions and assumptions provide a consistent framework for the subsequent algorithm design and performance evaluation.

2.1. Radar System Configuration

The radar network considered in this work consists of two radar nodes, denoted M1 and M2, forming a distributed sensing system. Each node includes 3 transmitters and 4 receivers, creating two mono-static apertures (M1→M1, M2→M2) and two bi-static apertures (M1→M2, M2→M1). The geometric configuration is illustrated in Fig. 2.1, where R_1 and R_2 denote the propagation distances from the target to M1 and M2, respectively, and φ and ψ represent the corresponding arrival angles.

The system employs a frequency modulated continuous wave radar (FMCW) operating at a carrier frequency of $f_0 = 77$ GHz. Each radar transmits linear chirps of duration T_{chirp}, bandwidth B, and slope $k = B/T_{\text{chirp}}$. The received signal is sampled with N_r fast-time samples per chirp and N_c chirps per coherent processing interval (CPI), forming a three-dimensional signal cube for subsequent range, Doppler and angle processing[22]. The key system parameters are summarized in Table 2.1.

Table 2.1: Key radar system parameters

Parameter	Symbol	Value	Parameter	Symbol	Value
Speed of light	c	3×10^8 m/s	Wavelength	λ	c/f_0
Carrier frequency	f_0	77 GHz	FMCW bandwidth	B	200 MHz
Number of fast-time samples	N_r	4000	Number of chirps	N_c	400
Chirp slope	k_s	B/T_{chirp}	Chirp duration	T_{chirp}	10 μs
Number of transmitter	M_{Tx}	3	Number of receiver	M_{Rx}	4
Baseline length	L	20λ			

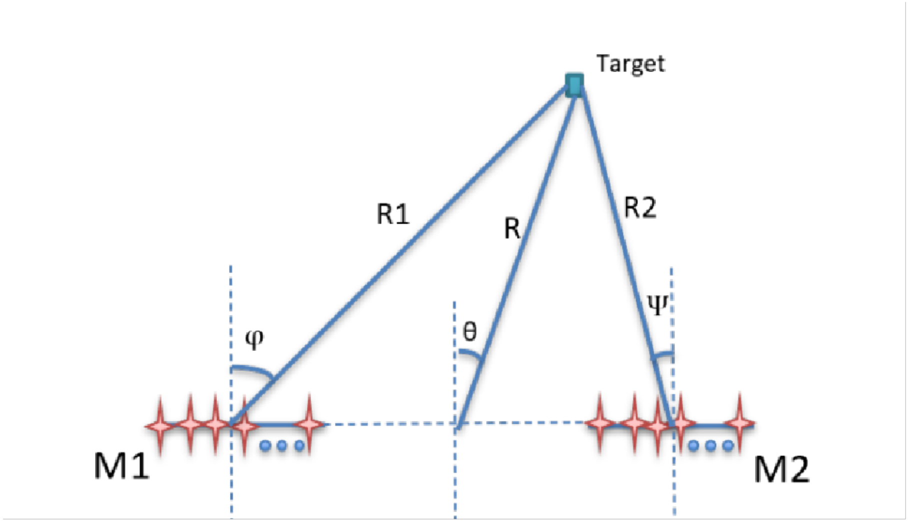

Figure 2.1: General system configuration

In the MIMO radar considered, *virtual array* is obtained by combining each transmitter-receiver pair. The position of each virtual element is given by the sum of the corresponding transmitter and receiver coordinates:

$$\mathbf{d}_v(i,j) = \mathbf{d}_{\text{tx}}(i) + \mathbf{d}_{\text{rx}}(j), \tag{2.1}$$

where $\mathbf{d}_{\text{tx}}(i)$ and $\mathbf{d}_{\text{rx}}(j)$ denote the physical positions of the i-th transmitter and the j-th receiver, respectively. This construction results in an extended aperture, as illustrated in Fig. 2.2.

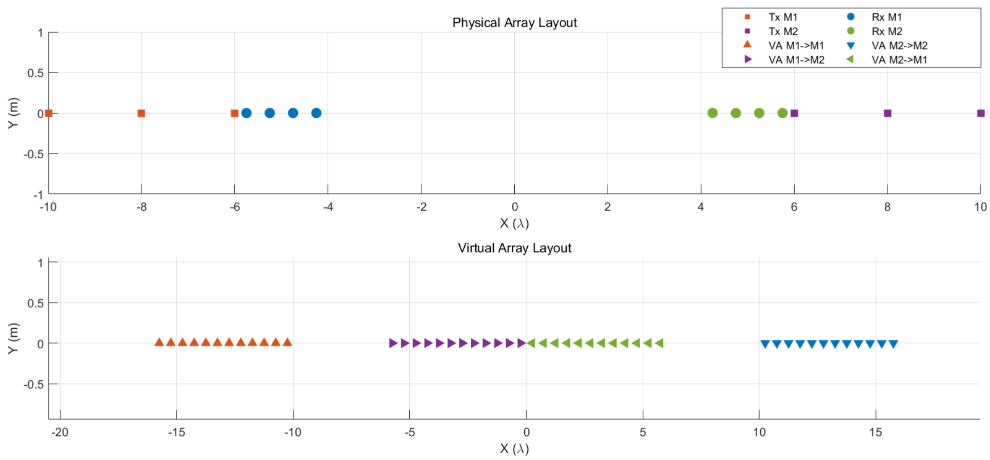

Figure 2.2: Physical and virtual array configurations

2.2. Nearfield and Farfield Assumption

In a MIMO radar system, the distinction between far-field and near-field conditions is critical for accurate modeling. Condition *far-field* is typically defined by the Fraunhofer distance.

$$R \geq R_{\text{F}} = \frac{2D^2}{\lambda}, \tag{2.2}$$

where D is the physical aperture size and λ is the radar wavelength. When this condition holds, the wavefront can be considered planar over the array aperture, and the received phase at each element can be expressed as

$$\phi_n \approx -\beta\, d_n \sin\theta, \tag{2.3}$$

where d_n is the position of the n-th element relative to the reference point of the matrix, and $\beta = 2\pi/\lambda$ is the wavenumber.

If $R < R_{\mathrm{F}}$, condition *near-field* applies, and the spherical nature of the wavefront must be preserved:

$$r_n = \sqrt{R^2 + d_n^2 - 2Rd_n \sin\theta}, \qquad \phi_n = -\beta r_n, \tag{2.4}$$

Near-field Modification Although for far-field scenarios it is common to use the center of an array as a reference for distance and angle computation, this approximation may introduce small range errors that translate into significant phase errors at 77 GHz. In our work, where coherent FOCUSS processing is performed, even a fractional-wavelength phase mismatch can severely degrade coherent integration. To avoid this issue, we compute distances and angles using the exact geometric path from *first transmitter* to *first receiver*, i.e.,

$$r_{\mathrm{ref}} = \|\mathbf{d}_{\mathrm{tx},1} - \mathbf{p}_{\mathrm{target}}\| + \|\mathbf{d}_{\mathrm{rx},1} - \mathbf{p}_{\mathrm{target}}\|, \tag{2.5}$$

The reference points of the two radar systems can be approximated as the centers of the first transmitter and the first receiver, so that the progressive phase of each array would be in the same direction. In this case, the distances from the origin of the two radars $L1, L2$ are no longer equal, shown in Fig. 2.3. In the DOA estimation, wavefront is still considered planar, and progressive phase differences between elements are still assumed to be uniform[23].

This near-field modification across radar systems is mandatory when coherent processing is used because phase synchronization across multiple arrays relies on accurate path-length differences. For non-coherent processing, the far-field approximation is typically sufficient.

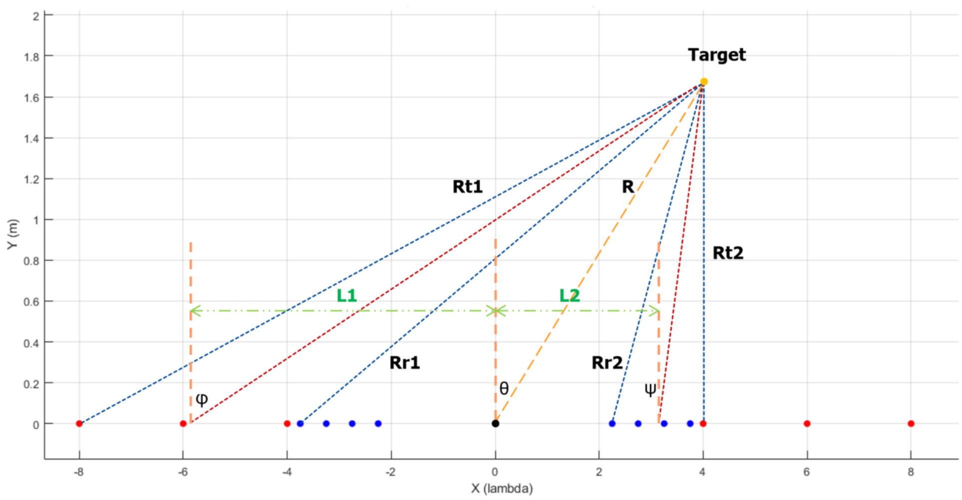

Figure 2.3: Geometric illustration of near-field modification.

2.2.1. Signal Model

Transmit FMCW waveform

In frequency modulated continuous-wave radar (FMCW), the transmitter emits a sequence of linear frequency modulated (LFM) chirps. This waveform enables simultaneous range and velocity estimation through beat frequency analysis. The baseband equivalent of a single up-chirp is mathematically described as

$$s_{\mathrm{tx}}(t) = \exp\left\{ j2\pi\Big(f_0 t + \frac{k_s}{2}t^2\Big) \right\}, \qquad 0 \le t < T_{\mathrm{chirp}}, \tag{2.6}$$

where f_0 denotes the carrier frequency (typically $77\ \mathrm{GHz}$ for automotive radar), T_{chirp} is the duration of the chirp and $k_s = B/T_{\mathrm{chirp}}$ is the slope of the chirp determined by the bandwidth B. The larger bandwidth B leads to a finer range resolution $\Delta R = c/(2B)$. The entire coherent processing interval (CPI) consists of N_c consecutive chirps, each separated by a pulse repetition interval (PRI) equal to T_{chirp}. Stacking multiple chirps within a CPI allows Doppler processing and thus velocity estimation of moving targets.

Multi-target received signal

Consider K point targets located at positions $\mathbf{p}_k(m)$ during the m-th transmitted chirp. For a given aperture p (corresponding to a specific transmitter–receiver pair) and receive channel q, the total round-trip propagation path length is

$$R_{p,k}(m,q) = \big\|\mathbf{p}_k(m) - \mathbf{d}_{\mathrm{tx}}^{(p)}\big\| + \big\|\mathbf{p}_k(m) - \mathbf{d}_{\mathrm{rx}}^{(p)}(q)\big\|, \tag{2.7}$$

where $\mathbf{d}_{\mathrm{tx}}^{(p)}$ and $\mathbf{d}_{\mathrm{rx}}^{(p)}(q)$ represent the positions of the p-th transmitter and the q-th receiver element, respectively. The corresponding two-way propagation delay is

$$\tau_{p,k}(m,q) = \frac{R_{p,k}(m,q)}{c}, \tag{2.8}$$

where c is the speed of light. For a target with constant radial velocity, the delay evolves over slow time m as

$$\tau_{p,k}(m,q) = \frac{1}{c}\Big(R_{p,k,0}(q) + 2v_k m T_{\mathrm{c}}\Big), \tag{2.9}$$

where $R_{p,k,0}(q)$ is the initial bistatic path length, v_k is the radial velocity of target k, and T_{c} is the chirp repetition interval. Thus, target motion is implicitly included through the m-dependent delay $\tau_{p,k}(m,q)$, which later generates Doppler modulation across chirps.

The received passband (RF) signal at channel q of aperture p before dechirping is modeled as a superposition of K delayed and scaled replicas of the transmitted chirp:

$$\begin{aligned} y_{p,q}(t,m) &= \sum_{k=1}^{K} \alpha_{p,q,k}\, s_{\mathrm{tx}}\big(t - \tau_{p,k}(m,q)\big) + w_{p,q}(t,m) \\ &= \sum_{k=1}^{K} \alpha_{p,q,k}\, \exp\Big\{ j2\pi \Big[f_0(t-\tau_{p,k}(m,q)) + \tfrac{k_s}{2}\,(t-\tau_{p,k}(m,q))^2 \Big] \Big\} + w_{p,q}(t,m), \end{aligned} \tag{2.10}$$

where $\alpha_{p,q,k} \in \mathbb{C}$ denotes the complex scattering coefficient of target k, incorporating its RCS, free-space propagation loss, and reflection-induced phase change. The term $w_{p,q}(t,m)$ represents additive receiver noise.

The dechirped (IF) signal used for range–Doppler processing is obtained by mixing $y_{p,q}(t,m)$ with the conjugated transmit chirp:

$$z_{p,q}(t,m) = y_{p,q}(t,m)\, s^{*}_{\mathrm{tx}}(t), \tag{2.11}$$

which yields the standard FMCW beat signal model. This IF signal forms the basis for the subsequent range FFT, Doppler FFT, and DOA estimation stages.

Array manifold and steering vectors

We now formalize the array manifold for each aperture. Let $\beta = 2\pi/\lambda$ be the wavenumber. For a 1D ULA oriented along the x-axis, the phase at an element located at the abscissa d for a plane wave originating from elevation θ is $-\beta\, d \sin\theta$.

Mono-static (single-sensor) manifold

Consider aperture p operating in mono-static mode, with transmit element positions collected in $\mathbf{d}^{(p)}_{\mathrm{Tx}}$ and receive element positions in $\mathbf{d}^{(p)}_{\mathrm{Rx}}$. Under the far-field assumption, the direction of departure (DoD) and direction of arrival (DoA) coincide, that is, θ. The corresponding transmit and receive steering vectors are

$$\mathbf{a}^{(p)}_{\mathrm{Tx}}(\theta) = \exp\Big(j\beta\, \mathbf{d}^{(p)}_{\mathrm{Tx}} \sin\theta\Big), \qquad \mathbf{a}^{(p)}_{\mathrm{Rx}}(\theta) = \exp\Big(j\beta\, \mathbf{d}^{(p)}_{\mathrm{Rx}} \sin\theta\Big), \tag{2.12}$$

where the exponential is applied element-wise. The MIMO (virtual) steering vector for aperture p is the Kronecker product.

$$\mathbf{a}^{(p)}(\theta) = \mathbf{a}^{(p)}_{\mathrm{Rx}}(\theta) \otimes \mathbf{a}^{(p)}_{\mathrm{Tx}}(\theta) \in \mathbb{C}^{M_{\mathrm{Tx}} M_{\mathrm{Rx}} \times 1}. \tag{2.13}$$

Equivalently, using the virtual array distribution $\mathbf{d}_v(i,j) = \mathbf{d}^{(p)}_{\mathrm{tx}}(i) + \mathbf{d}^{(p)}_{\mathrm{rx}}(j)$, the $((i,j)-th)$ entry of $\mathbf{a}^{(p)}(\theta)$ can be written as

$$\big[\mathbf{a}^{(p)}(\theta)\big]_{(i,j)} = \exp\Big(j\beta\big(\mathbf{d}^{(p)}_{v}(i,j)\big) \sin\theta\Big). \tag{2.14}$$

Bi-static manifold

For a bi-static aperture p formed by transmitter from sensor a and receiver from sensor b, the DoD φ (in transmitter) and the DoA ψ (at the receiver) generally differ. The transmit and receive steering vectors are

$$\mathbf{a}^{(p)}_{\mathrm{Tx},a}(\varphi) = \exp\Big(j\beta\, \mathbf{d}^{(p)}_{\mathrm{Tx},a} \sin\varphi\Big), \qquad \mathbf{a}^{(p)}_{\mathrm{Rx},b}(\psi) = \exp\Big(j\beta\, \mathbf{d}^{(p)}_{\mathrm{Rx},b} \sin\psi\Big), \tag{2.15}$$

and the bi-static MIMO steering vector is given by the Kronecker product,

$$\mathbf{a}^{(p)}(\varphi,\psi) = \mathbf{a}^{(p)}_{\mathrm{Rx},b}(\psi) \otimes \mathbf{a}^{(p)}_{\mathrm{Tx},a}(\varphi). \tag{2.16}$$

Entry-wise, using per-element abscissae $d^{(p)}_{\mathrm{Tx},a,i}$ and $d^{(p)}_{\mathrm{Rx},b,j}$, we have

$$\big[\mathbf{a}^{(p)}(\varphi,\psi)\big]_{(i,j)} = \exp\Big(j\beta\big(\mathbf{d}^{(p)}_{\mathrm{Tx},a,i} \sin\varphi + \mathbf{d}^{(p)}_{\mathrm{Rx},b,j} \sin\psi\big)\Big). \tag{2.17}$$

When the target is sufficiently far ($R \geq R_{\mathrm{F}}$) and the bi-static angle is small, we recover the mono-static case setting $\varphi \approx \psi \approx \theta$.

Per-aperture measurement model. After range Doppler processing and snapshot extraction in a given bin (r, v), the array observation for aperture p can be compactly written as

$$\mathbf{y}^{(p)} = \mathbf{A}^{(p)}(\theta)\,\mathbf{x} + \mathbf{n}^{(p)}, \tag{2.18}$$

where

- $\mathbf{y}^{(p)} \in \mathbb{C}^{M_{Tx}M_{Rx}\times 1}$ is the measurement snapshot across M_p virtual channels of aperture p,
- $\mathbf{A}^{(p)}(\theta) = [\mathbf{a}^{(p)}(\theta_1)\ \cdots\ \mathbf{a}^{(p)}(\theta_K)]$ is the steering matrix formed by stacking steering vectors for all K candidate angles,
- $\mathbf{x} \in \mathbb{C}^{K\times 1}$ contains the complex reflectivities (sparse with nonzero entries corresponding to actual target angles),
- $\mathbf{n}^{(p)}$ is additive noise.

Multi-aperture stacking

For the four apertures $p \in \{\mathrm{M1}\!\to\!\mathrm{M1}, \mathrm{M2}\!\to\!\mathrm{M2}, \mathrm{M1}\!\to\!\mathrm{M2}, \mathrm{M2}\!\to\!\mathrm{M1}\}$, the per-aperture observations can be stacked into a single linear model:

$$\mathbf{y} = \begin{bmatrix}\mathbf{y}^{(1)}\\ \mathbf{y}^{(2)}\\ \mathbf{y}^{(3)}\\ \mathbf{y}^{(4)}\end{bmatrix} = \begin{bmatrix}\mathbf{A}^{(1)}(\theta)\\ \mathbf{A}^{(2)}(\theta)\\ \mathbf{A}^{(3)}(\theta)\\ \mathbf{A}^{(4)}(\theta)\end{bmatrix}\mathbf{x} + \begin{bmatrix}\mathbf{n}^{(1)}\\ \mathbf{n}^{(2)}\\ \mathbf{n}^{(3)}\\ \mathbf{n}^{(4)}\end{bmatrix} = \mathbf{A}(\theta)\,\mathbf{x} + \mathbf{n}, \tag{2.19}$$

where $\mathbf{y}$ concatenates all aperture snapshots, $\mathbf{A}(\theta)$ is the complete steering matrix, and $\mathbf{n}$ is the stacked noise vector. This unified model is the basis for both noncoherent and coherent multi-aperture DOA estimation, with the difference that the coherent case requires a prior phase alignment across apertures.

Receive signal cube

Before snapshot extraction, the raw data for each aperture are organized as a three-dimensional signal cube with axes.

- **fast-time** (samples within a chirp, used for range FFT),
- **slow-time** (chirp index within CPI, used for Doppler FFT),
- **channel index** (Tx–Rx virtual element, used for spatial processing).

2.3. System assumption for Scope of Thesis

In order to focus on the core problem of direction-of-arrival (DoA) estimation in distributed automotive radar systems, a number of simplifying assumptions are introduced. These assumptions delimit the scope of this thesis and are summarized below:

- **Clock synchronization:** The distributed radar systems are synchronized in time, so that all transmitters start their chirps simultaneously. However, *phase coherence across different radar systems is not assumed*. This distinction allows for both noncoherent and coherent processing frameworks to be investigated.

- **Far-field plane-wave approximation:** The incoming wavefronts are approximated as planar across each array aperture (far-field assumption). However, for coherent fusion, *strict near-field geometric relations* is used when applying phase compensation across different apertures.
- **Target visibility:** Each target is assumed to be detectable by all radar subsystems, ensuring that consistent range–velocity bins are available in all four apertures.
- **Signal separation:** After modulation and demodulation, the received signals corresponding to different transmitters at a given receiver are assumed to be separable. That is, contributions from multiple transmitters can be correctly distinguished in the receiver processing chain.
- **Propagation model:** Multipath effects, clutter, and diffuse scattering are neglected. Only line-of-sight (LoS) propagation between the transmitter, target, and receiver is considered.
- **Angular domain restriction:** DoA estimation is carried out only in the azimuth (horizontal) domain. Estimation of the elevation angle (vertical) is excluded from the scope of this thesis.
- **Noise model (additional assumption):** Receiver noise across different antennas and subsystems is assumed to be independent, spatially white and Gaussian. This is a standard assumption that simplifies the covariance structure in array processing.

2.4. Conclusion

In this chapter, the system and signal models that form the basis for this thesis have been established. First, the radar network configuration was introduced, consisting of two nodes with multiple transmit and receive antennas, leading to both mono-static and bi-static apertures. The geometric setup was formalized using the concept of virtual arrays, providing an extended aperture for improved angular resolution.

Second, the near-field and far-field assumptions were discussed. Although the far-field plane-wave approximation is adopted for direction-of-arrival (DoA) modeling, strict geometric relations are retained for phase compensation in coherent processing to ensure accuracy across distributed apertures.

Third, the mathematical formulation of the transmitted FMCW waveform and the received signal model was derived. This included the multi-target superposition model, array steering vectors for both mono-static and bi-static cases, and the compact per-aperture and multi-aperture measurement equations. These models clarify how the received snapshots are constructed and how the different apertures can be combined coherently or noncoherently. The structure of the three-dimensional receiving signal cube (fast-time, slow-time, and channel) was also described, highlighting the organization of the data for subsequent range-velocity-angle processing.

Finally, a set of system assumptions was introduced to delimit the scope of the thesis. These include synchronization assumptions, propagation conditions, target visibility, separability of signals, and restriction to azimuthal DoA estimation. Together, these assumptions simplify the problem to a tractable yet representative framework.

Overall, this chapter has provided a consistent and unified signal modeling basis that will be used in the following chapters for algorithm development, data association, and fine DoA estimation.

3

Signal Pre-Processing

3.1. Range-Velocity Map

Given the raw received signal model in (3.1)–(3.2), the standard FMCW pre-processing first performs *dechirping* (mixing with conjugated transmit chirp and low-pass filtering) to obtain the beat signal, and then applies 2-D FFT[24] along the fast-time and slow-time dimensions to form the range–velocity (RV) map. Finally, complex peaks are selected to form per-bin snapshots across the channel dimension.

Dechirp (mixing & low-pass filtering). For aperture p and receiving channel q, with the raw signal

$$y_{p,q}(t,m) = \sum_{k=1}^{K} \alpha_{p,q,k}\, s_{\mathrm{tx}}\big(t - \tau_{p,k}(m,q)\big) + w_{p,q}(t,m), \tag{3.1}$$

and

$$s_{\mathrm{tx}}(t) = \exp\left\{ j2\pi \left(f_0 t + \frac{k_s}{2}\, t^2 \right) \right\}, \tag{3.2}$$

we define the (baseband) beat signal after dechirp as

$$b_{p,q}(t,m) \triangleq \mathrm{LPF}\{\, y_{p,q}(t,m)\, s_{\mathrm{tx}}^{*}(t)\,\}\,. \tag{3.3}$$

Substituting (3.1)–(3.2) and expanding $(t-\tau)^2 = t^2 - 2t\tau + \tau^2$ produces the explicit exponential form

$$b_{p,q}(t,m) = \sum_{k=1}^{K} \alpha_{p,q,k}\, \underbrace{\exp\big(-j2\pi k_s\, \tau_{p,k}(m,q)\, t \big)}_{\text{beat term } f_b = k_s \tau_{p,k}}\; \underbrace{\exp\left\{ -j2\pi \left(f_0 \tau_{p,k}(m,q) - \frac{k_s}{2} \tau_{p,k}^{2}(m,q) \right) \right\}}_{\text{constant phase}} + \tilde{w}_{p,q}(t,m), \tag{3.4}$$

where $\tilde{w}_{p,q}(t,m)$ is the post-mixing noise which is assumed to be Guassion white noise[25]. and $\tau_{p,k}(m,q) = R_{p,k}(m,q)/c$ is the two-way delay defined in Chapter 2. The first exponential in (3.4) is the *beat term*: its frequency $f_b = k_s \tau_{p,k}$ encodes the delay (and hence the path length $R_{p,k} = c\,\tau_{p,k}$).

Discretization. Each chirp contains N_r fast-time samples. Let the sampling interval be $\Delta t = T_{\mathrm{chirp}}/N_r$ and $t_n = n\,\Delta t$ with $n = 0, \ldots, N_r - 1$. Using N_c chirps indexed by $m = 0, \ldots, N_c - 1$, we write discrete beat samples as

$$b_{p,q}[n,m] \triangleq b_{p,q}(t_n, m). \tag{3.5}$$

Range FFT (fast-time). For each chirp m, a 1-D DFT along n gives range-domain samples:

$$\tilde{b}_{p,q}[\ell, m] = \sum_{n=0}^{N_r-1} b_{p,q}[n, m] \exp\left(-j \frac{2\pi n\ell}{N_r}\right), \qquad \ell = 0, \dots, N_r - 1. \tag{3.6}$$

Each frequency bin ℓ corresponds to a delay (hence the path length) through the FMCW mapping

$$\tau(\ell) = \frac{\ell}{N_r} \frac{1}{k_s \Delta t}, \qquad R(\ell) = c\,\tau(\ell). \tag{3.7}$$

(Recall R here is the two-way path length defined in Chapter 2; for the mono-static range, one may report $R/2$ if desired.)

Doppler FFT (slow-time). For each range bin ℓ, a DFT along the chirp index m produces the Doppler axis (velocity):

$$B_{p,q}[\ell, d] = \sum_{m=0}^{N_c-1} \tilde{b}_{p,q}[\ell, m] \exp\left(-j \frac{2\pi md}{N_c}\right), \qquad d = 0, \dots, N_c - 1. \tag{3.8}$$

The pair (ℓ, d) indexes a specific range–velocity cell. (An exact velocity mapping $d \rightarrow$ is not required here, since the model already captures the delay variation across m through $\tau_{p,k}(m, q)$.)

In the mathematical formulation above, the FFT lengths were taken equal to the number of available samples, i.e. N_r for the range FFT and N_c for the Doppler FFT. In practice, however, it is common to specify an FFT size `nfft` larger than the data length, corresponding to zero-padding in the time domain. This does not change the fundamental resolution ($c/2B$ in range and $1/(N_c T_{\text{chirp}})$ in Doppler), but provides a finer discretization of the frequency axes and hence a smoother RV map visualization.

Range–Velocity map and snapshot extraction. The RV map at each channel (p, q) is obtained as the squared magnitude of the 2-D FFT output:

$$\mathrm{RV}_{p,q}[\ell, d] = \left|B_{p,q}[\ell, d]\right|^2. \tag{3.9}$$

At detected peaks $(\ell^\star, d^\star)$, we extract the complex *snapshot* across all channels of aperture p as the input to spatial DoA processing:

$$\mathbf{y}^{(p)} \triangleq \left[B_{p,1}[\ell^\star, d^\star],\ B_{p,2}[\ell^\star, d^\star],\ \dots,\ B_{p,M_p}[\ell^\star, d^\star]\right]^\top \in \mathbb{C}^{M_{Tx} M_{Rx} \times 1}. \tag{3.10}$$

These snapshots are precisely the per-aperture observations used in the measurement model $\mathbf{y}^{(p)} = \mathbf{A}^{(p)}(\theta)\mathbf{x} + \mathbf{n}^{(p)}$ (cf. Chapter 2), now indexed by the selected range–velocity bin $(\ell^\star, d^\star)$.

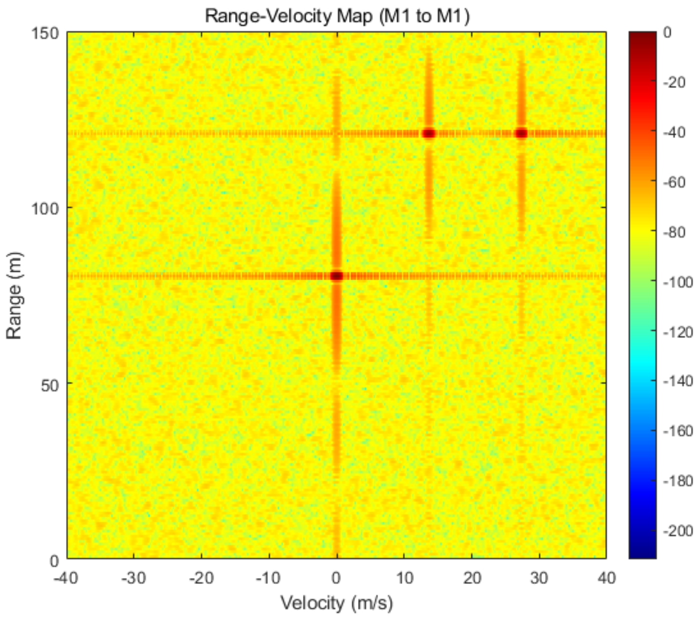

Figure 3.1: Example RV map using targets in Table 3.1 and radar settings in Table 2.1.

Table 3.1: Target parameters used for the RV map example

Target ID	Distance (m)	DOA (°)	v_x (m/s)	v_y (m/s)
1	80	30	0	0
2	80	35	0	0
3	120	60	10	10
4	120	60	20	20

3.2. Coarse DOA Estimation and Localization

3.2.1. Coarse DOA Estimation

In the first stage, a computationally efficient coarse direction-of-arrival (DoA) estimation is performed using conventional Bartlett beamforming. For a given aperture p, recall the snapshot vector $\mathbf{y}^{(p)} \in \mathbb{C}^{M_{Tx}M_{Rx}\times 1}$ defined in Section 3.1. The Bartlett spatial spectrum is given by

$$P^{(p)}_{\text{Bartlett}}(\theta) = \frac{\left|\mathbf{a}^{(p)}(\theta)^H\,\mathbf{y}^{(p)}\right|^2}{\|\mathbf{a}^{(p)}(\theta)\|_2^2}, \qquad \theta \in \Theta_{\text{FOV}}, \tag{3.11}$$

where $\mathbf{a}^{(p)}(\theta)$ denotes the steering vector at angle θ for aperture p, and $\Theta_{\text{FOV}} = [-50°, 50°]$ specifies the field of view under consideration. A uniform angular grid with step size $2°$ is used.

The Bartlett method requires only a sequence of inner products between the steering vector and the snapshot, and thus incurs a very low computational cost. Although its angular resolution is limited, it is well suited for providing a coarse estimate of the target directions. These coarse estimates will then be used to define narrow angular search intervals for the subsequent high-resolution sparse reconstruction stage.

It is important to note that the coarse DoA estimates obtained from different apertures correspond to different angle definitions.

- For *mono-static apertures* (M1→M1 and M2→M2), the estimated angles are directly φ and ψ.
- For *bi-static apertures* (M1→M2 and M2→M1), the manifold is constructed as a Kronecker product of the Tx and Rx steering vectors (see Chapter 2). Under the far-field approximation, φ and ψ are approximately equal ($\varphi \approx \psi \approx \theta$). Hence, for coarse estimation it is sufficient to represent the angle by a single parameter θ. This approximation is reasonable because the coarse Bartlett stage only serves to provide angular cues for association, not precise localization.

In later processing, all estimated angles (whether expressed as φ, ψ, or θ) will be consistently transformed into the global coordinate system, so observations from the four apertures can be fused.

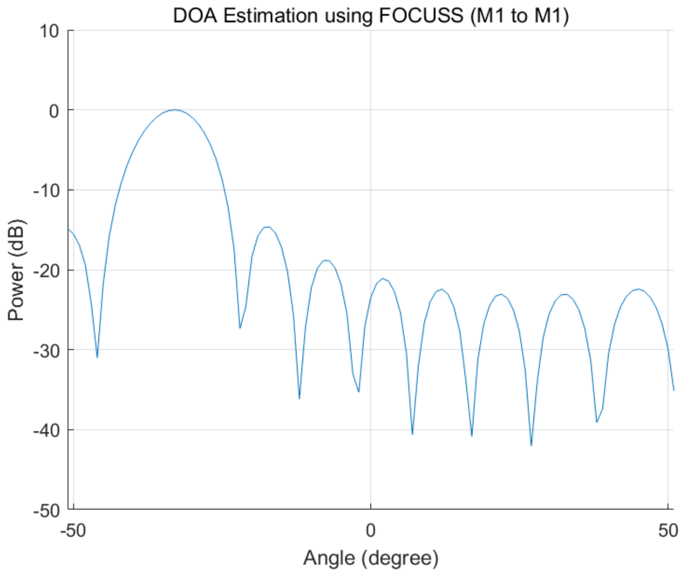

Figure 3.2: Example Bartlett beamforming spectrum (aperture M1 → M1)

3.2.2. Localization in Global Coordinate System

Once coarse DoA estimates are available, the next step is to transform the per-aperture measurements into a common global Cartesian coordinate system. For illustration, consider two mono-static apertures with measured ranges R_1, R_2 and coarse angle estimates $\hat{\varphi}_1, \hat{\psi}_2$, together with baseline offsets L_1, L_2 along the x axis. The corresponding localization coordinates are obtained as

$$\begin{bmatrix} \hat{x}_1 \\ \hat{y}_1 \end{bmatrix} = \begin{bmatrix} R_1 \sin(\hat{\varphi}_1) + L_1 \\ R_1 \cos(\hat{\varphi}_1) \end{bmatrix}, \qquad \begin{bmatrix} \hat{x}_2 \\ \hat{y}_2 \end{bmatrix} = \begin{bmatrix} R_2 \sin(\hat{\psi}_2) - L_2 \\ R_2 \cos(\hat{\psi}_2) \end{bmatrix}. \tag{3.12}$$

For the bi-static apertures (M1→M2 and M2→M1), the available measurements consist of ranges R_3, R_4 and coarse angle estimates $\hat{\theta}_3, \hat{\theta}_4$. Since coarse localization does not require high precision and the far-field approximation holds, the transmit/receive angles are treated as a single effective parameter $\hat{\theta}$. The corresponding estimated global coordinates are expressed as

$$\begin{bmatrix} \hat{x}_3 \\ \hat{y}_3 \end{bmatrix} = \begin{bmatrix} R_3 \sin(\hat{\theta}_3) \\ R_3 \cos(\hat{\theta}_3) \end{bmatrix}, \qquad \begin{bmatrix} \hat{x}_4 \\ \hat{y}_4 \end{bmatrix} = \begin{bmatrix} R_4 \sin(\hat{\theta}_4) \\ R_4 \cos(\hat{\theta}_4) \end{bmatrix}. \tag{3.13}$$

These estimated Cartesian coordinates represent the target positions inferred from each aperture in the global coordinate frame, shown in Fig.3.3. In subsequent processing, they are used as inputs for association across apertures and for refining the localization with fine DoA estimation.

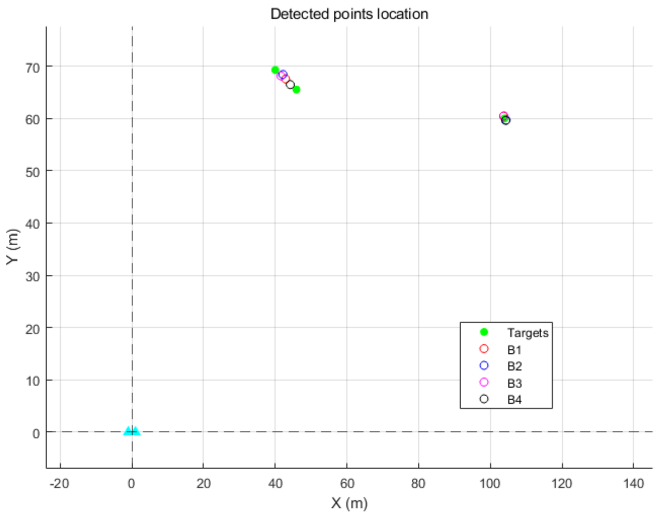

Figure 3.3: Illustration of coarse localization in the global coordinate system using range and coarse DoA estimates from two apertures.

3.3. Multi-Aperture Data Association

The purpose of this stage is to determine which combinations of snapshots from the four apertures correspond to the same potential target state. We define a *target state* t_k as the joint observation of a potential scatterer in global coordinates, characterized by a particular range-angle position and radial velocity. Importantly, we use the term *state* rather than *target* because, under the coarse DoA estimation, multiple closely spaced objects may still be indistinguishable and thus share the same coarse angular estimate. Each target state is represented as a quadruple of snapshots, one from each aperture:

$$t_k = \{b_{1a},\, b_{2b},\, b_{3i},\, b_{4j}\}, \qquad \mathcal{T} = \{t_1, t_2, \ldots, t_K\}, \tag{3.14}$$

where b_{pa} denotes the snapshot extracted from the a-th detected peak in aperture p. The goal of data association is to construct the set $\mathcal{T}$ of all feasible target states.

In the radar tracking literature, there are many methods to address data association, such as particle filters [26] and the Joint Probabilistic Data Association (JPDA) [27], both of which rely on multiple consecutive snapshots within a prediction-update framework. Such methods are well established for multi-snapshot tracking but cannot be directly applied when only a single snapshot is available, a scenario for which data association methods have been scarcely investigated so far. For automotive radar networks, recent work [28] has given the idea of exploring geometry-based consistency checks for association in imaging data; this work inspired our use of geometric relations and velocity information to evaluate association consistency across snapshots.

Association logic. Since only single snapshot data are available, conventional *prediction* + *update* tracking methods cannot be applied. Instead, the association is based on two criteria: *distance matching* and *velocity validation*. The procedure is as follows:

1. Enumerate all possible quadruples $\{b_{1a}, b_{2b}, b_{3i}, b_{4j}\}$.
2. For each quadruple, compute the corresponding estimated global coordinates (cf. Section 3.2.2) and evaluate the consistency of the distance between apertures. Only quadruples with sufficiently small interaperture distance mismatch (below a predefined threshold) are retained.
3. For the surviving candidates, apply velocity validation to discriminate between spatially consistent

but velocity-inconsistent combinations. Specifically, a quadruple is accepted if

$$|\hat{v}_3 - \hat{v}_4| + |(\hat{v}_1 + \hat{v}_2) - \hat{v}_3| + |(\hat{v}_1 + \hat{v}_2) - \hat{v}_4| < \text{threshold}, \tag{3.15}$$

where $\hat{v}_1, \hat{v}_2, \hat{v}_3, \hat{v}_4$ denote the estimated velocities corresponding to the four apertures. Each $\hat{v}_p$ is a measurement of the radial velocity along the line of sight from the target to the respective radar node. For bi-static apertures, $\hat{v}_3$ and $\hat{v}_4$ represent the sum of the target velocity components projected along the transmit and receive directions of the two radar systems.

Association outcome. The associated quadruples resulting show a continuous *progressive phase* across apertures, as illustrated in Fig. 3.4, confirming that the constituent snapshots originate from the same physical scatterer. The main outcomes of the multi-aperture association stage can be summarized as follows:

- It establishes a consistent mapping between observations from different apertures using single snapshot data, enabling coherent or non-coherent fusion in later stages.
- Provides an initial separation of targets, discarding combinations that differ significantly in position or velocity, and thereby ensures a sufficiently sparse scene for the fine DoA estimation.
- For each accepted target state t_k, the corresponding coarse angular estimate defines the angular field-of-view (FOV) constraint for the subsequent high-resolution sparse reconstruction.

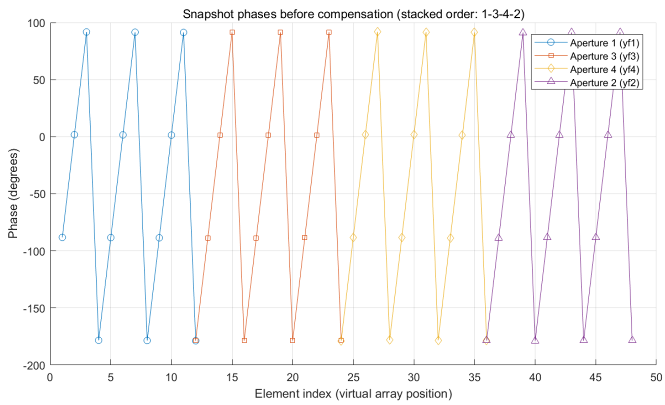

Figure 3.4: Illustration of progressive phase continuity across four apertures for an associated target state.

3.4. Conclusion

In this chapter, the key pre-processing steps that transform the raw FMCW radar measurements into structured observations suitable for target association and subsequent fine DoA estimation were presented. Starting from the dechirped signals, two-dimensional FFT operations were applied in fast and slow time dimensions to form range-velocity maps, from which snapshot vectors were extracted at detected target peaks for each aperture.

A computationally efficient Bartlett beamformer was then employed to obtain coarse DoA estimates over a limited angular field of view. These coarse angular cues, together with range and velocity estimates, were transformed into the global coordinate frame to provide an initial location of candidate targets. The process was extended to both mono-static and bi-static apertures, with appropriate approximations adopted in the latter case to reduce complexity at the coarse stage.

Finally, a multi-aperture data association framework was introduced. By combining distance matching and velocity validation, feasible quadruples of snapshots were identified in the four apertures. The resulting associated sets ensure consistency of observations, separate spatially and kinematically distinct targets, and define narrow angular windows for the fine-sparse reconstruction stage.

Overall, the signal pre-processing chain achieves three objectives: (1) it reduces the raw signal cube into compact per-aperture snapshots; (2) it provides coarse but reliable angular and positional cues in the global coordinate system; and (3) it establishes a consistent set of associated observations across multiple apertures. These results form the essential input for the high-resolution DoA estimation and fusion methods developed in the following chapter.

4

Block FOCUSS Fine Estimation

4.1. Sparse Reconstruction for DOA Estimation

In this stage, sparse reconstruction approaches will be implemented in a fine DOA estimation. For each aperture $p \in \{1, 2, 3, 4\}$, let us define $N_p = M_{Tx} M_{Rx}$ recall the aperture snapshot $\mathbf{y}^{(p)} \in \mathbb{C}^{N_p \times 1}$ obtained from a selected range–velocity bin (cf. Chapter 3). The measurement model is

$$\mathbf{y}^{(p)} = \mathbf{A}^{(p)} \mathbf{x}^{(p)} + \mathbf{n}^{(p)}, \tag{4.1}$$

where $\mathbf{A}^{(p)} \in \mathbb{C}^{N_p \times G}$ is the steering matrix constructed on an angular search grid of size G, $\mathbf{x}^{(p)} \in \mathbb{C}^{G \times 1}$ is the vector of sparse coefficients encoding target powers at the angles of the grid, and $\mathbf{n}^{(p)}$ denotes noise.

Steering matrix construction. The construction of $\mathbf{A}^{(p)}$ depends on whether the aperture is mono-static or bi-static:

- **Mono-static apertures.** For M1→M1, the steering matrix is defined over a grid of departure angles $\{\varphi_g\}_{g=1}^{G}$:

  $$\mathbf{A}^{(1)} = \left[\mathbf{a}^{(1)}(\varphi_1),\, \mathbf{a}^{(1)}(\varphi_2),\, \ldots,\, \mathbf{a}^{(1)}(\varphi_G)\right], \qquad \mathbf{A}^{(1)} \in \mathbb{C}^{N_p \times G}. \tag{4.2}$$

  Similarly, for M2→M2, defined over arrival angles $\{\psi_g\}_{g=1}^{G}$:

  $$\mathbf{A}^{(2)} = \left[\mathbf{a}^{(2)}(\psi_1),\, \mathbf{a}^{(2)}(\psi_2),\, \ldots,\, \mathbf{a}^{(2)}(\psi_G)\right], \qquad \mathbf{A}^{(2)} \in \mathbb{C}^{N_p \times G}. \tag{4.3}$$

- **Bi-static apertures.** The manifold is defined as a Kronecker product of transmit and receive steering vectors. For example, for aperture M1→M2:

  $$\mathbf{a}_{\mathrm{M1M2}}(\varphi, \psi) = \mathbf{a}_{\mathrm{Tx1}}(\varphi) \otimes \mathbf{a}_{\mathrm{Rx2}}(\psi). \tag{4.4}$$

  The corresponding steering matrix is constructed over all (φ_g, ψ_g) grid pairs as

  $$\mathbf{A}^{(3)} = \left[\mathbf{a}_{\mathrm{M1M2}}(\varphi_1, \psi_1),\, \mathbf{a}_{\mathrm{M1M2}}(\varphi_2, \psi_2),\, \ldots,\, \mathbf{a}_{\mathrm{M1M2}}(\varphi_G, \psi_G)\right], \qquad \mathbf{A}^{(3)} \in \mathbb{C}^{N_p \times G}. \tag{4.5}$$

Similarly, for aperture M2→M1:

$$\mathbf{A}^{(4)} = \big[\mathbf{a}_{\mathrm{M2M1}}(\psi_1, \varphi_1),\ \mathbf{a}_{\mathrm{M2M1}}(\psi_2, \varphi_2),\ \ldots,\ \mathbf{a}_{\mathrm{M2M1}}(\psi_G, \varphi_G)\big], \qquad \mathbf{A}^{(4)} \in \mathbb{C}^{N_p \times G}. \tag{4.6}$$

Sparse reconstruction problem. Given $\mathbf{y}^{(p)}$ and $\mathbf{A}_{(p)}$, the sparse coefficient vector $\mathbf{x}^{(p)}$ can be recovered by solving a regular optimization ℓ_1:

$$\hat{\mathbf{x}}^{(p)} = \arg\min_{\mathbf{x}}\ \|\mathbf{y}^{(p)} - \mathbf{A}^{(p)}\mathbf{x}\|_2^2 + \epsilon\|\mathbf{x}\|_1, \tag{4.7}$$

where $\epsilon > 0$ is a regularization parameter. The nonzero entries of $\hat{\mathbf{x}}^{(p)}$ indicate the estimated DoA grid points for aperture p.

In the following sections, we extend this formulation to a block-sparse model across multiple apertures, enabling non-coherent and coherent fusion via the block FOCUSS algorithm.

4.2. Coordinate System Transform

In order to perform fine DoA estimation jointly across all apertures, it is necessary to establish a common global angular support. This section describes how the refined global angle grid $\boldsymbol{\theta}$ is defined and how it is converted to the local angle coordinates of each aperture.

Unified target range estimate. From the range–velocity maps of the two mono-static apertures, the range measurements R_1 and R_2 are obtained. Together with the baseline offsets L_1 and L_2 of the two radar systems relative to the global origin, these quantities form a triangle geometry that allows us to derive a unified effective range estimate $\hat{R}$ for the potential target, expressed as

$$\hat{R} = \sqrt{\frac{L_2 R_1^2 + L_1 R_2^2}{L_1 + L_2} - L_1 L_2}. \tag{4.8}$$

Global angle axis. For each associated target state (cf. Section 3.3), the center angle θ in the global coordinate system is first determined. Around this coarse direction, a refined angular grid is defined as

$$\boldsymbol{\theta} = \{\theta_1, \theta_2, \ldots, \theta_G\}, \tag{4.9}$$

where the grid covers a $30°$ field of view centered at θ, sampled with $0.1°$ resolution.

Transformation to local apertures. To ensure consistent global support, the effective range $\hat{R}$ is kept fixed. For each angle $\theta \in \boldsymbol{\theta}$, the corresponding local ranges to the mono-static apertures are computed as

$$R_1(\theta) = \sqrt{\hat{R}^2 + L_1^2 + 2\hat{R}L_1\sin(\theta)}, \qquad R_2(\theta) = \sqrt{\hat{R}^2 + L_2^2 - 2\hat{R}L_2\sin(\theta)}. \tag{4.10}$$

From these ranges, the local DoA coordinates for each aperture are as follows:

$$\varphi(\theta) = \arcsin\left(\frac{\hat{R}\sin(\theta) + L_1}{R_1(\theta)}\right), \qquad \psi(\theta) = \arcsin\left(\frac{\hat{R}\sin(\theta) - L_2}{R_2(\theta)}\right). \tag{4.11}$$

Summary. Thus, each point in the global grid $\theta \in \boldsymbol{\theta}$ can be consistently mapped to local angular coordinates $\varphi(\theta)$ and $\psi(\theta)$, which are then used to construct the steering vectors $\mathbf{a}^{(1)}(\varphi)$, $\mathbf{a}^{(2)}(\psi)$, and the corresponding Kronecker product manifolds for the bi-static apertures. This unified coordinate system ensures that all apertures are aligned on the same global angular support before sparse reconstruction.

4.3. FOCUSS Algorithm

4.3.1. FOCUSS

The Focal Underdetermined System Solver (FOCUSS) [29, 30] is an iterative reweighted minimum norm algorithm for the reconstruction of sparse signals from limited observations. Within the linear model introduced earlier, the sparse reconstruction problem can be formulated as a regularized non-convex optimization:

$$J(x) = \|y - Ax\|_2^2 + \epsilon \|x\|_{p_f} \tag{4.12}$$

where $\epsilon > 0$ is a regularization parameter that balances the fidelity term of the data and the sparsity prior. A larger ϵ enforces stronger data consistency, while a smaller ϵ emphasizes sparsity and improves noise resistance. FOCUSS approximates (4.12) through a sequence of weighted least-squares problems, solved iteratively.

Core iteration (pseudo-inverse form). Starting from an initial estimate $\mathbf{x}^{(0)}$, the k-th iteration proceeds in three main steps:

$$\text{Step 1:} \qquad \mathbf{W}^{(k)} = \operatorname{diag}(|x_1^{(k-1)}|^{1-\frac{p_f}{2}}, \dots, |x_G^{(k-1)}|^{1-\frac{p_f}{2}}), \quad 0 < p_f < 1, \tag{4.13}$$

$$\text{Step 2:} \qquad \mathbf{q}^{(k)} = \left(\mathbf{A}\mathbf{W}^{(k)}\right)^{\dagger} \mathbf{y}, \tag{4.14}$$

$$\text{Step 3:} \qquad \mathbf{x}^{(k)} = \mathbf{W}^{(k)}\, \mathbf{q}^{(k)}, \tag{4.15}$$

where $(\cdot)^{\dagger}$ denotes pseudo-inverse:

$$\left(\mathbf{A}\mathbf{W}^{(k)}\right)_{\epsilon}^{\dagger} \triangleq \left(\left(\mathbf{A}\mathbf{W}^{(k)}\right)^{H}\left(\mathbf{A}\mathbf{W}^{(k)}\right) + \epsilon\,\mathbf{I}\right)^{-1}\left(\mathbf{A}\mathbf{W}^{(k)}\right)^{H}, \quad \epsilon > 0, \tag{4.16}$$

where ϵ serves as a Tikhonov regularization constant that mitigates noise amplification and poor matrix conditioning.

Convergence and remarks. The iteration ends when the relative change between consecutive estimates satisfies $\|\mathbf{x}^{(k)} - \mathbf{x}^{(k-1)}\|_2 / \|\mathbf{x}^{(k-1)}\|_2 < \tau$, or when a predefined maximum iteration count is reached. Equations (4.13)–(4.15) summarize the standard FOCUSS implementation, corresponding to a reweighted minimum norm solution for the problem ℓ_{p_f} regularized. More general p_f norm extensions and convergence analyzes can be found in [29, 30].

4.3.2. Block FOCUSS (non-coherent fusion)

Principle. Recall that in Sect. 4.2 a common global grid $\boldsymbol{\theta} = \{\theta_g\}_{g=1}^{G}$ is constructed and each aperture $p \in \{1, 2, 3, 4\}$ builds its local dictionary $A^{(p)} = [a^{(p)}(\theta_1), \dots, a^{(p)}(\theta_G)]$ from the mapped angles. For the snapshot extracted in a given (R, V) bin, we have the per-aperture linear models

$$y^{(p)} \;=\; A^{(p)} x^{(p)} + n^{(p)}, \qquad p = 1, 2, 3, 4 \tag{4.17}$$

where $x^{(p)} \in \mathbb{C}^G$ is sparse in the set of indexes *same* (the same angles), while its complex amplitudes can be different between apertures due to anisotropic RCS or view-dependent propagation. Stacking the unknowns column-wise yields the coefficient matrix $X = \left[x^{(1)}, \dots, x^{(4)}\right] \in \mathbb{C}^{G \times 4}$, whose *rows* correspond to angles θ_g and whose non-zero rows form the common support. Figure 4.1 illustrates this “row-sparse” (block-sparse) structure: nonzero rows (gray blocks) are shared by all apertures, although their per-aperture amplitudes differ. This principle follows the idea of block-sparse reconstruction in distributed non-coherent multi-static radar systems as introduced in [31].

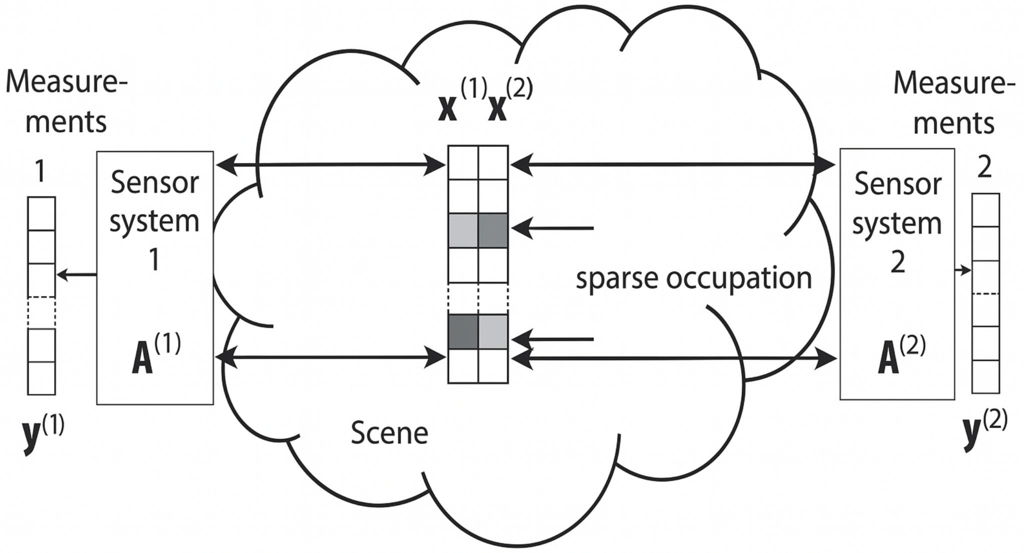

Figure 4.1: Illustration of block (row) sparsity across apertures.[14]

From FOCUSS to Block FOCUSS. Standard FOCUSS recovers a single sparse vector x by iteratively solving a weighted minimum norm problem with a diagonal weight W_k updated from element-wise magnitudes of x_k. *Block FOCUSS* extends this idea to the MMV/row-sparse case by: (i) keeping the per-aperture forward models (4.17) independent (no phase tying across apertures, i.e., non-coherent fusion), (ii) using a **single** diagonal weight $W_k \in \mathbb{C}^{G\times G}$ shared by all apertures, whose entries are updated from the *row* ℓ_{p_f}-norms of X_k, and (iii) updating $x^{(p)}$ for each aperture through the same W_k. Consequently, angles that are strong in apertures *all* are jointly reinforced, which leads to accurate recovery of the **common support** (angles where every aperture exhibits high-magnitude coefficients), while allowing the amplitudes per aperture to differ.

Block FOCUSS objective. With the above notation, the block-sparse recovery is posed as

$$\min_{X\in\mathbb{C}^{G\times L}} \sum_{p=1}^{4} \big\|y^{(p)} - A^{(p)}x^{(p)}\big\|_2^2 \;+\; \epsilon \sum_{g=1}^{G} \|X_{g,:}\|_{p_f}, \quad 0 < p_f \leq 1,\ \epsilon \geq 0, \tag{4.18}$$

where $X_{g,:}$ denotes the g-th row of X, p_f is the FOCUSS exponent, and $\varepsilon > 0$ avoids singular weights. Compared with the single-vector FOCUSS, the penalty in (4.18) promotes *row*-sparsity through the mixed ℓ_{2,p_f} quasinorm, thus enforcing a common set of active angles across apertures.

Iterative solver (Block FOCUSS). Following the same majorization–minimization strategy as FOCUSS, define the diagonal weight at iteration k from the row norms of X_k:

$$W_k \;=\; \mathrm{diag}(w_{k,1},\ldots,w_{k,G}), \qquad w_{k,g} \;=\; \big(\|X_{k,g,:}\|_2 + \varepsilon\big)^{1-\frac{p_\mathrm{f}}{2}}. \tag{4.19}$$

Given W_k, each aperture is updated independently by a weighted minimum norm step (the same weight for all p):

$$x_{k+1}^{(p)} = W_k^2 A^{(p)H} \left(A^{(p)} W_k^2 A^{(p)H} + \epsilon I \right)^{-1} y^{(p)}, \qquad p = 1, 2, 3, 4 \tag{4.20}$$

which reduces to the damped pseudo-inverse form $x_{k+1}^{(p)} = W_k \, (A^{(p)} W_k)^{\dagger} y^{(p)}$ when $\epsilon = 0$. Then form $X_{k+1} = [x_{k+1}^{(1)}, \ldots, x_{k+1}^{(4)}]$, recompute W_{k+1} via (4.19), and iterate until

$$\delta_k = \frac{\|X_{k+1} - X_k\|_F}{\|X_k\|_F} < \tau, \tag{4.21}$$

with a small tolerance τ. A practical choice for ϵ is the minimum of the noise variances estimated from the 4 apertures, which preserves the sensitivity of the strongest channel while regularizing the inverses in (4.20).

Remarks. (1) When $p_{\mathrm{f}} = 1$, Block-FOCUSS becomes a group-Lasso-like reweighted least-squares; choosing $p_f < 1$ yields a stronger sparsity. $p_f = 0.8$ is usually chosen, which can give a moderate balance between resolution and robustness. (2) Unlike the coherent stacking model, Block FOCUSS does *not* require inter-aperture phase alignment; its goal is to *detect and enhance* angles where all apertures carry significant energy, thereby stabilizing support recovery under anisotropic RCS and SNR imbalance. (3) After convergence, the DOA support $\widehat{\mathcal{S}} = \{g : \|X_{g,:}\|_2$ is large$\}$ is taken as a common set of target angles, and the per-aperture amplitudes $\{x_{\widehat{\mathcal{S}}}^{(p)}\}$ are available for further processing.

4.4. Solutions for Numerical Problem

In this section, we will discuss the numerical problems in the fine DOA estimation procedure: what is the problem, what is the reason, and how we will solve it.

4.4.1. Problem Statement

Figure 4.2 shows the result obtained from the Block FOCUSS algorithm previously implemented using the fine-stage angle grid in our model. It can be observed that the estimation suffers from numerous false peaks and that the correct DOA positions cannot be clearly distinguished. This indicates that the current formulation of the Block FOCUSS algorithm does not produce a reliable reconstruction under the given grid setting.

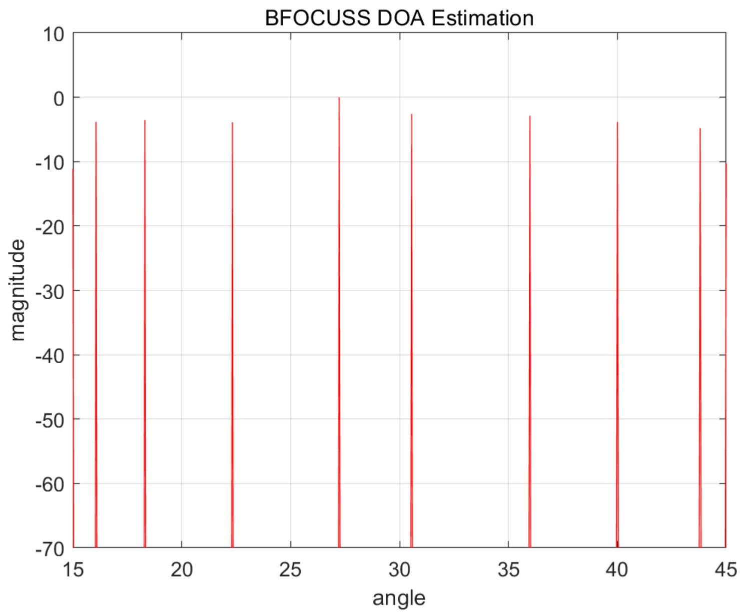

Figure 4.2: Block FOCUSS estimation result($\theta_1 = 29°, \theta_2 = 31°$).

The root cause of this problem lies in the numerical instability of the matrix inversion involved in each FOCUSS iteration. In our fine-stage reconstruction, the field-of-view (FOV) for angle search is deliberately small (about $\pm 15°$) with a dense grid (e.g., $0.1°$ spacing). This leads to a steering matrix $A^{(p)}$ whose adjacent columns become highly correlated. As a result, the Gram matrix $A^{(p)} W_k^2 A^{(p)H}$ in the FOCUSS update step,

$$x_{k+1}^{(p)} = W_k A^{(p)H} (A^{(p)} W_k^2 A^{(p)H} + \epsilon I)^{-1} y^{(p)},$$

can become nearly singular, amplifying numerical errors during inversion. Such an ill-conditioning significantly deteriorates the estimation performance, producing unstable or spurious peaks in the recovered spectrum.

To quantify this effect, we examine the *condition number* of the steering matrix, defined as

$$\kappa(A^{(p)}) = \frac{\sigma_{\max}(A^{(p)})}{\sigma_{\min}(A^{(p)})},$$

where $\sigma_{\max}$ and $\sigma_{\min}$ denote the largest and smallest singular values, respectively. A large condition number implies that small perturbations or numerical noise in the data can cause large deviations in the inversion result. Therefore, the condition number serves as a direct indicator of how susceptible a matrix is to ill-conditioning. Figure 4.3 illustrates that as the FOV range narrows, $\kappa(A^{(p)})$ rapidly increases, which means that the steering matrix becomes more ill-conditioned and the inversion less stable.

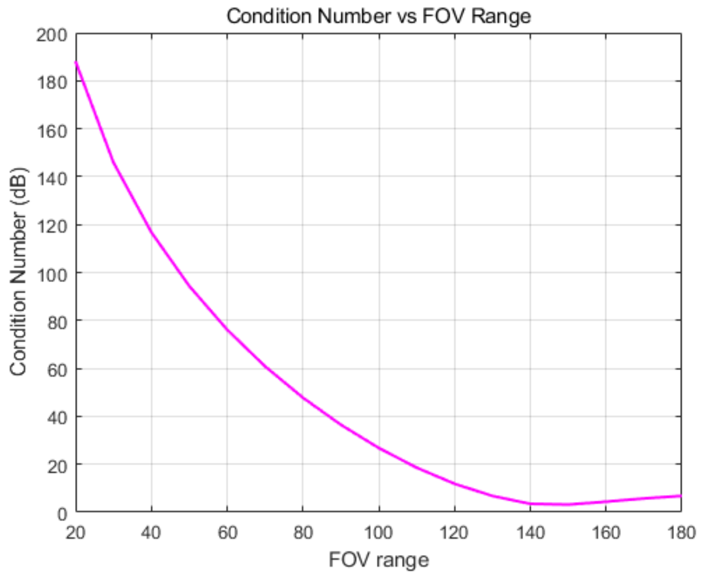

Figure 4.3: condition number of steering matrix versus angle range

Several studies have attempted to mitigate such numerical problems in sparse reconstruction algorithms. An approach is to replace the pseudo-inverse in the FOCUSS update with a **truncated singular value decomposition (TSVD)** [32]. Let the singular value decomposition of the weighted sensing matrix be $A^{(p)}W_k = U\Sigma V^H$, where $\Sigma = \mathrm{diag}(\sigma_1, \sigma_2, \ldots, \sigma_M)$ and $\sigma_1 \geq \sigma_2 \geq \cdots \geq \sigma_M$. The TSVD-based inversion is defined as

$$(A^{(p)}W_k)_r^{\dagger} = V_r \Sigma_r^{-1} U_r^H, \tag{4.22}$$

where only the r largest singular values are retained in Σ_r, while the smaller values (responsible for numerical noise amplification) are discarded. Accordingly, the FOCUSS update becomes

$$x_{k+1}^{(p)} = W_k (A^{(p)}W_k)_r^{\dagger} y^{(p)}. \tag{4.23}$$

Although this method improves numerical stability, it sacrifices useful signal subspace components when the singular value spectrum gradually decays. Thus, the TSVD only mitigates numerical sensitivity but does not fundamentally resolve the ill-conditioning inherent in densely sampled fine grids.

Another line of research offers an insightful idea through *adaptive regularization*. Xia *et al.* proposed the **Adaptive Regularized FOCUSS (AR-FOCUSS)** algorithm [33], which dynamically adjusts the regularization weight ϵ_k at each iteration according to the relative amplitude of the estimated coefficients. Larger regularization is applied to weaker components to enhance stability, while stronger ones are less penalized. This approach effectively balances sparsity and robustness without requiring a fixed regularization parameter.

In summary, the false peaks observed in Figure 4.2 are mainly caused by severe ill-conditioning in the steering matrix when using dense fine grids. Existing remedies such as TSVD improve the numerical robustness, but cannot completely eliminate the problem. In the following sections, we will develop 3 different ways to address numerical problems: adaptive regularization, sparse array configuration, and non-uniform angle axis.

4.4.2. Adaptive Regularization

To further mitigate the numerical instability discussed in the previous section, we introduce an **adaptive regularization** scheme into the FOCUSS framework. The modified cost function is defined as

$$\min_x J(x) = \|y - Ax\|_2^2 + (\epsilon + \gamma)\|x\|_{p_f}, \qquad 0 < p_f \leq 1, \tag{4.24}$$

where ϵ is the nominal regularization parameter and γ is an adaptive term that depends on the numerical conditioning of the sensing matrix. Specifically, γ is defined as

$$\gamma = \eta \log\left(1 + \frac{\kappa(AW_k)}{\kappa_0}\right), \tag{4.25}$$

where $\kappa(AW_k)$ denotes the condition number of the weighted sensing matrix in the k-th iteration, κ_0 is a condition number threshold that determines the point where additional regularization begins to take effect, and η is a positive scaling factor controlling the overall strength of the adaptive term.

This formulation provides a smooth, data-dependent adjustment of the regularization intensity. When the system matrix is well-conditioned ($\kappa(AW_k) \approx \kappa_0$), the adaptive term γ remains close to zero, thus preserving the performance of the original FOCUSS update without introducing unnecessary bias. As $\kappa(AW_k)$ increases—indicating stronger correlation between steering vectors and possible numerical instability— the logarithmic function in (4.25) ensures that γ grows gradually rather than explosively, preventing excessive regularization that could otherwise suppress the true signal components.

The inclusion of κ_0 in the denominator serves to normalize the growth of the condition number, ensuring that the adaptive term is activated only when the matrix begins to exhibit ill-conditioning. Meanwhile, the logarithmic dependence guaranties smooth and bounded growth even for extremely large $\kappa(AW_k)$ values, avoiding over-regularization that would otherwise degrade angular resolution or distort amplitude estimation.

In practice, empirical results show that the setting $\eta = 10^2$ yields a good balance between numerical robustness and reconstruction accuracy. This adaptive regularization effectively stabilizes the inversion process within each FOCUSS iteration, thereby improving convergence and suppressing false peaks caused by near-singular steering matrices.

Figure 4.4 shows the DOA estimation result after applying the proposed adaptive regularization. Compared with the previous ill-conditioned case (Figure 4.2), the false peaks are effectively removed and the true target angles are clearly resolved. This shows that condition-number-based adaptive regularization stabilizes reconstruction and improves the reliability of the estimation.

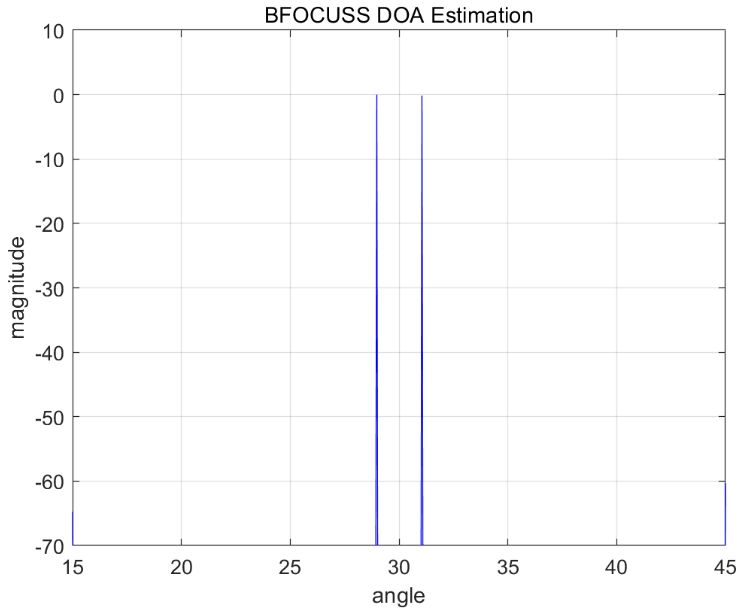

Figure 4.4: Block-FOCUSS DOA estimation after adaptive regularization($\theta_1 = 29°, \theta_2 = 31°$)

4.4.3. Sparse Array Configuration

To further improve numerical stability without relying on additional regularization, we propose a **sparse array configuration** strategy. The key idea is to increase the element spacing of the virtual array from the conventional half-wavelength ($d = 0.5\lambda$) to one wavelength ($d = \lambda$), as illustrated in Figure 4.5. By enlarging the inter-element distance, the correlation between adjacent steering vectors is reduced, thereby improving the conditioning of the steering matrix.

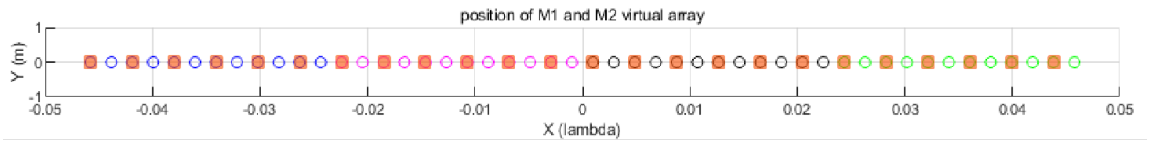

Figure 4.5: Configuration of the sparse virtual array with element spacing increased from 0.5λ to λ.

Effect on matrix conditioning. Let the steering vector of a uniform linear array of M-elements be defined as

$$a(\theta) = \left[1, e^{j2\pi\frac{d}{\lambda}\sin\theta}, \ldots, e^{j2\pi(M-1)\frac{d}{\lambda}\sin\theta}\right]^T. \tag{4.26}$$

When d increases, the phase increase between adjacent sensors increases, lowering the mutual coherence between the steering vectors at nearby angles. This directly improves the condition number of the steering matrix $A = [a(\theta_1), \ldots, a(\theta_G)]$, which can be quantified as

$$\kappa(A) = \frac{\sigma_{\max}(A)}{\sigma_{\min}(A)}.$$

Table 4.1 summarizes the comparison of the condition number for $M = 24$ sensors, FOV $[-45°, 45°]$, and angle step $0.5°$. It is evident that increasing the spacing between 0.5λ and λ dramatically improves the numerical conditioning of A.

Table 4.1: Comparison of steering matrix condition numbers for different spacings ($M = 24$, FOV $[-45°, 45°]$, step $0.5°$).

Element spacing (d)	Condition number $\kappa(A)$
0.5λ	1.751×10^4
λ	1.548

Grating lobe analysis. A well-known drawback of using large element spacing ($d > \lambda/2$) is the appearance of *grating lobes*. For a ULA, the beam pattern for a single source in direction θ_0 is

$$B(\theta) = \frac{1}{M} \frac{\sin\left(M\pi \frac{d}{\lambda}(\sin\theta - \sin\theta_0)\right)}{\sin\left(\pi \frac{d}{\lambda}(\sin\theta - \sin\theta_0)\right)}. \tag{4.27}$$

The mainlobe occurs at $\theta = \theta_0$, while additional maxima (grating lobes) appear when

$$\pi \tfrac{d}{\lambda}(\sin\theta - \sin\theta_0) = m\pi, \quad m \in \mathbb{Z} \setminus \{0\}, \tag{4.28}$$

which yields

$$\sin\theta_g = \sin\theta_0 + m\tfrac{\lambda}{d}. \tag{4.29}$$

When $d = \lambda$, the first grating lobe ($m = \pm 1$) appears at

$$\sin\theta_g = \sin\theta_0 \pm 1.$$

For a target at $\theta_0 = 30°$, this gives $\theta_g \approx 30°$, which means that the closest grating lobe is about $60°$ away from the main lobe—well outside of our fine-stage FOV of $[-45°, 45°]$. Hence, in our fine DOA estimation, grating lobes do not appear within the processing range and do not affect the reconstruction accuracy.

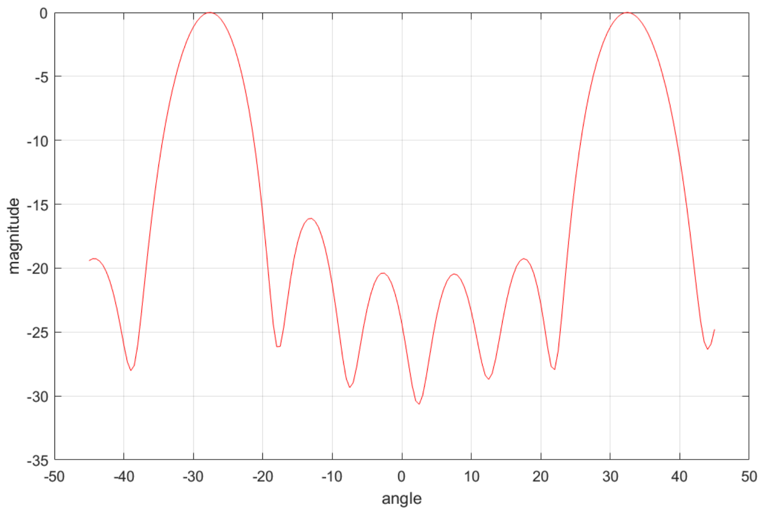

Figure 4.6: Example beam pattern for $d = \lambda$ showing grating lobes outside the $[-45°, 45°]$ FOV. True target angle: $30°$.

Result. After applying the sparse array configuration, the FOCUSS reconstruction achieves a stable and accurate DOA estimation without the need for additional regularization. As shown in Figure 4.7, false peaks are eliminated and true angles are clearly identified, confirming the effectiveness of the proposed sparse array configuration.

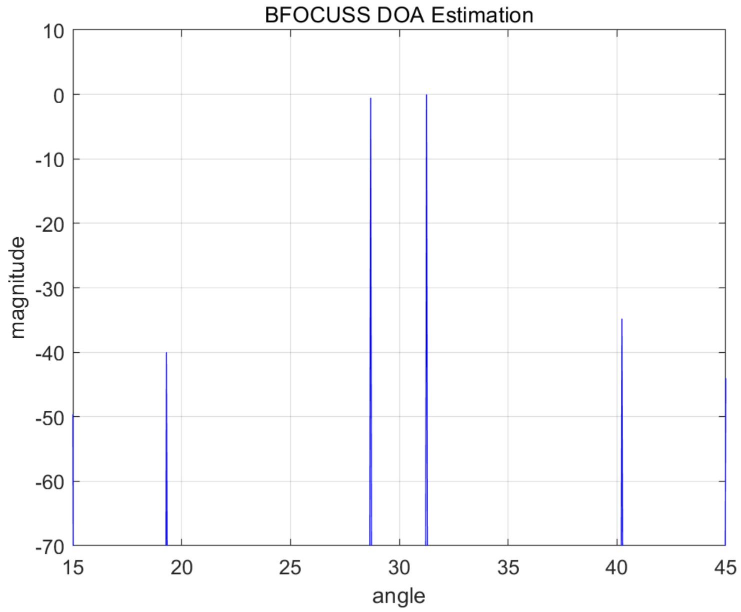

Figure 4.7: BFocuss DOA estimation result with sparse array configuration ($d = \lambda$)

4.4.4. Non-Uniform Angle Axis

Another strategy to alleviate numerical instability without relying on additional regularization is to redesign the angle sampling grid. When the field of view (FOV) covers only a narrow region within $(-90°, 90°)$, the columns of the steering matrix A become highly correlated, causing the number of conditions to increase dramatically. To address this, we employ a **non-uniform angle axis** that spans the entire $(-90°, 90°)$ range, while allocating finer angular resolution only around the region of interest (ROI). In this work, we define the ROI as $\theta \in [-15°, 15°]$, corresponding to the *FOV of interest*, where the grid step is set to $0.1°$. Outside of this range, a coarser grid with step size $2°$ is used to reduce computational complexity.

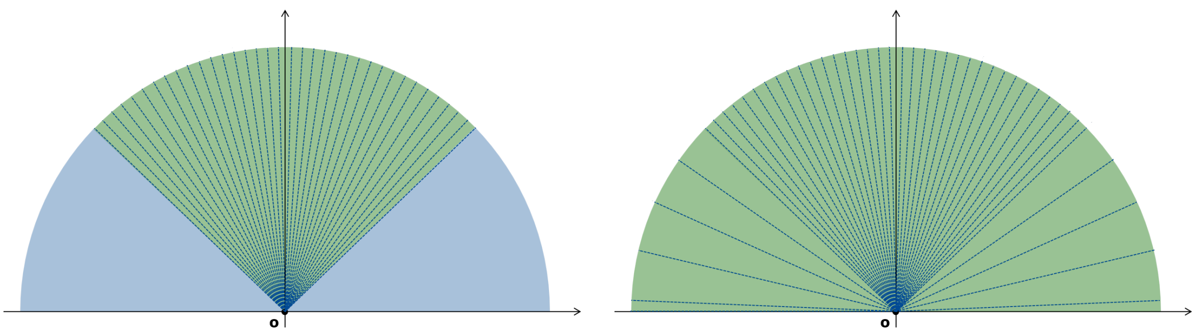

(a) Uniform fine grid within limited FOV of interest

(b) Proposed non-uniform grid covering entire $(-90°, 90°)$ range

Figure 4.8: Comparison between uniform and non-uniform angle sampling strategies.

Conditioning improvement. To quantitatively evaluate the effect of this design, we compute the condition number of the steering matrix A for both configurations using $M = 24$ elements with half-wavelength spacing ($d = 0.5\lambda$). The results are summarized in Table 4.2. It is evident that the non-uniform grid substantially improves the conditioning, reducing the condition number from 1.751×10^4 to 5.038.

Table 4.2: Condition number comparison for uniform and non-uniform angle grids ($M = 24$, $d = 0.5\lambda$).

Angle grid configuration	FOV coverage	Condition number $\kappa(A)$
Uniform fine grid (0.1° step)	$[-15^\circ, 15^\circ]$	1.751×10^4
Non-uniform grid (fine in ROI, coarse outside)	$[-90^\circ, 90^\circ]$	5.038

The improvement arises because expanding the FOV introduces steering vectors with larger phase diversity, reducing inter-column correlation, and stabilizing the matrix inversion in the FOCUSS iterations. At the same time, coarser sampling outside the ROI maintains computational efficiency without compromising estimation accuracy near the expected target region.

Result. Applying the proposed non-uniform angle axis yields stable reconstruction results without any additional regularization. As shown in Figure 4.9, the false peaks observed in the uniform-grid case are completely suppressed, and the target directions are accurately resolved within the fine angular region of interest.

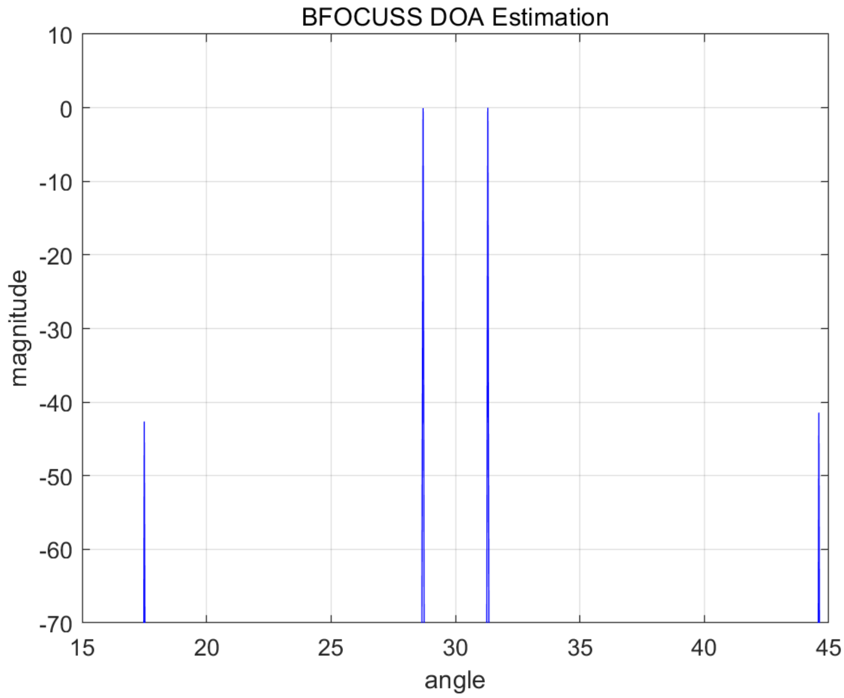

Figure 4.9: BFocuss DOA estimation result using the non-uniform angle axis

4.5. Performance and Results Comparison

4.5.1. Monte-Carlo Simulation Setup

The Monte-Carlo evaluation in this chapter follows the system assumptions summarized in Section 2.3, including far-field plane-wave approximation, line-of-sight propagation, separable multi-transmitter signals, azimuth-only DOA estimation, and independent spatially white receiver noise. This subsection describes in full detail how the simulation results are generated and the additional assumptions specific to the non-coherent reconstruction experiments.

Scene and signal model. Two point targets are located at the same range but with different directions-of-arrival (DOAs). Their positions, velocities, and complex reflection coefficients follow the physical bi-static MIMO radar model established in Chapter 2. The baseband snapshots used for DOA estimation are extracted after dechirping, range FFT, Doppler FFT, and snapshot selection, consistent with the assumptions in Section 2.3. Receiver noise is modeled as circular complex AWGN at a specified SNR, and no phase synchronization is assumed between the two radar systems.

Angular grid and sweep. The angular separation $\Delta\theta$ varies from $0.25°$ to $5°$ in steps of $0.25°$. For each separation, the center angle θ_c is swept from $-45°$ to $45°$ in steps of $1°$, resulting in a two-dimensional simulation loop over $(\Delta\theta, \theta_c)$.

Randomization across trials. For each $(\Delta\theta, \theta_c)$ configuration,

$$N_{\text{trial}} = 5$$

independent Monte-Carlo realizations are performed. In each trial:

- the two targets are assigned independent random reflection phases,
- independent AWGN is generated for each receive channel and each aperture.

Because Block FOCUSS performs non-coherent fusion, no inter-radar phase constraint is imposed in this chapter.

Performance metrics. For each angular separation, the following metrics are computed:

- **Mean MSE**:
$$\text{MSE}(\Delta\theta) = \frac{1}{2N_{\text{trial}}} \sum_{t=1}^{N_{\text{trial}}} \sum_{k=1}^{2} \left(\widehat{\theta}_k^{(t)} - \theta_k^{(t)} \right)^2.$$
- **Successful resolution probability** P_{res}: both targets are detected and matched to the ground truth within a tolerance window.
- **Probability of no false peak** P_{nofalse}: no additional peak appears inside the fine-estimation field of view.
- **Association success probability** P_{assoc}: snapshots from all four apertures are associated to the correct targets.

All results are averaged over the full Monte-Carlo grid $\{(\Delta\theta, \theta_c)\}$.

4.5.2. Comparison I: Different Target Ranges

Figure 4.10a shows the mean separation of MSE versus DOA for three different target ranges, and Fig. 4.10b presents the corresponding probabilities P_{res}, P_{nofalse} and P_{assoc}.

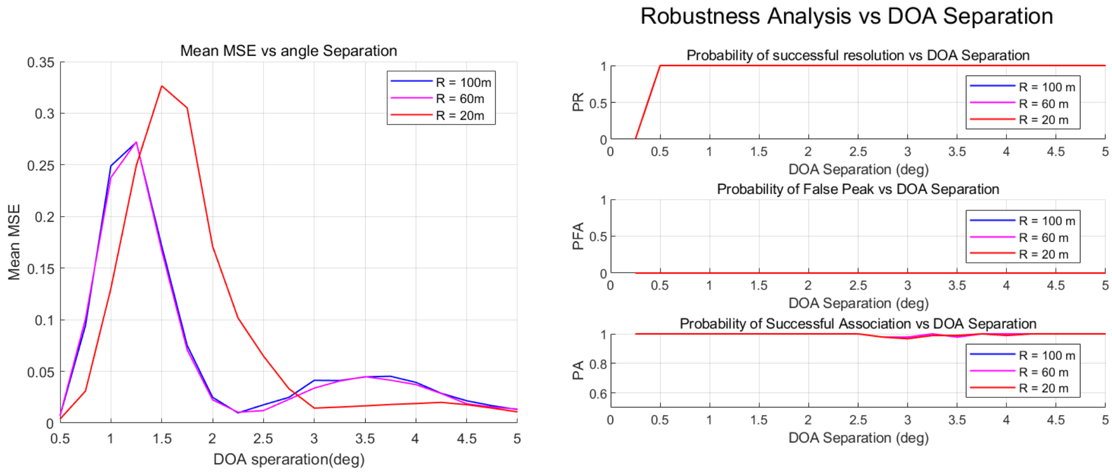

(a) Mean MSE versus DOA separation

(b) Robustness analysis versus DOA separation.

Figure 4.10: Performance comparison at different target ranges.

Discussion:

In general, the proposed system demonstrates robust performance in all tested ranges. The data association success rate remains consistently high and the occurrence of false peaks is very limited. The system can reliably resolve targets with an angular separation greater than approximately $0.5°$, and the obtained estimation errors remain within a small margin, indicating stable reconstruction accuracy.

When the targets are closer (e.g., 20 m), the system is still able to maintain robust performance, while the MSE increases slightly. This degradation is mainly due to the **far-field assumption** in the signal model: at shorter ranges, the curvature of the spherical wavefront becomes non-negligible, resulting in phase mismatch across the array and reduced estimation accuracy.

4.5.3. Comparison II: Different SNR Levels

Figures 4.11a and 4.11b show the results under three SNR conditions.

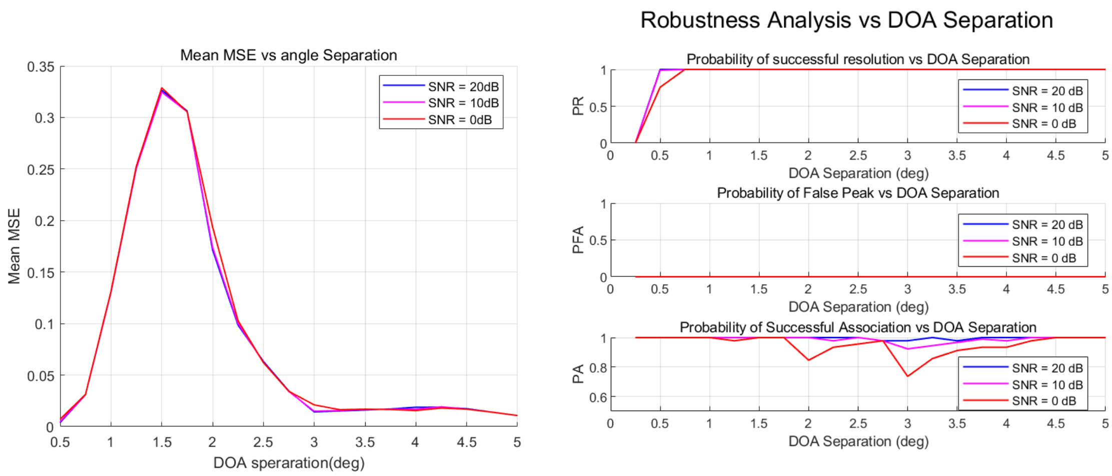

(a) Mean MSE versus DOA separation

(b) Robustness analysis versus DOA separation

Figure 4.11: Performance comparison under different SNR conditions.

Discussion: As the SNR decreases, the probability of a successful association P_{assoc} is noticeably

reduced, reflecting the increased difficulty of maintaining the consistency of the range and velocity across the apertures under strong noise. At the same time, the MSE also has a slight growth. However, both P_{res} and P_{nofalse} remain relatively stable, and the mean MSE exhibits only a moderate increase.
This behavior indicates that, while the data association is more sensitive to SNR, the DOA estimation stage itself remains relatively robust under a low SNR scenario. The reason is that the FMCW RV map formation involves coherent FFT integration across chirps, which introduces processing gain and effectively averages the noise power over the frequency domain. Similarly, the FOCUSS-based DOA estimation further averages the noise energy across the spatial frequency domain. As a result, the angular estimation benefits from a double layer of noise averaging, leading to better tolerance to low-SNR conditions.

4.5.4. Comparison III: Mono-static-Only vs. All-Aperture Processing

This comparison evaluates the performance difference between using only the two **mono-static apertures** ($\mathrm{M1}{\rightarrow}\mathrm{M1}$, $\mathrm{M2}{\rightarrow}\mathrm{M2}$) and using **all four apertures** , including the bi-static channels. Both configurations apply the same Block FOCUSS reconstruction and data-association procedure.

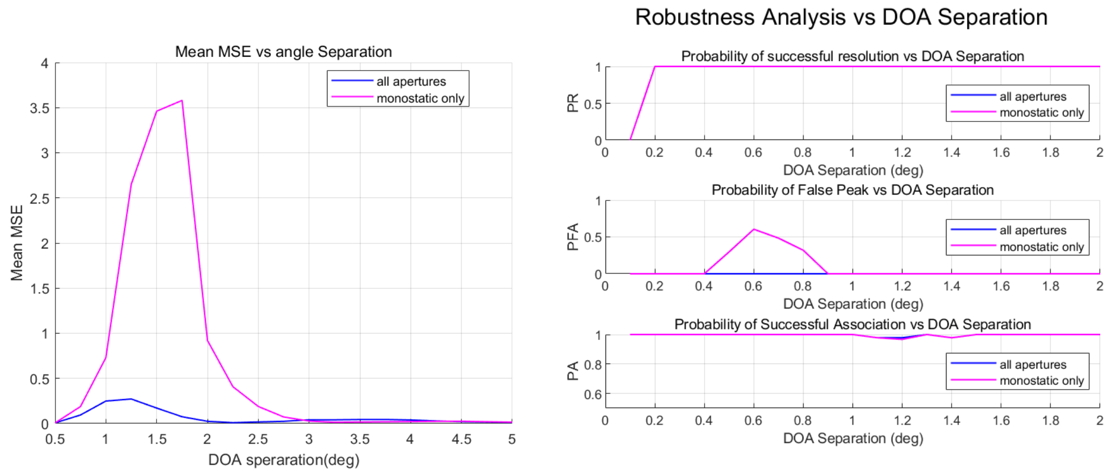

(a) Mean MSE versus DOA separation.

(b) Robustness metrics versus DOA separation.

Figure 4.12: Comparison between mono-static-only and all-aperture processing.

Discussion: As shown in Fig. 4.12, the mono-static case only suffers from a degraded resolution, a higher false-peak probability, and a larger mean MSE, especially when the angular separation is below $2°$. In contrast, combining all apertures provides greater spatial diversity and improved numerical stability, resulting in a lower estimation error and a more reliable target separation.

4.5.5. Comparison IV: Numerical-Stability Remedies

Finally, three numerical stabilization strategies are compared in the fine estimation stage: (1) *extra regularization*, (2) *sparse array configuration*, and (3) *non-uniform angular grid*. Figures 4.13a and 4.13b summarize the results.

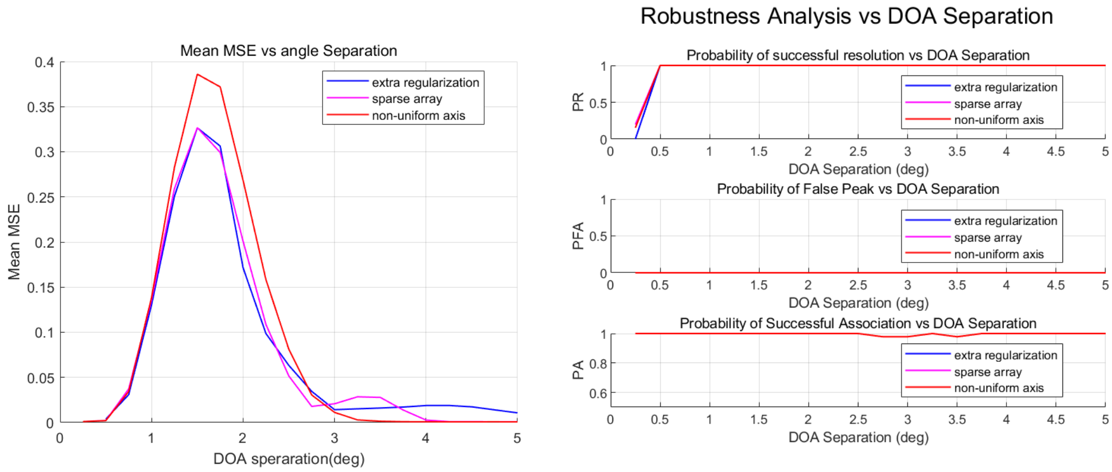

(a) Mean MSE versus DOA separation

(b) Robustness analysis versus DOA separation

Figure 4.13: Performance comparison under different numerical-stability remedies.

Discussion: All three methods maintain high P_{res} and P_{assoc} across the entire separation range. The non-uniform grid and sparse array configurations yield lower mean MSE in the moderate separation region ($1°$–$3°$) compared to the regularized solution, which slightly sacrifices resolution to improve conditioning. Overall, the *sparse array* and *non-uniform axis* methods provide better conditioning while preserving angular resolution, and the *extra regularization* serves as a robust fallback for extremely ill-conditioned cases.

4.5.6. Summary of Findings

Through the numerical comparisons presented in this section, several key findings can be summarized.

- **Sensitivity to Regularization:** The reconstruction accuracy of Block FOCUSS is sensitive to the choice of regularization parameters. Over-regularization leads to biased estimates, while under-regularization amplifies noise and instability. Adaptive weighting or normalization methods mitigate these effects and improve convergence consistency.
- **Numerical Stability:** The proposed stability remedies—matrix conditioning and normalization of the steering dictionary— effectively suppress numerical divergence in ill-conditioned cases and improve robustness against small-angle separations and high dynamic range scenarios.
- **Importance of Aperture Diversity:** Comparing the mono-static-only case with the all-aperture configuration shows that spatial diversity plays a critical role in maintaining stability and accuracy. Joint processing of all four apertures provides higher robustness, lower mean MSE, and better separation of closely spaced targets compared to using mono-static data only.
- **Overall Performance:** The enhanced Block FOCUSS framework achieves stable reconstruction performance under a wide range of conditions, offering an effective trade-off between computational cost and estimation accuracy.

Overall, the results confirm that aperture diversity and proper numerical conditioning are essential for reliable sparse reconstruction in distributed radar systems.

4.6. Conclusions

This chapter presented the experimental evaluation and comparative analysis of the proposed **Block FOCUSS-based coarse-to-fine sparse reconstruction framework** for distributed MIMO radar DOA estimation.

Several conclusions can be drawn from the simulation studies:

1. **The coarse-to-fine Block FOCUSS framework provides a flexible and efficient solution** for multi-aperture data fusion and high-resolution estimation. In contrast to a single-stage direct FOCUSS reconstruction, the proposed two-stage approach first performs coarse localization using traditional beamforming to identify a limited angular region of interest, followed by fine-grid FOCUSS reconstruction within that region. This hierarchical refinement significantly improves the angular resolution while reducing computational complexity.
2. **Numerical-stability remedies are crucial within the fine-stage reconstruction.** fine-grid processing operates on higher angular resolution , and thus encounters stronger dictionary correlation and ill-conditioning. Remedies such as steering-vector normalization and condition-number regulation effectively stabilize the iteration process, improving convergence, and reducing estimation bias when targets are closely spaced.
3. **The combination of apertures greatly enhances robustness.** The comparison between monostatic only and all-aperture processing demonstrated that full-aperture integration significantly reduces mean squared error and improves reliability under challenging noise and resolution conditions. Aperture diversity, together with the coarse-to-fine reconstruction scheme, enables accurate target separation and robust data association across channels.
4. **The proposed framework forms a solid foundation** for subsequent coherent processing. The insights gained here—particularly with respect to numerical conditioning, fine-grid reconstruction, and aperture diversity— directly support the phase-synchronization and coherent FOCUSS strategies developed in Chapter 5.

In summary, the results of this chapter validate the effectiveness of the **coarse-to-fine Block FOCUSS framework** and highlight the importance of numerical robustness, adaptive refinement, and multi-aperture diversity for achieving reliable high-resolution DOA estimation in distributed radar systems.

5

Coherent FOCUSS Fine Estimation

5.1. Modified Topology and Phase Compensation

Accurate phase alignment among apertures is essential for coherent DOA estimation. Even after system-level phase synchronization, each aperture experiences a distinct propagation path from the transmitter to the target and back to the receiver. These path-length differences introduce additional phase offsets that vary with the target angle. If not corrected, such differences distort the steering vector and degrade the coherent combination across apertures.

At $77\,\mathrm{GHz}$, the signal wavelength is approximately

$$\lambda = \frac{c}{f_c} \approx 3.9\ \mathrm{mm},$$

So, a path-length error of only a few millimeters can cause a phase deviation of several radians. Hence, even small geometric mismatches between apertures or targets not centered within a range cell lead to significant phase errors. That is why we introduced this nearfield modification in Sec.2.2. Figure 5.1 illustrates this nearfield geometry used for path-based phase correction.

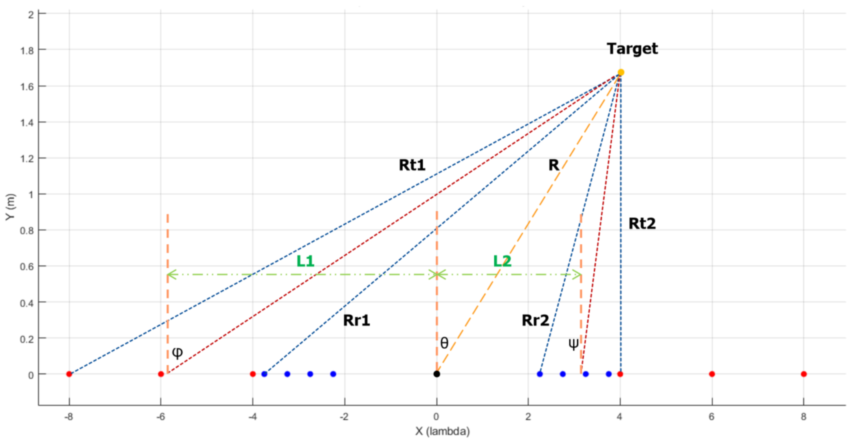

Figure 5.1: Near-field geometric model for path-based phase compensation.

To achieve accurate coherent processing, the phase of each aperture is compensated for according to its exact total propagation distance. Taking the first transmitter–receiver pair as a reference, the total paths for the four apertures are defined as

$$\begin{aligned} L_1 &= R_{t1} + R_{r1}, && \text{(M1}\rightarrow\text{M1, mono-static)} \\ L_2 &= R_{t2} + R_{r2}, && \text{(M2}\rightarrow\text{M2, mono-static)} \\ L_3 &= R_{t1} + R_{r2}, && \text{(M1}\rightarrow\text{M2, bi-static)} \\ L_4 &= R_{t2} + R_{r1}, && \text{(M2}\rightarrow\text{M1, bi-static)} \end{aligned} \tag{5.1}$$

where each term R_{tp} and R_{rp} represents the distance from transmitter p or receiver p to the target located at an angle θ_g on the global grid.

For each angle of the grid θ_g, the geometric distances are calculated as

$$\begin{aligned} R_{t1}(\theta_g) &= \sqrt{R_0^2 + l_{t1}^2 + 2R_0 l_{t1} \sin\theta_g}, \\ R_{r1}(\theta_g) &= \sqrt{R_0^2 + l_{r1}^2 + 2R_0 l_{r1} \sin\theta_g}, \\ R_{t2}(\theta_g) &= \sqrt{R_0^2 + l_{t2}^2 - 2R_0 l_{t2} \sin\theta_g}, \\ R_{r2}(\theta_g) &= \sqrt{R_0^2 + l_{r2}^2 - 2R_0 l_{r2} \sin\theta_g}, \end{aligned} \tag{5.2}$$

where R_0 is the nominal target range, l_{tp} and l_{rp} denote the transmitter and receiver positions along the baseline, and the $\pm$ signs indicate that the two radar nodes are located on opposite sides of the origin.

The corresponding phase-compensation terms are then given by

$$\begin{aligned} \beta_1(\theta_g) &= \frac{2\pi}{\lambda} L_1(\theta_g), \\ \beta_2(\theta_g) &= \frac{2\pi}{\lambda} L_2(\theta_g), \\ \beta_3(\theta_g) &= \frac{2\pi}{\lambda} L_3(\theta_g), \\ \beta_4(\theta_g) &= \frac{2\pi}{\lambda} L_4(\theta_g), \end{aligned} \tag{5.3}$$

and the corresponding complex phase-compensation factors applied to each aperture are

$$\Phi_p(\theta_g) = \exp[j\,\beta_p(\theta_g)]\,, \qquad p = 1,2,3,4. \tag{5.4}$$

The phase-compensation factor $\Phi_p(\theta_g)$ is applied element-wise to the steering matrix of each aperture. For aperture p, the original steering matrix $A_p(\theta_g)$ is defined in the global angle grid as

$$A_p = \big[a_p(\vartheta_p(\theta_1)),\, a_p(\vartheta_p(\theta_2)),\, \ldots,\, a_p(\vartheta_p(\theta_G))\big],$$

where $a_p(\vartheta_p(\theta_g)) \in \mathbb{C}^{N_p\times 1}$ is the steering vector of the p-th aperture for direction $\vartheta_p(\theta_g)$. After phase compensation, the corrected (coherently aligned) sensing matrix is obtained as

$$A_p^\star = \big[\, a_p(\vartheta_p(\theta_1))\, \Phi_p(\theta_1),\; a_p(\vartheta_p(\theta_2))\, \Phi_p(\theta_2),\; \ldots,\; a_p(\vartheta_p(\theta_G))\, \Phi_p(\theta_G) \,\big], \qquad p = 1,2,3,4. \tag{5.5}$$

This operation multiplies each steering vector by the corresponding complex phase factor $\Phi_p(\theta_g)$, thereby aligning the phase of all apertures at each angle of the grid θ_g. The resulting matrices $A_p^\star$ are then used to form the coherent stacked model $y_c = A_c x + n$ introduced in Section 5.2.

5.2. Coherent Model for DOA Estimation

In a distributed MIMO radar network, signals received from multiple mono-static and bi-static apertures can be coherently combined to form an **equivalent extended virtual array**. By treating all sub-apertures as parts of one coherent system, the effective aperture spans the entire baseline between the radars, resulting in a substantial improvement in angular resolution. This section introduces the mathematical formulation of the coherent model and its sparse reconstruction using the FOCUSS algorithm.

5.2.1. Array Definition and Phase-Compensated Steering Matrices

Let N_p denote the number of virtual elements in each aperture (here $N_p = 12$), and let G denote the number of discrete grid points on the global DoA grid $\boldsymbol{\theta} = \{\theta_g\}_{g=1}^{G}$. Each aperture $p \in \{1, 2, 3, 4\}$ has its own local angle mapping $\vartheta_p(\theta_g)$ that relates the global angle θ_g to the local angular coordinate of the aperture p. For example, $\vartheta_1(\theta) = \phi(\theta)$ and $\vartheta_2(\theta) = \psi(\theta)$, while the two bi-static apertures $\mathrm{M1}\to\mathrm{M2}$ and $\mathrm{M2}\to\mathrm{M1}$ use the corresponding local mappings defined by their geometry.

The steering *vector* of aperture p for direction $\vartheta_p(\theta_g)$ is

$$a_p\big(\vartheta_p(\theta_g)\big) \in \mathbb{C}^{N_p \times 1},$$

and the aperture's sensing *matrix* is obtained by horizontally stacking all steering vectors for the G points of the grid.

Each aperture requires an independent phase-compensation term that depends on the grid angle. Let $\beta_p(\theta_g)$ denote the aperture-dependent phase-compensation function associated with θ_g. The compensated sensing matrices are then defined as

$$A_p^{\star} = \big[\, a_p(\vartheta_p(\theta_1))e^{j2\pi\beta_p(\theta_1)},\ a_p(\vartheta_p(\theta_2))e^{j2\pi\beta_p(\theta_2)},\ \ldots,\ a_p(\vartheta_p(\theta_G))e^{j2\pi\beta_p(\theta_G)} \,\big] \in \mathbb{C}^{N_p \times G}. \tag{5.6}$$

Here, $\beta_p(\theta)$ encapsulates the geometric phase difference between transmitter, target, and receiver for each global angle and differs for all four apertures ($p = 1, 2, 3, 4$).

5.2.2. Coherent Observation Model

Let $y_p \in \mathbb{C}^{N_p \times 1}$ be the snapshot received in aperture p, and n_p the corresponding additive noise. After phase synchronization and per-aperture compensation, the coherent stacked model becomes

$$\underbrace{\begin{bmatrix} y_1 \\ y_3 \\ y_4 \\ y_2 \end{bmatrix}}_{y_c \in \mathbb{C}^{4N_p \times 1}} = \underbrace{\begin{bmatrix} A_1^{\star} \\ A_3^{\star} \\ A_4^{\star} \\ A_2^{\star} \end{bmatrix}}_{A_c \in \mathbb{C}^{4N_p \times G}} \underbrace{x}_{\in \mathbb{C}^{G \times 1}} + \underbrace{n}_{\in \mathbb{C}^{4N_p \times 1}}, \tag{5.7}$$

where x is the common sparse angular spectrum shared by all apertures, and A_c represents the equivalent *coherent sensing matrix* of the entire distributed system.

Notes.

- Each $a_p(\cdot)$ is an $N_p \times 1$ column vector; $A_p^{\star}$ is an $N_p \times G$ matrix formed by horizontally stacking G such vectors.
- The same N_p notation is used for the number of elements per aperture, consistent with the previous

sections.

- All four apertures include angle-dependent phase compensation $\beta_p(\theta)$.

5.2.3. Sparse Reconstruction via Coherent FOCUSS

With the coherent model (5.7), the DoA estimation problem is formulated as a sparse joint reconstruction on the global angle grid. The *coherent FOCUSS* algorithm solves for x using the following iterative reweighted ℓ_p-regularized least-squares formulation:

$$\hat{x} = \arg\min_{x} \frac{1}{2} \parallel y_c - A_c x \parallel_2^2 + \epsilon \sum_{g=1}^{G} |x_g|^{p_f}, \qquad 0 < p_f \leq 1, \tag{5.8}$$

By coherently stacking all aperture data and enforcing a common sparse support, the algorithm exploits the full distributed aperture as a single virtual unified array. This coherent model thus achieves higher angular resolution and improved robustness compared with noncoherent processing, as all phase-aligned measurements contribute constructively to the final DoA estimate.

5.3. Phase Synchronization

To enable the coherent model introduced in the previous section, all radar nodes must share a common phase reference. In practice, distributed systems experience unknown phase offsets between transmit–receive units, which must be estimated and compensated. This section presents the mathematical model and procedure for inter-system **phase synchronization**, a key step ensuring that data from different apertures can be coherently stacked for high-resolution DOA estimation[34].

5.3.1. Mathematical Model

Let y_{12} and y_{21} denote complex snapshots of the bi-static apertures corresponding to the transmission paths $\mathrm{M1} \to \mathrm{M2}$ and $\mathrm{M2} \to \mathrm{M1}$, respectively. Their observation models are

$$\begin{aligned} y_{12} &= e^{j\Delta} A_{12} x + n_{12}, \\ y_{21} &= e^{-j\Delta} A_{21} x + n_{21}, \end{aligned} \tag{5.9}$$

where A_{12} and A_{21} are the steering matrices of the bi-static apertures, x is the sparse angular coefficient vector, n_{12} and n_{21} are additive noise terms and Δ represents the unknown inter-system phase offset. The two channels are complex conjugates of each other, as the forward path introduces $e^{j\Delta}$, while the reverse path experiences $e^{-j\Delta}$. Mono-static channels are not affected by this offset.

5.3.2. Stacked Model and LS Estimator

Stacking the two bi-static observations yields

$$\begin{bmatrix} y_{12} \\ y_{21} \end{bmatrix} = \underbrace{\begin{bmatrix} e^{j\Delta} A_{12} \\ e^{-j\Delta} A_{21} \end{bmatrix}}_{B(\Delta)} x + n. \tag{5.10}$$

The least-squares (LS) objective is

$$J(\Delta, x) = \|y - B(\Delta)x\|_2^2, \tag{5.11}$$

and for a fixed Δ, the LS solution is

$$\hat{x}(\Delta) = (B^H(\Delta)B(\Delta))^{-1}B^H(\Delta)y. \tag{5.12}$$

Define

$$G = A_{12}^H A_{12} + A_{21}^H A_{21}, \tag{5.13}$$

then the profiled cost function is

$$\begin{aligned} J_{\text{prof}}(\Delta) &= \min_x \| y - Bx \|_2^2 = \| y - B\hat{x}(\Delta) \|_2^2 \\ &= \big\| (I - P_B) y \big\|_2^2 = y^H (I - P_B) y, \end{aligned} \tag{5.14}$$

$$\text{where} \quad P_B = B \big(B^H B\big)^{-1} B^H, \tag{5.15}$$

$$\begin{aligned} J_{\text{prof}}(\Delta) &= \|y\|_2^2 - y^H B(\Delta) \big(B^H(\Delta) B(\Delta)\big)^{-1} B^H(\Delta) y \\ &= \|y\|_2^2 - \underbrace{\big(B^H(\Delta) y\big)^H G^{-1} \big(B^H(\Delta) y\big)}_{Q(\Delta)}. \end{aligned} \tag{5.16}$$

Let

$$u = G^{-1/2} A_{12}^H y_{12}, \qquad v = G^{-1/2} A_{21}^H y_{21}. \tag{5.17}$$

$$\begin{aligned} \Rightarrow \; Q(\Delta) &= \Big\| G^{-1/2} \big(e^{-j\Delta} A_{12}^H y_{12} + e^{j\Delta} A_{21}^H y_{21}\big) \Big\|_2^2 \\ &= \Big\| e^{-j\Delta} \, u + e^{j\Delta} \, v \Big\|_2^2 \\ &= \|u\|_2^2 + \|v\|_2^2 + 2\, \Re\big\{ e^{j2\Delta} \, v^H u \big\}. \end{aligned} \tag{5.18}$$

Minimizing $J_{\text{prof}}(\Delta)$ is equivalent to maximizing $\Re\{e^{j2\Delta} v^H u\}$, which yields the closed-form estimator

$$\hat{\Delta} = \frac{1}{2} \angle(u^H v) = \frac{1}{2} \angle(y_{12}^H A_{12} G^{-1} A_{21}^H y_{21}). \tag{5.19}$$

After compensation,

$$\tilde{y}_{12} = e^{-j\hat{\Delta}} y_{12}, \qquad \tilde{y}_{21} = e^{j\hat{\Delta}} y_{21}, \tag{5.20}$$

the bi-static snapshots become phase-aligned with each other and with the mono-static channels.

5.3.3. Ambiguity Issue for $\Delta > \pi/2$

When the true phase offset satisfies $\Delta > \pi/2$, the estimator in (5.19) yields $\hat{\Delta} = \Delta - \pi$, introducing a π-ambiguity because the cosine term in the cost function is symmetric. This results in an incorrect sign for the estimated alignment and destroys coherent stacking.

$$\hat{\Delta}_{\text{amb}} = \hat{\Delta} \pm \pi. \tag{5.21}$$

To verify and correct the ambiguity, we evaluate whether the estimated $\hat{\Delta}$ satisfies the minimum of the cost function. Define the complex correlation metric

$$Z = y_{12}^H A_{12} G^{-1} A_{21}^H y_{21}, \tag{5.22}$$

then the estimated phase is

$$\hat{\Delta} = \frac{1}{2}\angle(Z), \tag{5.23}$$

and the alternative ambiguous solution is $\hat{\Delta} + \pi$. The correct solution is determined by re-evaluating the LS residual:

$$J_{\text{prof}}(\hat{\Delta}) \quad \text{and} \quad J_{\text{prof}}(\hat{\Delta} + \pi). \tag{5.24}$$

The value producing the smaller residual cost is selected as the valid synchronization phase. This ensures coherent alignment even when $\Delta > \pi/2$.

After disambiguation, the compensated snapshots become

$$\tilde{y}_{12} = e^{-j\hat{\Delta}_{\text{corr}}} y_{12}, \qquad \tilde{y}_{21} = e^{j\hat{\Delta}_{\text{corr}}} y_{21}, \tag{5.25}$$

where $\hat{\Delta}_{\text{corr}}$ is the estimate resolved with ambiguity.

5.3.4. Phase Synchronization Results

Two point targets located at $13°$ and $17°$ are simulated. The **left column** in Fig. 5.2 shows results using only the two bi-static apertures ($\mathrm{M1}{\to}\mathrm{M2}$ and $\mathrm{M2}{\to}\mathrm{M1}$), while the **right column** shows coherent processing with all four apertures. The **upper** plots correspond to the case before synchronization, where a random inter-system phase offset is introduced, and the **lower** plots show the results after phase alignment, where both targets are correctly localized.

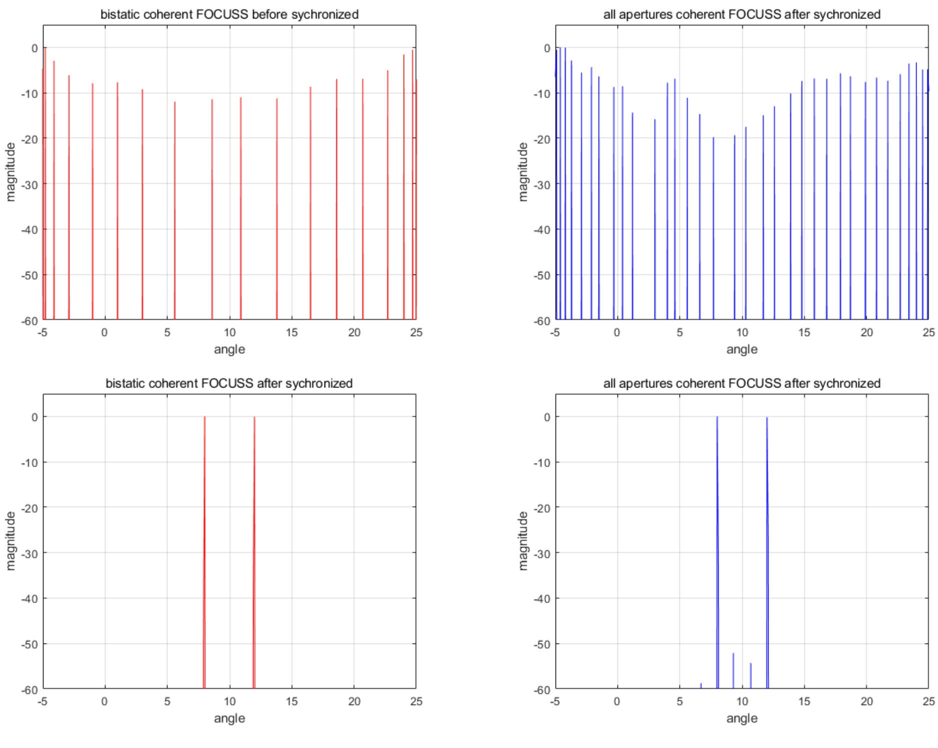

Figure 5.2: Phase synchronization results for $\Delta = 0.4410\pi$, $\hat{\Delta} = 0.4410\pi$.

Case 1: $\Delta < \pi/2$ (No Ambiguity).

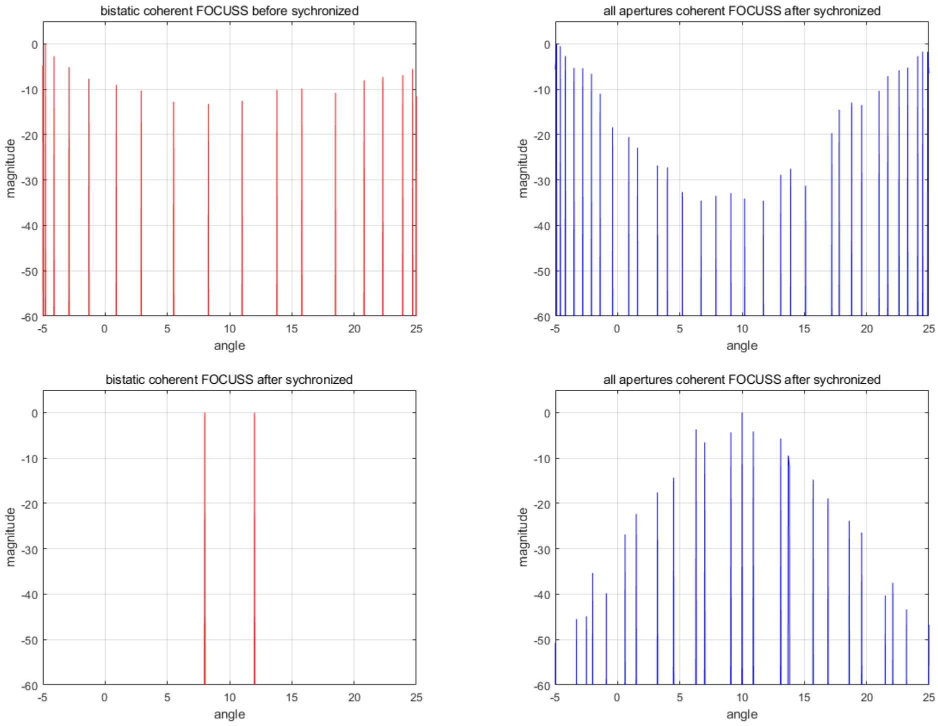

Figure 5.3: When $\Delta = 0.7529\pi$, the estimated $\hat{\Delta} = -0.2471\pi$, differing by π.

Case 2: $\Delta > \pi/2$ (Ambiguity Occurs).

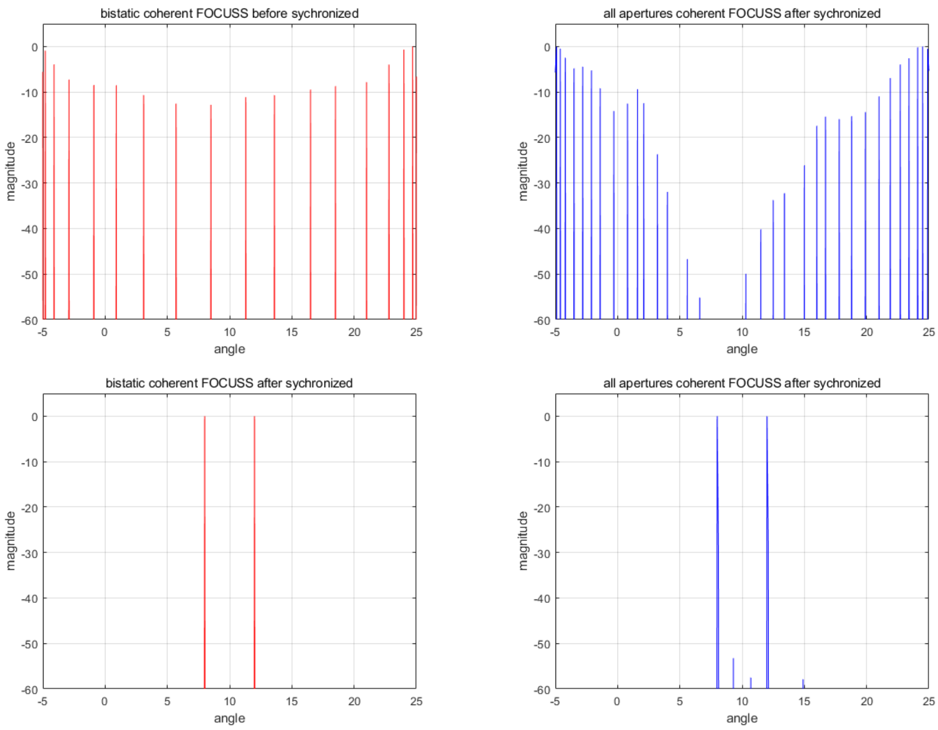

Figure 5.4: Ambiguity resolution results for $\Delta = 0.6600\pi$, $\hat{\Delta} = 0.6600\pi$.

Case 3: Ambiguity Resolved.

Case 4: Targets at different ranges. To evaluate the effect of range-dependent phase terms, three scenarios are tested in which the two targets remain at fixed DOAs but are placed at different distances ($100\,\mathrm{m}$, $60\,\mathrm{m}$, and $20\,\mathrm{m}$). Figure 5.5 shows that the synchronized coherent FOCUSS reconstruction remains stable across all distances. Even when the targets are moved as close as $20\,\mathrm{m}$, the reconstructed peaks remain well aligned, demonstrating that the proposed phase-synchronization model preserves robustness against range variation within the operating conditions of this study.

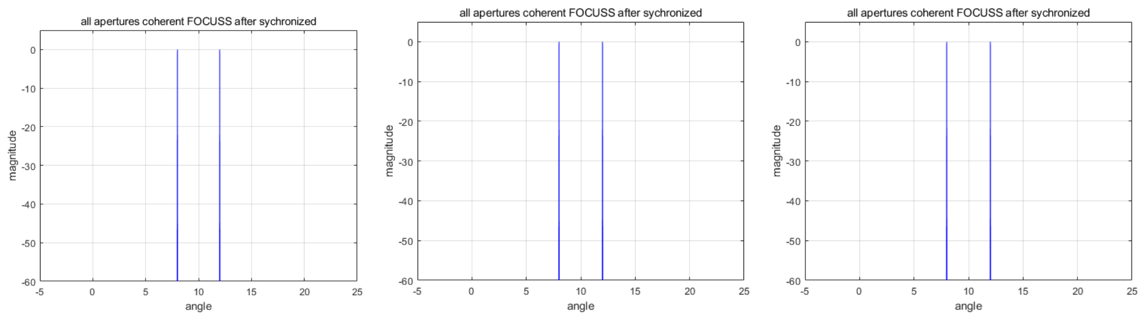

(a) $R = 100\,\mathrm{m}$ **(b)** $R = 60\,\mathrm{m}$ **(c)** $R = 20\,\mathrm{m}$

Figure 5.5: Coherent FOCUSS results under different target ranges.

Case 5: Different numbers of targets. To assess the scalability of phase synchronization, the number of targets is increased while keeping the baseline scenario remains unchanged. The initial DOA is fixed at 10° with a separation of 1.5°, and the number of targets is set to 2, 3, and 4. As shown in Fig. 5.6, the coherent FOCUSS reconstruction maintains stable peak locations without distortion or merging, indicating that the proposed synchronization model remains reliable even as the scene becomes more populated.

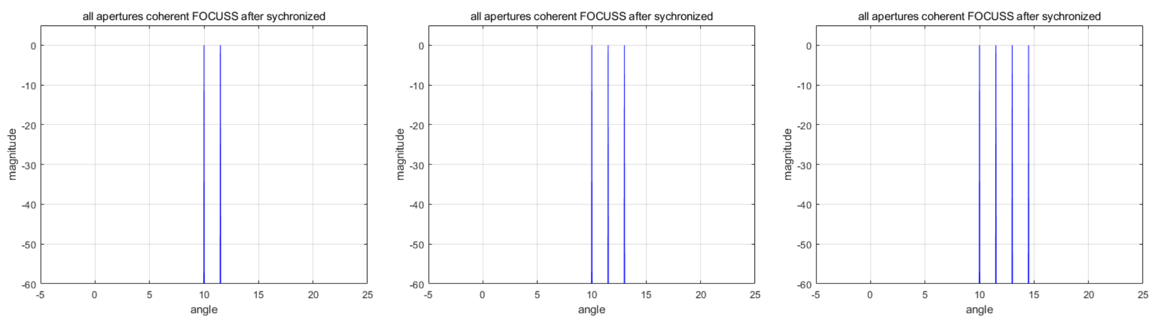

(a) 2 targets **(b)** 3 targets **(c)** 4 targets

Figure 5.6: Coherent FOCUSS results with increasing target numbers.

The results confirm that the proposed closed-form estimator successfully retrieves the phase offset between systems Δ. Even when $\Delta > \pi/2$, the ambiguity validation and correction procedure ensures that all apertures remain phase-synchronized, allowing coherent FOCUSS reconstruction to exploit the full virtual aperture for improved angular resolution.

5.4. Ambiguity Function in Coherent Model

The angular ambiguity function (AF) provides an intuitive way to assess and compare the angular resolution capability of different array configurations. For a given steering matrix $\mathbf{A}(\theta)$, the normalized ambiguity function is defined as

$$\mathrm{AF}(\theta_1, \theta_2) = \frac{\left|\mathbf{a}^H(\theta_1)\mathbf{a}(\theta_2)\right|}{\|\mathbf{a}(\theta_1)\|_2 \, \|\mathbf{a}(\theta_2)\|_2}, \tag{5.26}$$

where $\mathbf{a}(\theta)$ denotes the direction θ of the array steering vector. AF measures the similarity between the responses of the arrays from two different directions and therefore determines the ability of the array to distinguish nearby sources.

Traditionally, for methods such as beamforming or MUSIC, the 3-dB mainlobe width of the AF indicates the theoretical resolution limit. However, in sparse reconstruction methods such as FOCUSS, which exploit sparsity priors to achieve *super-resolution*, the actual achievable angular resolution often surpasses that implied by the AF width. Nevertheless, since the aperture size directly influences the array manifold, the AF remains a valuable tool for visualizing and comparing the effective angular resolving power under different coherent configurations.

5.4.1. Case I: Baseline Length = 16λ

Figure 5.7 shows the physical and virtual array layouts when the inter-radar baseline is 16λ. In this configuration, the virtual apertures of the four signal paths ($\mathrm{M1}\to\mathrm{M1}$, $\mathrm{M2}\to\mathrm{M2}$, $\mathrm{M1}\to\mathrm{M2}$, $\mathrm{M2}\to\mathrm{M1}$) form a continuous uniform linear array (ULA) without gaps. As shown in Fig. 5.8, the coherent combination of all apertures corresponds to an effectively longer array, resulting in a narrower AF mainlobe and improved angular resolution. The single-aperture AF (blue) has the widest mainlobe, the bi-static coherent case (orange) offers intermediate performance, and the fully coherent all-aperture AF (green) achieves the sharpest mainlobe with negligible sidelobes.

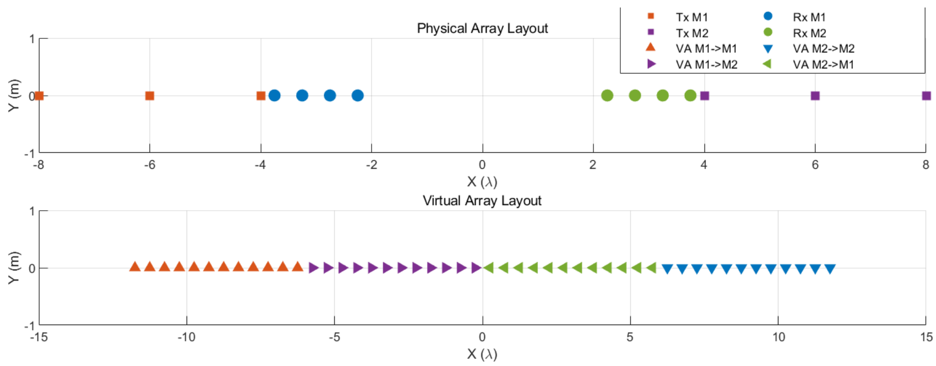

Figure 5.7: Physical and virtual array layouts for baseline length 16λ.

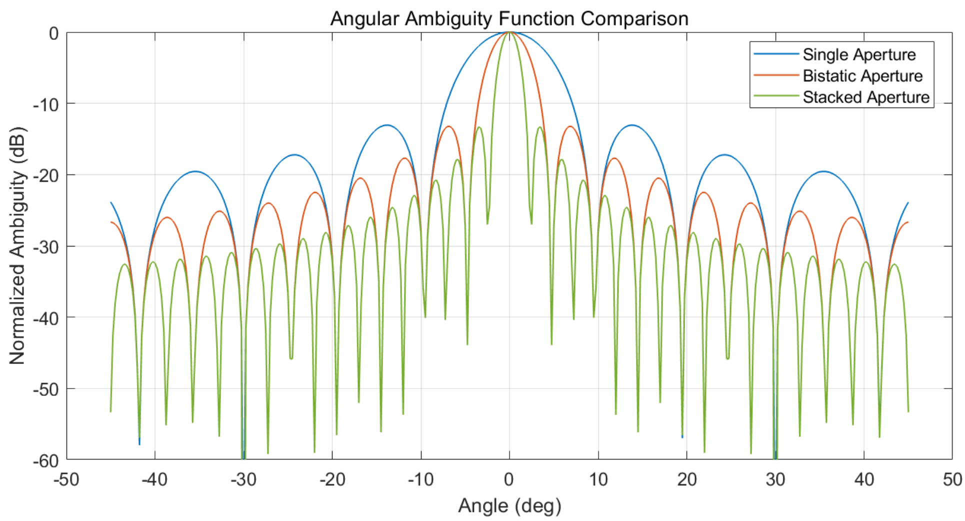

Figure 5.8: Angular ambiguity functions for different coherent configurations with baseline length 16λ.

5.4.2. Case II: Baseline Length = 68λ

When the baseline extends to 68λ, the geometry of the array changes significantly. As shown in Fig. 5.9, the physical separation between M1 and M2 creates noticeable gaps in the equivalent virtual array. The bi-static virtual apertures ($\mathrm{M1}{\rightarrow}\mathrm{M2}$ and $\mathrm{M2}{\rightarrow}\mathrm{M1}$) remain continuous, while the mono-static ones are spatially isolated. This discontinuity causes prominent sidelobes in general AF, as illustrated in Fig. 5.10. The green curve (all-aperture coherent) still provides the narrowest mainlobe, but sidelobe levels rise because of the discontinuous aperture structure. In contrast, the bi-static-only case maintains a smoother sidelobe envelope, reflecting its more contiguous virtual array.

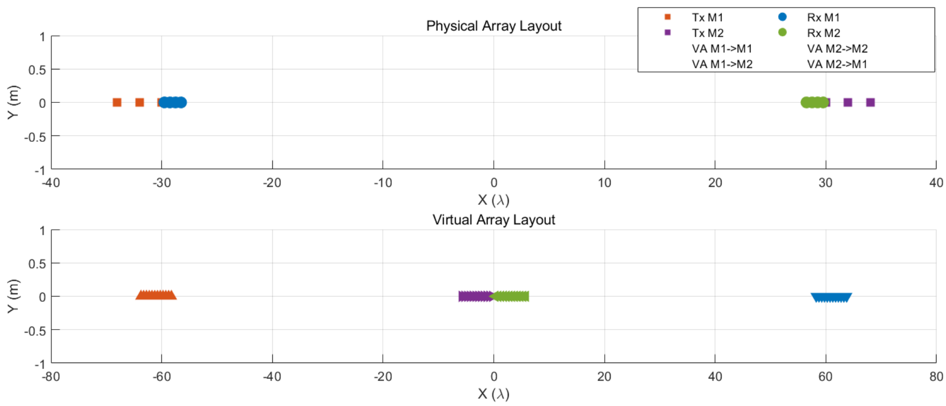

Figure 5.9: Physical and virtual array layouts for baseline length 68λ.

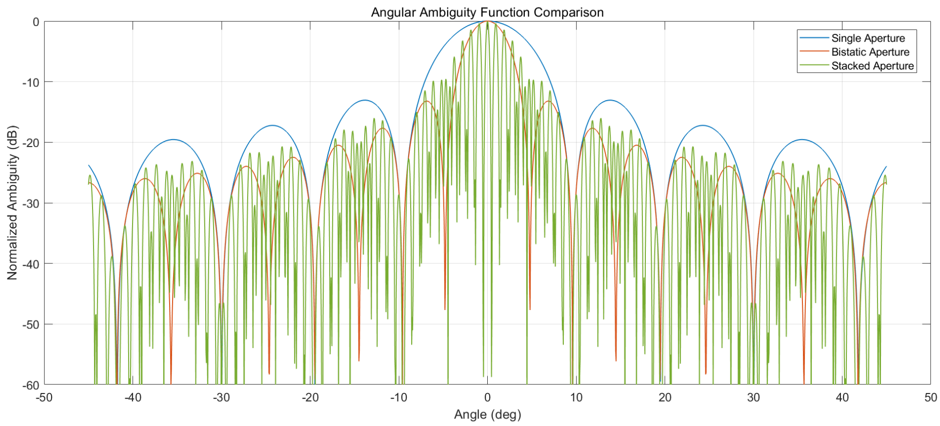

Figure 5.10: Angular ambiguity functions for different coherent configurations with baseline length 68λ.

5.4.3. Analysis of AF Characteristics

From these results, several observations can be made. The width of the mainlobe of the AF is primarily determined by the *total baseline length*, while the sidelobe envelope depends on the *effective continuous aperture region*. In Fig. 5.10, the fully coherent AF envelope lies between the mono-static-only and bi-static-only configurations. This is because the effective continuous apertures consist of two bi-static sub-arrays of size 24×1 and two mono-static arrays of size 12×1. For comparison, Fig. 5.11 shows the AF using only mono-static apertures, where the effective virtual aperture length is merely 12×1, leading to an AF curve that completely overlaps with the case of single-aperture.

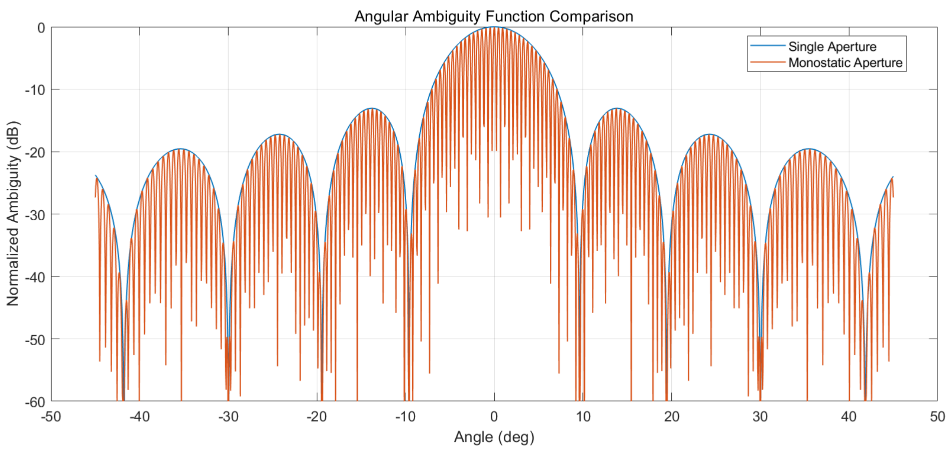

Figure 5.11: Angular ambiguity function using only mono-static apertures.

5.4.4. Summary

In summary, AF analysis reveals that excessively large baseline lengths introduce discontinuities in the virtual array, resulting in strong sidelobes and degraded angular performance. Conversely, moderate baselines such as 16λ allow the sub-apertures to form a continuous coherent aperture, achieving a favorable balance between resolution and sidelobe suppression. This observation is consistent with later simulation results, where coherent FOCUSS with smaller baselines demonstrates superior accuracy and stability compared to the large-baseline case.

5.5. Performance and Results Comparison

This chapter evaluates the performance of the **coherent FOCUSS** model for fine DOA estimation. Except for the phase-related processing steps, the simulation protocol follows exactly the same assumptions as in Chapter 4. The Monte-Carlo simulation setup is also the same except that the angular separation grid $\Delta\theta$ is set to $(0.1°, 2°)$ with the step of $0.1°$ to get a better resolution comparison. The main differences between the two models originate from the coherent combination of the four apertures.

Coherent virtual-array construction. In each Monte-Carlo realization, snapshots from the four physical apertures (M1→M1, M2→M2, M1→M2, M2→M1) are stacked into a single coherent virtual array after applying:

1. **inter-radar phase synchronization**, and
2. **geometric phase-path compensation** derived in Chapter 3.

This produces a globally phase-aligned virtual array for coherent sparse reconstruction.

Randomized inter-radar phase offsets. To test the robustness of the synchronization procedure, a random inter-radar phase offset is performed.

$$\phi_{\text{offset}} \sim \text{Unif}(0, 2\pi)$$

is injected between the two radar systems in every Monte-Carlo realization. This emulates independent oscillators and verifies the feasibility of the phase-alignment method.

Evaluation aspects. The coherent model is analyzed under: (i) comparison with non-coherent Block FOCUSS, (ii) variations in target range, (iii) SNR levels, (iv) numerical-stability remedies, (v) different target RCS ratios, and (vi) different baseline lengths. These experiments demonstrate the strengths and trade-offs of coherent processing in distributed MIMO radar systems.

5.5.1. Comparison Between Coherent and Non-coherent Models

Figures 5.12 and 5.13 show the performance comparison between the coherent and block-based FOCUSS frameworks. Since both models share identical data-association strategies, the association success rate is omitted from the comparison. As shown in Fig. 5.12, the coherent FOCUSS model consistently achieves a much lower mean MSE across all DOA separations. This improvement comes from the coherent phase alignment among the apertures, which effectively enlarges the equivalent aperture and suppresses residual phase errors. In the robustness plots (Fig. 5.13), the coherent FOCUSS achieves a probability of successful resolution (P_{SR}) close to 1 even for separations below $1°$, whereas the non-coherent block FOCUSS fails to distinguish targets when angular separation is small. These results confirm that coherent reconstruction offers significantly improved angular resolution and robustness without degrading the false-alarm rate.

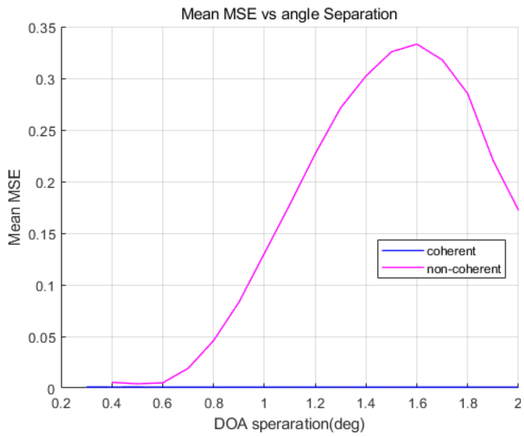

Figure 5.12: Mean MSE vs. DOA separation for Block FOCUSS and coherent FOCUSS.

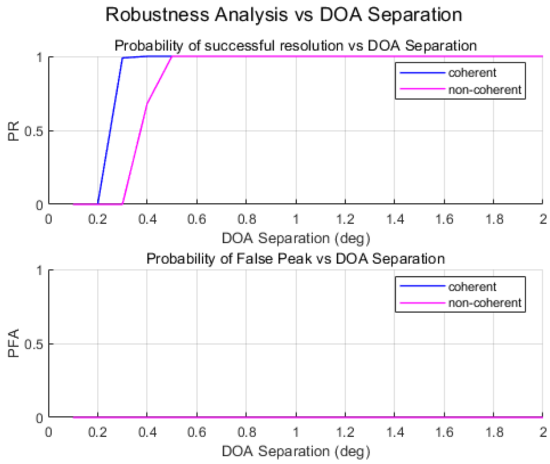

Figure 5.13: Robustness analysis vs. DOA separation for Block FOCUSS and coherent FOCUSS.

5.5.2. Performance at Different Target Ranges

Figures 5.14 and 5.15 illustrate the coherent performance of FOCUSS at different target distances ($R = 20$ m, 60 m, and 100 m). To emphasize the capability of close-target resolution, the DOA separation axis is limited to $0–2°$. The results in Fig. 5.14 show that the mean MSE remains on the order of 10^{-3} across all ranges, indicating stable reconstruction even for nearby targets. The corresponding robustness curves in Fig. 5.15 reveal that the probability of successful resolution reaches 1 when the separation exceeds $0.3°$, and the probability of false peaks remains negligible for all ranges. This shows that the coherent FOCUSS maintains strong robustness to range-dependent phase variations and performs reliably even in short-range scenarios.

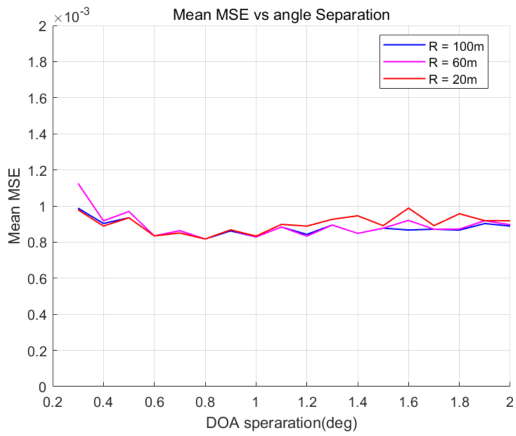

Figure 5.14: Mean MSE vs. DOA separation

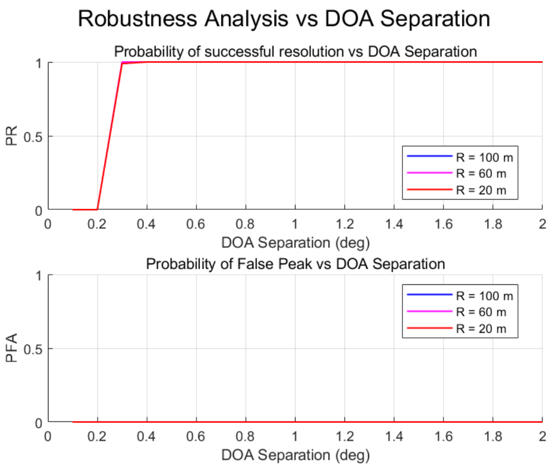

Figure 5.15: Robustness analysis vs. DOA separation

Figure 5.16: Performance comparison at different target ranges (coherent model).

5.5.3. Performance at Different SNR Levels

Figures 5.17 and 5.18 show the coherent model performance at SNRs levels of 0 dB, 10 dB, and 20 dB. Even at low SNRs, the mean MSE (Fig. 5.17) remains below 10^{-3}, indicating that the coherent processing scheme effectively preserves phase integrity and mitigates noise-induced fluctuations. The robustness results in Fig. 5.18 show nearly identical probabilities of successful resolution and zero false peaks for all SNRs above 0 dB, confirming the high noise tolerance of the coherent reconstruction.

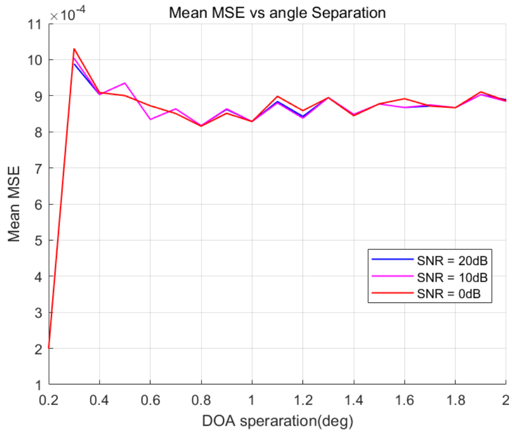

Figure 5.17: Mean MSE vs. DOA separation.

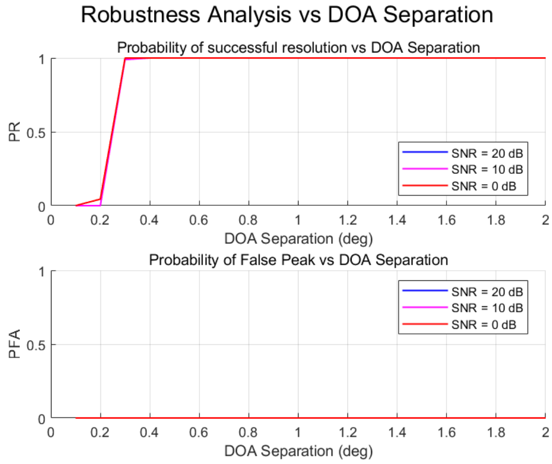

Figure 5.18: Robustness analysis vs. DOA separation.

Figure 5.19: Performance comparison at different SNR levels (coherent model).

5.5.4. Effect of Numerical Solutions

Finally, Figures 5.20 and 5.21 present the performance comparison between three numerical-stability remedies applied within the coherent model: (i) dictionary normalization with extra regularization, (ii) sparse matrix formulation and (iii) non-uniform correction on the axes. As observed in Fig. 5.20, all three methods maintain a similar level of MSE and robustness across separations, indicating that they effectively prevent numerical divergence. Among them, the "extra regularization" approach achieves slightly lower stability around small separations ($< 0.4°$), due to the regularization-induced bias that mildly broadens the mainlobe. Nevertheless, Fig. 5.21 confirms that all three strategies maintain a near-perfect resolution probability and zero false-peak occurrence, validating their robustness for practical coherent reconstruction.

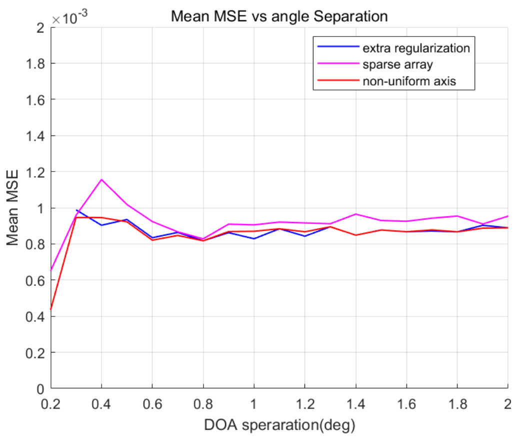

Figure 5.20: Mean MSE vs. DOA separation

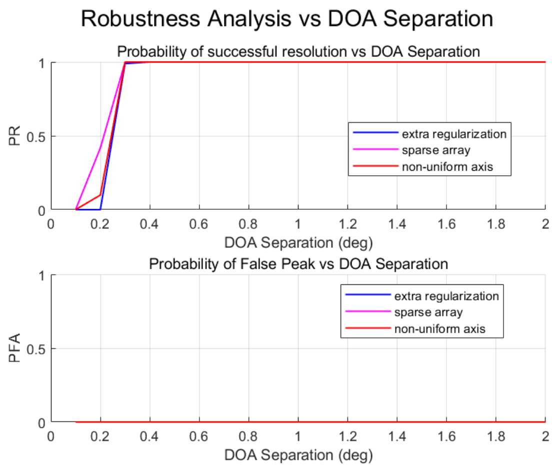

Figure 5.21: Robustness analysis

Figure 5.22: Performance comparison under different numerical solutions (coherent model).

5.5.5. Performance with Targets of Different RCS

In previous evaluations, all targets were assumed to have identical radar cross sections (RCS). To further investigate the robustness of both reconstruction models, this section examines the scenario in which two targets exhibit different RCS values with power differences of $\Delta\mathrm{RCS} = 0\ \mathrm{dB}$, $10\ \mathrm{dB}$, and $20\ \mathrm{dB}$.

Figures 5.23 and 5.24 show the results of the non-coherent Block FOCUSS model under varying RCS differences. It can be observed that the performance of the non-coherent approach is highly sensitive to RCS imbalance.

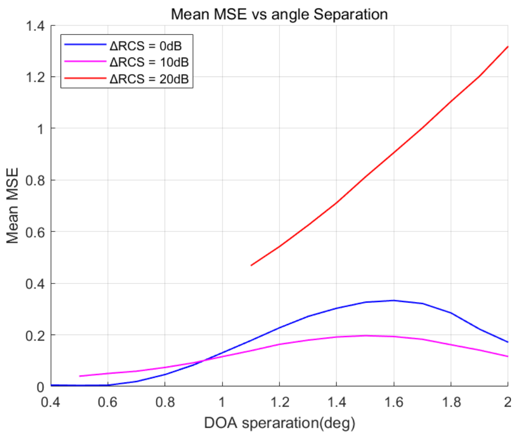

Figure 5.23: Mean MSE vs. DOA separation

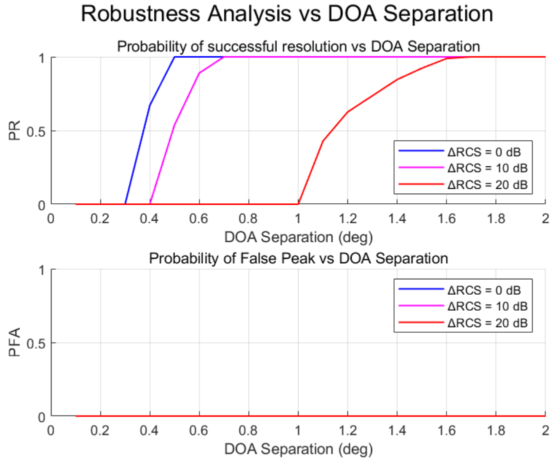

Figure 5.24: Robustness analysis vs. DOA separation

Figure 5.25: Performance comparison for different RCS differences (Block FOCUSS).

For large $\Delta\mathrm{RCS}$ values (e.g. $20\ \mathrm{dB}$), the mean MSE increases significantly, and the probability of successful resolution (P_{SR}) decreases sharply. In the non-coherent (block) model, each aperture is processed independently and fused in power:

$$Z_{\text{nc}}(g) \propto \sum_p \left|\mathbf{a}_p^H(\theta_g)\mathbf{y}_p\right|.$$

For two targets with amplitudes $|\alpha_s| \gg |\alpha_w|$, the snapshot in the weak target grid is

$$\mathbf{a}_p^H(\theta_w)\mathbf{y}_p \simeq \alpha_w + \alpha_s\,\rho_p(g_w, g_s) + \eta_p, \quad \rho_p(g_w, g_s) = \mathbf{a}_p^H(\theta_w)\mathbf{a}_p(\theta_s).$$

Because Z_{nc} fuse magnitudes rather than coherent phases, the leakage term $|\alpha_s\rho_p|$ from the strong target is added constructively across the apertures. When $|\alpha_w| < |\alpha_s|\overline{|\rho_p|}$, the weak target peak is masked, leading to biased estimation and loss of resolution. This effect is amplified in FOCUSS updates, where weaker components receive smaller reweighting factors and are further attenuated.

Figures 5.26 and 5.27 show the corresponding results for the coherent FOCUSS model under the same RCS conditions. In the coherent model, phase alignment ensures that signals from all apertures combine coherently before power evaluation:

$$Z_{\text{c}}(g) \propto \left|\sum_p \mathbf{a}_p^H(\theta_g)\mathbf{y}_p\right|.$$

Thus, the leakage terms of the strong targets partially cancel due to phase diversity, and the weak target's contribution is reinforced coherently across the apertures. This joint phase-preserving fusion maintains the sparsity structure of $\mathbf{x}$ and mitigates the dominance of high-RCS components, making the coherent model less sensitive to $\Delta\mathrm{RCS}$ variations. Residual degradation at large $\Delta\mathrm{RCS}$ arises mainly from the weighting bias in the FOCUSS iterations that favors stronger amplitudes.

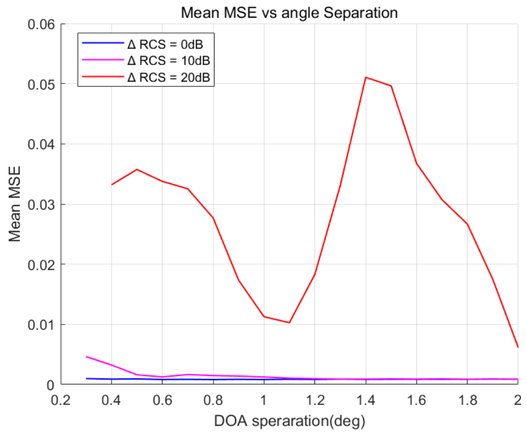

Figure 5.26: Mean MSE vs. DOA separation.

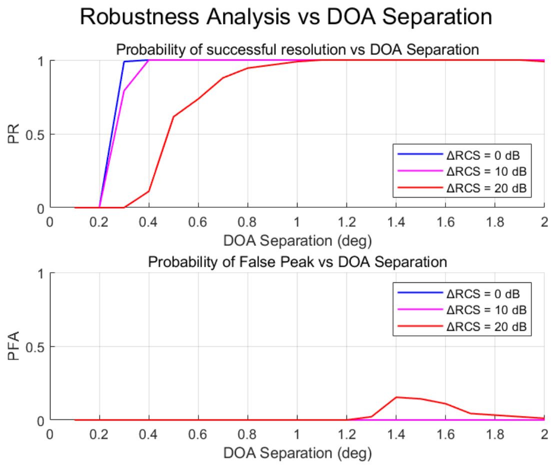

Figure 5.27: Robustness analysis vs. DOA separation.

Figure 5.28: Performance comparison for different RCS differences (coherent model).

5.5.6. Effect of Baseline Length in Coherent Model

Next, we investigate the influence of the radar baseline length L on coherent reconstruction performance. For the non-coherent Block FOCUSS model, the baseline length has negligible impact since signals are processed independently without exploiting cross-aperture phase relations. In contrast, for the coherent model, the baseline length plays a critical role due to the phase-coherent fusion mechanism across distributed sub-apertures.

From the analysis of the ambiguity function in Section 5.4, it was shown that an increased baseline enlarges the virtual aperture, but also widens the spatial sampling gaps between sub-apertures. This leads to more pronounced sidelobes and stronger phase sensitivity. Figures 5.29 and 5.30 illustrate the performance of the coherent FOCUSS model for the baseline lengths of $L = 16\lambda$, 36λ and 68λ. As seen in Fig. 5.29, larger baselines induce severe performance fluctuations, with significantly higher mean MSE and reduced angular resolution. This can be attributed to the sidelobe coupling effect: when the baseline becomes excessively large, the columns of the steering dictionary $\mathbf{a}(\theta)$ become less correlated for small θ, causing unstable sparse recovery and local minima in the solution.

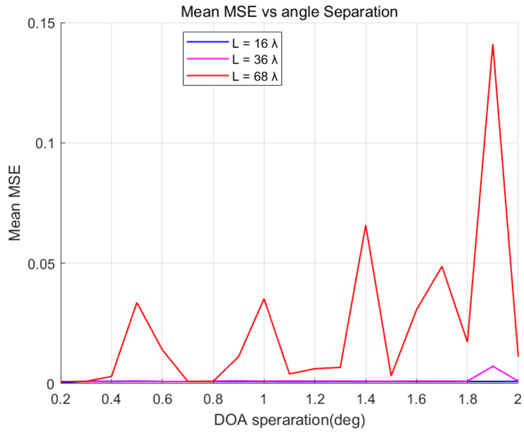

Figure 5.29: Mean MSE vs. DOA separation.

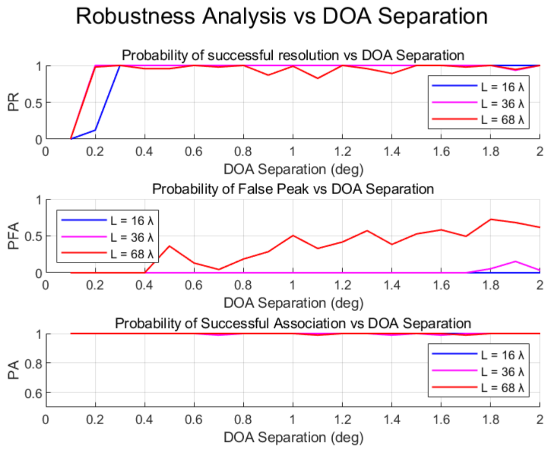

Figure 5.30: Robustness analysis vs. DOA separation.

Figure 5.31: Performance comparison for different baseline lengths (coherent model).

The robustness curves in Fig. 5.30 further confirm this observation. For $L = 68\lambda$, both the probability of no false peak $(1 - P_{\mathrm{FA}})$ and the probability of successful association (P_{A}) drop substantially, indicating that sidelobe artifacts interfere with association consistency. However, too small a baseline (e.g. $L < 16\lambda$) is undesirable in practice since closely spaced radar systems may suffer from mutual coupling and near-field interference. Therefore, a moderate baseline offers a trade-off between angular resolution and system robustness. Research on mitigating sidelobe effects under large-baseline conditions will be discussed in further detail in the next chapter.

5.6. Conclusions

This chapter introduced the **coherent FOCUSS** framework for the fine DOA estimation stage. Building on the non-coherent results of Chapter 4, it established the phase synchronization and compensation models required to coherently fuse multiple mono-static and bi-static apertures.

The proposed coherent formulation effectively transforms all sub-apertures into a single extended virtual array, significantly increasing the angular resolution and estimation accuracy. Through both analytical modeling and Monte Carlo simulations, it was demonstrated that coherent fusion yields superior MSE performance, sharper angular discrimination, and higher robustness at low SNR and short ranges.

The ambiguity function analysis confirmed that aperture continuity rather than total baseline length dominates the main-lobe envelope, while excessive baseline extension introduces pronounced sidelobes that degrade stability. Performance studies further revealed that the coherent model remains resilient to moderate RCS variations between targets, outperforming non-coherent fusion, though extreme power imbalance can still bias sparse reconstruction due to FOCUSS reweighting effects.

Overall, the results validate the advantages of coherent reconstruction in distributed radar networks: it achieves enhanced resolution and stability by exploiting inter-aperture phase information, while highlighting the need for precise synchronization and controlled baseline design. These findings form the basis for the advanced coherence optimization and sidelobe-mitigation strategies developed in the next chapter.

6

Sidelobe Suppression in a Large Baseline Situation

This chapter addresses the degradation of coherent DOA estimation when the bi-static baseline becomes excessively large and introduces a modified array configuration to mitigate the resulting sidelobe problem. As discussed in Section 5.5, although a large baseline extends the virtual aperture and enhances angular resolution, it also causes severe array non-uniformity and missing elements in the virtual array, leading to strong and irregular sidelobes that distort coherent FOCUSS reconstruction.

Fig. 6.1 illustrates this effect for a baseline of 68λ, where two targets are located at 29° and 31°. Although the mainlobes appear near the true DOAs, multiple spurious sidelobes emerge around them, indicating that direct coherent stacking under a large baseline condition severely degrades reconstruction performance.

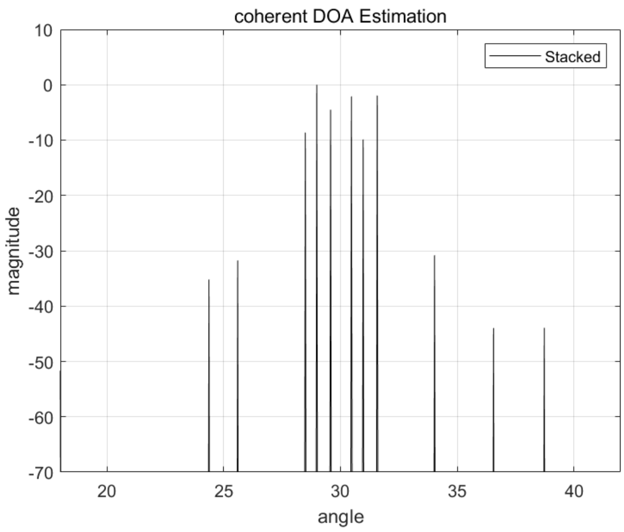

Figure 6.1: Coherent DOA estimation result under a large baseline (68λ) with two targets at 29° and 31°.

In array signal processing, sidelobe suppression has been widely studied to improve beam pattern quality and robustness. A classical approach is the use of window functions to weight the elements of the array, as discussed in [35]. Such tapering designs, including Chebyshev and Hann windows, effectively reduce sidelobe levels by smoothing the aperture weighting but at the cost of broadened mainlobes and degraded angular resolution. While recent studies have extended window design to non-uniform MIMO arrays, these methods mainly focus on single-platform systems and uniform aperture weighting. and thus are not directly applicable to distributed radar configurations with large baselines. In addition, for super-resolution sparse reconstruction methods such as FOCUSS, where spectral peaks are extremely narrow and discrete, window-based sidelobe suppression is largely ineffective because it acts on continuous beam patterns rather than sparse spectra.

Another direction of research involves optimization-based beamforming methods. For example, a sparse constraint has been introduced in time-domain broadband beamforming to enforce a sparse response in sidelobe regions [36]. This approach can significantly lower sidelobe levels and improve robustness against steering-vector mismatch, but it relies on convex optimization with high computational complexity and is primarily developed for single-array broadband systems.

Similarly, robust sidelobe cancellers constrained by subspace have been proposed to maintain mainlobe integrity under DOA mismatch conditions [37]. By projecting the desired steering vector onto an orthogonal subspace, these methods enhance robustness and suppress interference. However, they also require prior knowledge of the signal sector and are limited to monostatic array configurations.

In contrast, for large-baseline distributed MIMO radar systems employing coherent sparse reconstruction, existing sidelobe suppression strategies are still limited. The combination of inter-radar phase alignment, sparse virtual aperture synthesis, and wide-field-of-view processing introduces new sidelobe characteristics that are not well addressed by traditional windowing or convex optimization methods. This motivates the development of modified array configurations and tailored processing schemes to effectively suppress sidelobes in such large-baseline coherent systems.

The goal of this chapter is therefore to modify the array configuration and the corresponding coherent processing scheme such that the sidelobe energy is effectively suppressed while maintaining the resolution advantage of a large baseline.

6.1. Ambiguity Function for Different Array Gap

To further analyze the influence of the spacing of the elements d on the characteristics of the sidelobes in the coherent configuration, the ambiguity functions are compared under different array gaps. Figs. 6.2–6.5 show the results when the overall baseline is fixed at 68λ, while the inter-element spacing d is set to 0.5λ, λ, 2λ and 2.5λ, respectively.

As d increases, the matrix becomes sparser, and the sidelobes around the mainlobe are gradually compressed, leading to a narrower and more concentrated mainlobe. This phenomenon occurs because larger spacing enhances the effective aperture of each sub-aperture, which increases angular selectivity. However, this benefit comes at the cost of introducing grating lobes, whose positions depend on d and can severely interfere with target localization if they fall within the field of view (FOV).

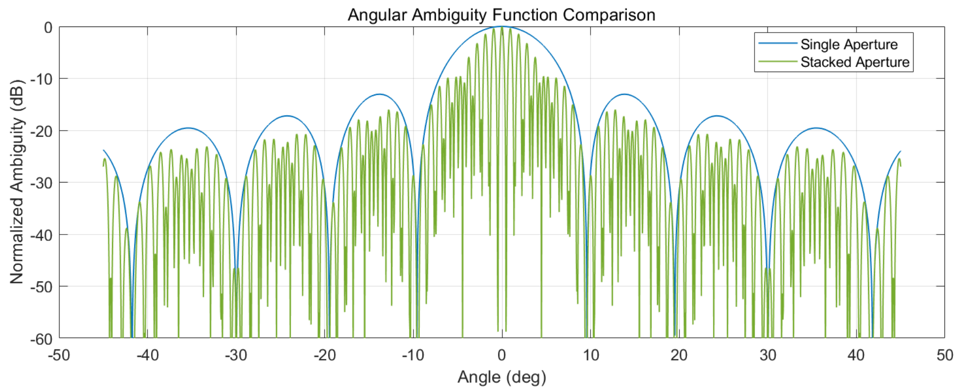

Figure 6.2: Angular ambiguity function comparison when $d = 0.5\lambda$ (benchmark configuration).

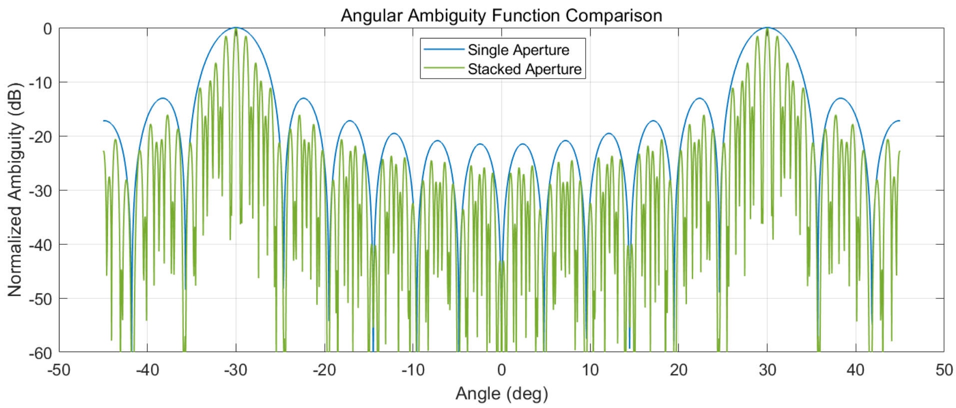

Figure 6.3: Angular ambiguity function comparison when $d = \lambda$.

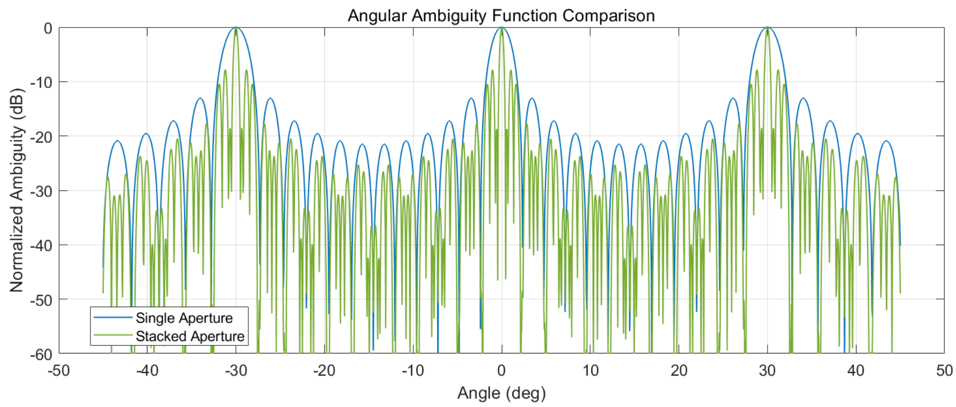

Figure 6.4: Angular ambiguity function comparison when $d = 2\lambda$.

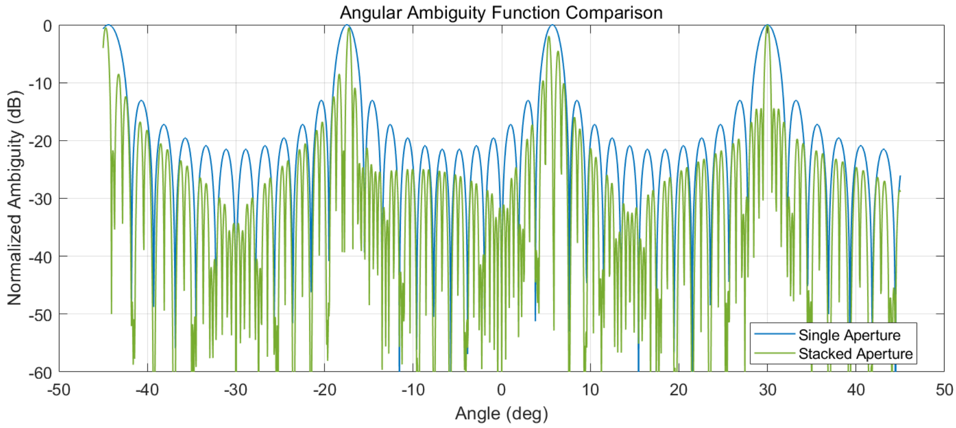

Figure 6.5: Angular ambiguity function comparison when $d = 2.5\lambda$.

The relationship between the position of the grating lobe and the spacing of the elements d has been derived in Eq. (4.29), expressed as:

$$\sin\theta_g = \sin\theta_0 + m\frac{\lambda}{d}, \quad m = \pm 1, \pm 2, \dots \tag{6.1}$$

where θ_0 and θ_g denote the mainlobe and grating-lobe directions, respectively. To ensure that the grating lobes do not enter the FOV of the fine estimation stage, the angular separation between the mainlobe and its nearest grating lobe must be greater than the FOV limit. The minimum separation $\Delta\theta_{\min}$ can be analytically obtained as follows:

$$\Delta\theta\left(\theta_0\right) \triangleq \min_{m=\pm 1} |\theta_g - \theta_0| = \min_{m=\pm 1} \left|\arcsin\left(\sin\theta_0 + ms\right) - \theta_0\right|, \quad \text{where } s = \frac{\lambda}{d}. \tag{6.2}$$

By taking the derivative of $\Delta(\theta_0)$ with respect to θ_0 and finding its stationary point, we obtain the following:

$$\frac{d\Delta}{d\theta_0} = 1 - \frac{\cos\theta_0}{\sqrt{1 - (\sin\theta_0 - s)^2}} = 0, \tag{6.3}$$

which yields the minimum angular separation as:

$$\Delta\theta_{\min} = 2\arcsin\left(\frac{\lambda}{2d}\right). \tag{6.4}$$

Fig. 6.6 plots $\Delta\theta_{\min}$ as a function of normalized spacing d/λ. It can be observed that as d increases, the minimum angular separation between the mainlobe and the first grating lobe decreases rapidly. For example, when $d = 2\lambda$, $\Delta\theta_{\min} \approx 29^\circ$, while for $d = 2.5\lambda$, $\Delta\theta_{\min} \approx 23^\circ$. Therefore, to avoid grating lobes entering the FOV during fine estimation, the angular search range should be constrained within these limits.

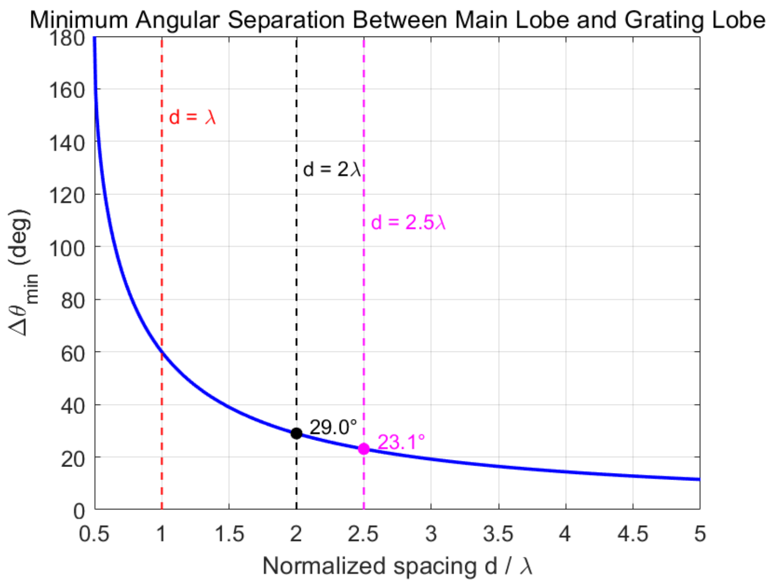

Figure 6.6: Minimum angular separation $\Delta\theta_{\mathrm{min}}$ between mainlobe and grating lobe versus normalized spacing d/λ.

6.2. Proposed Modified Configuration

Based on the previous analysis, the compression of the sidelobes observed with increasing element spacing d can be utilized to mitigate the sidelobe problem in a large baseline configuration. Although in the fine estimation stage the influence of grating lobes can be avoided by restricting the field of view (FOV), the coarse estimation stage inevitably requires a wide angular search range. Therefore, employing a highly sparse array with a large d would introduce strong grating lobes in the coarse estimation process, which is undesirable.

To address this issue, a modified array configuration is proposed, as illustrated in Fig. 6.7. In this design, the general baseline is maintained at 68λ with an inter-element spacing of $d = 2.5\lambda$. Between each pair of receiver subarrays, four additional receiver elements are uniformly inserted, forming three dense sub-apertures with $d = 0.5\lambda$ and six elements per subarray. This hybrid design combines the advantages of both dense and sparse spacings.

- During the **coarse estimation stage**, snapshots collected from dense sub-apertures ($d = 0.5\lambda$) are utilized. These subarrays exhibit low sidelobes and no grating lobes within the wide FOV, ensuring stable beamforming and reliable preliminary DOA estimation.
- During the **fine estimation stage**, only the snapshots corresponding to the sparse sub-apertures ($d = 2.5\lambda$) are used to achieve high angular resolution through coherent FOCUSS reconstruction.

Since a spacing of $d = 2.5\lambda$ results in a minimum angular separation between the mainlobe and the first grating lobe of approximately $23°$ (as derived from

$$\Delta\theta_{\mathrm{min}} = 2\arcsin\left(\frac{\lambda}{2d}\right), \tag{6.5}$$

), the FOV in the fine estimation stage is limited to $23°$ around each coarse estimate of the DOA. This ensures that the grating lobes do not enter the estimation window, maintaining accuracy while benefiting from the improved aperture of the sparse configuration.

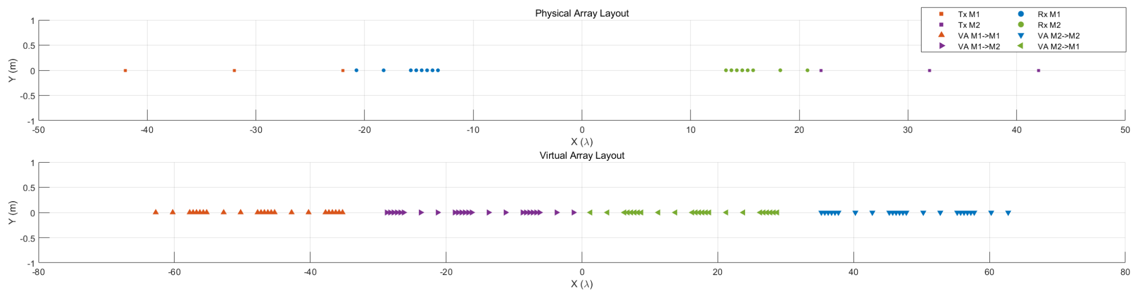

Figure 6.7: Proposed modified array configuration. Top: physical array layout; bottom: virtual array layout.

6.3. Results and Performance Evaluation

In this section, the proposed modified array configuration is evaluated through numerical simulations. The overall processing framework is summarized as follows: in the **coarse estimation stage**, three dense sub-apertures within the virtual array (each with spacing $d = 0.5\lambda$) are employed to obtain stable preliminary DOA estimates through beamforming; in the **fine estimation stage**, only the snapshots corresponding to the sparse sub-apertures ($d = 2.5\lambda$) are utilized for coherent FOCUSS reconstruction. This configuration effectively mitigates the sidelobe problem that occurs under a large baseline.

Figs. 6.8a–6.8c show the coherent DOA estimation results under the same baseline length ($L = 68\lambda$) but with different inter-element spacings of $d = 0.5\lambda$, 2λ, and 2.5λ, respectively. The two targets are located at $29°$ and $31°$. As d increases, the sidelobes are progressively compressed, and when $d = 2.5\lambda$, the sidelobe level is reduced to approximately -30 dB, which is within an acceptable range for accurate estimation.

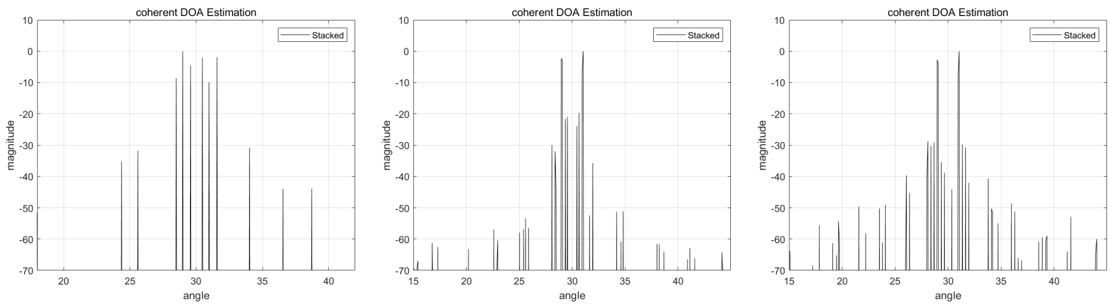

(a) $d = 0.5\lambda$ **(b)** $d = 2\lambda$ **(c)** $d = 2.5\lambda$

Figure 6.8: Results under a baseline of $L = 68\lambda$ for different element spacings d. Two targets are located at $29°$ and $31°$.

Next, the robustness of the proposed configuration is tested with targets of different radar cross-sectional (RCS) contrasts. Fig. 6.9a and Fig. 6.9b correspond to the RCS differences of 10 dB and 20 dB, respectively. Even under a large RCS difference, the proposed model still yields clearly distinguishable peaks, and the relative peak magnitudes accurately reflect the RCS ratio. Furthermore, the influence of sidelobes caused by the large baseline remains negligible.

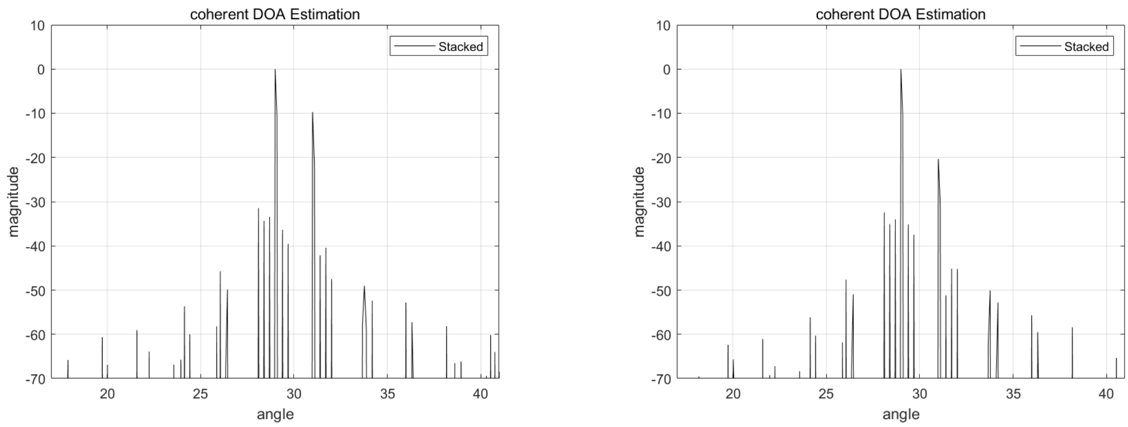

(a) RCS = 10 dB

(b) RCS = 20 dB

Figure 6.9: Results for $L = 68\lambda$, $d = 2.5\lambda$.

To further validate the effectiveness under an even larger aperture, the baseline is extended to $L = 100\lambda$. Figs . 6.10a and 6.10b show the results for two targets with RCS differences of 0 dB and 20 dB, respectively. Despite the significantly larger baseline, the proposed array still provides distinct peaks and remains robust to large RCS differences, confirming the scalability of the design.

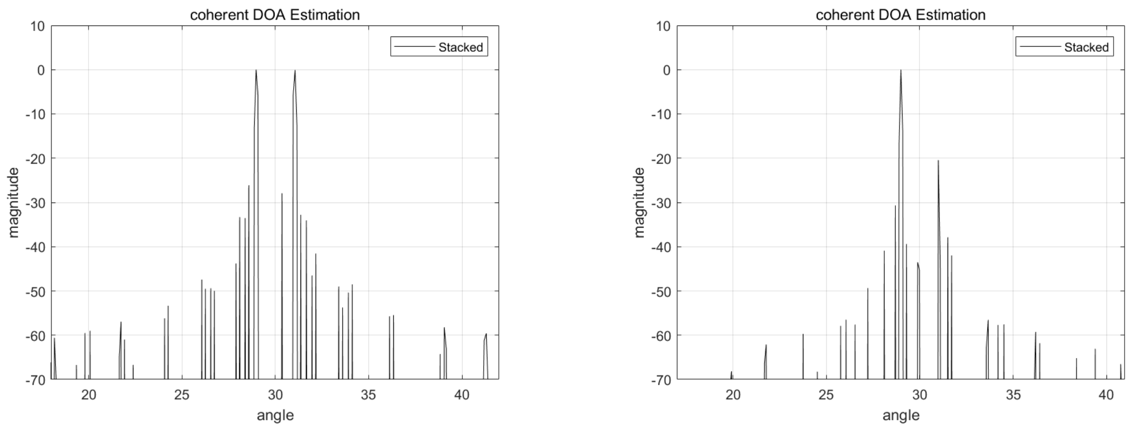

(a) RCS = 0 dB

(b) RCS = 20 dB

Figure 6.10: Results for $L = 100\lambda$, $d = 2.5\lambda$.

Finally, Figs. 6.11a and 6.11b compare the overall performance between the proposed modified array and the benchmark uniform linear array (ULA) model with half-wavelength spacing ($d = 0.5\lambda$), both using a baseline of $L = 68\lambda$. Fig. 6.11a shows the mean squared error (MSE) as a function of target separation, while Fig. 6.11b presents robustness metrics including probability of resolution (PR), probability of no false alarm ($1-\mathrm{PFA}$) and probability of successful association (PA). It can be observed that the modified array achieves significantly higher angular resolution—successfully resolving targets separated by as little as $0.1°$—while maintaining low reconstruction error and strong robustness against sidelobe interference. The only minor drawback is a slight reduction in coarse-stage association robustness due to shorter subarray apertures, along with a modest increase in hardware complexity.

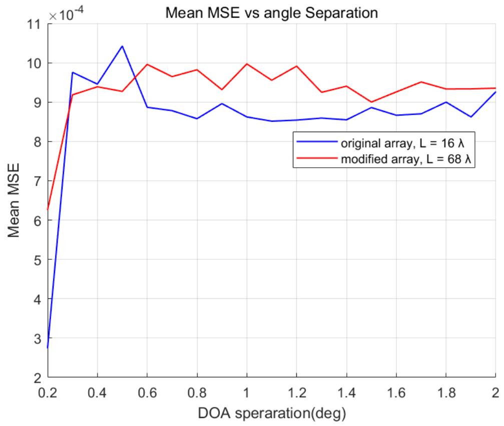

(a) MSE

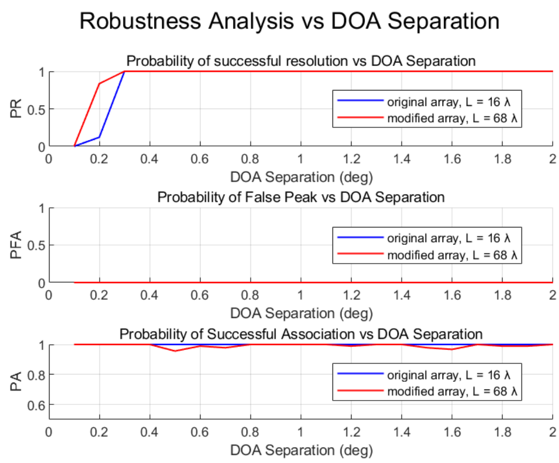

(b) Robustness

Figure 6.11: Comparison between the benchmark ULA and the proposed modified array ($L = 68\lambda$).

7
Conclusion

This thesis investigated high-resolution direction-of-arrival (DOA) estimation in distributed MIMO radar systems, with a particular focus on coherent and non-coherent sparse reconstruction, cross-radar phase alignment, and large-baseline aperture design. A two-stage processing framework was developed to achieve super-resolution performance while maintaining manageable computational complexity. The first stage performs coarse DOA estimation using conventional beamforming, followed by a range–velocity–geometry based data-association procedure that assigns snapshots from the four bistatic apertures to the underlying physical targets. The second stage refines the angular estimates using sparse reconstruction, with both non-coherent fusion (Block FOCUSS) and coherent fusion (phase-aligned FOCUSS) examined in depth.

Summary of Contributions

The main contributions of this thesis can be summarized as follows:

- **Two-stage DOA estimation framework.** A computationally efficient coarse-to-fine structure was proposed, enabling super-resolution DOA estimation without relying on a dense search grid or high-dimensional joint estimation.
- **Non-coherent and coherent sparse reconstruction models.** A complete formulation of Block FOCUSS and coherent FOCUSS was developed for distributed bistatic radar. The coherent model required a dedicated phase-synchronization and geometric phase-compensation derivation, allowing the four bistatic apertures to be coherently stacked into a unified virtual array.
- **Numerical stabilization for coherent fusion.** It was shown that coherent FOCUSS suffers from ill-conditioning when combining multiple sparse aperture responses. Three numerical remedies were introduced and evaluated: (i) adaptive regularization, (ii) normalization-based stabilization, and (iii) multi-grid reconstruction. Their impact on robustness, accuracy, and weak-target detectability was systematically analyzed.
- **Modified sparse–dense hybrid array for large baselines.** Although a large bistatic baseline improves nominal angular resolution, it results in severe non-uniformity and high sidelobe levels. A modified array configuration was proposed, introducing several locally dense sub-apertures that significantly suppress sidelobes in the coarse stage while retaining the wide aperture required for super-resolution in the fine stage.
- **Comprehensive simulation analysis.** Extensive Monte-Carlo simulations were conducted to evaluate the performance under various conditions—including target separation, range, SNR, RCS

imbalance, numerical stabilization, and baseline length—providing an in-depth comparison between coherent and non-coherent processing frameworks.

Key Findings

Several important conclusions emerged from this study:

- Non-coherent Block FOCUSS provides stable super-resolution performance and is robust to inter-radar phase misalignment, but its resolution is limited by the individual apertures and cannot exploit aperture diversity fully.
- Coherent FOCUSS achieves significantly higher resolution due to virtual aperture expansion, but requires precise phase alignment and careful numerical stabilization to avoid ill-conditioned reconstructions.
- The proposed modified sparse–dense hybrid array configuration effectively mitigates the severe sidelobe problem caused by large bistatic baselines and greatly improves coarse-stage reliability without compromising fine-stage super-resolution capabilities.
- Coarse-to-fine processing is demonstrated to be particularly suitable for distributed MIMO radar, as it constrains the search region, improves numerical conditioning, and reduces combinatorial ambiguity during data association.

7.1. Future Work

While the proposed models and methods provide a solid basis for high-resolution DOA estimation in distributed radar systems, several promising research directions remain.

1. Data Association and Multi-Target Sparse Reconstruction

The current data-association method, based on single-snapshot range–velocity–geometry consistency and enumeration of feasible combinations, is effective for a small number of targets but does not scale well. In multi-target scenarios, enumeration becomes computationally expensive, and the robustness of sparse reconstruction degrades, especially when adaptive regularization is applied in coherent FOCUSS—potentially suppressing weaker targets. Future work may incorporate more advanced multi-target association techniques such as probabilistic data association, optimal transport, or joint sparse reconstruction models that exploit multi-snapshot temporal structure.

2. Spatial Filtering in the Coarse-to-Fine Framework

In coarse-to-fine processing, the fine-stage reconstruction is limited to a narrow FOV. However, without proper spatial filtering, out-of-FOV targets, clutter, or noise can still affect sparse reconstruction. Traditional window-based spatial filtering has a limited effect on super-resolution methods such as FOCUSS because of their extremely narrow and discretized spectral peaks. Developing spatial filtering or interference-suppression mechanisms tailored to sparse reconstruction remains an open and valuable research topic.

3. Extension to Non–Point-Target Models

This thesis assumes point-target scattering. In realistic environments, objects such as vehicles or UAVs exhibit extended or distributed scattering, forming point clouds or angular spreads. Extending the proposed models to handle extended targets, scattering centers, or multi-path-induced angular clusters is essential for improving realism and applicability to advanced sensing tasks.

4. Full Experimental Verification

Due to time constraints, the complete experimental validation was not completed. Future work should focus on: (i) implementing the proposed algorithms on a hardware platform, (ii) validating phase synchronization and geometric compensation under real conditions, and (iii) conducting field experiments to evaluate robustness in the presence of clutter, multi-path, motion-induced distortion, and calibration errors. This verification is critical before deploying the framework in real systems.

Final Remarks

This thesis provides a unified view of coherent and non-coherent sparse DOA estimation in distributed bistatic MIMO radar and introduces a practical and effective framework capable of achieving super-resolution performance without excessive computational burden. The proposed hybrid array design and numerical stabilization strategies address several key challenges associated with large-baseline distributed sensing. The findings lay a foundation for further research towards scalable, robust, and physically realistic distributed radar systems.

References

[1] M. A. Richards, J. Scheer, and W. A. Holm. *Principles of Modern Radar, Volume I: Basic Principles*. Accessed: Nov. 17, 2025. Raleigh, NC: SciTech Publishing, 2010. URL: http://site.ebrary.com/id/10755684.

[2] Wogong Zhang et al. "A Unified 77/79GHz Low-Profile Digital Code Modulation (DCM) Automotive Radar Aiming at Mass Production". In: *2024 IEEE MTT-S International Wireless Symposium (IWS)*. 2024, pp. 1–3. DOI: 10.1109/IWS61525.2024.10713572.

[3] Ralph H. Rasshofer. "Functional requirements of future automotive radar systems". In: *2007 European Radar Conference*. 2007, pp. 259–262. DOI: 10.1109/EURAD.2007.4404986.

[4] Joachim Ender. "A brief review of compressive sensing applied to radar". In: *2013 14th International Radar Symposium (IRS)*. Vol. 1. 2013, pp. 3–16.

[5] Zhiwei Chen, Guochang Gokeda, and Yiqing Yu. *Introduction to Direction-of-Arrival Estimation*. Boston: Artech House, 2010. URL: https://ebookcentral.proquest.com/lib/uvic/detail.action?docID=583642.

[6] Francesco Belfiori, Wim van Rossum, and Peter Hoogeboom. "Coherent MUSIC technique for range/angle information retrieval: application to a frequency□modulated continuous wave MIMO radar". In: *IET Radar, Sonar & Navigation* 8.2 (Feb. 2014), pp. 75–83. DOI: 10.1049/iet-rsn.2013.0121.

[7] Matthias Weiß. "Distributed Sensor Systems". In: *NATO SET 235: Radar and SAR Systems for Airborne and Space-based Surveillance and Reconnaissance*. STO-EN-SET-235. Fraunhofer FHR, Germany: NATO Science and Technology Organization, 2021.

[8] Joachim H. G. Ender. "On compressive sensing applied to radar". In: *Signal Processing* 90.5 (2010), pp. 1402–1414. DOI: 10.1016/j.sigpro.2009.11.009.

[9] X. Zhang et al. "Direction of Departure (DOD) and Direction of Arrival (DOA) Estimation in MIMO Radar with Reduced-Dimension MUSIC". In: *IEEE Communications Letters* 14.12 (2010), pp. 1161–1163. DOI: 10.1109/LCOMM.2010.102610.101581.

[10] Xiaoming Liu et al. "Joint DOD and DOA Estimation Using 2-D Unitary ESPRIT for Bistatic MIMO Radar". In: *IEEE Signal Processing Letters* 23.10 (2016), pp. 1414–1418. DOI: 10.1109/LSP.2016.2592958.

[11] Neder Karmous, Mohamed Ould-Elhassen, and Fethi Choubani. "An Improved ESPRIT Algorithm for DOA Estimation of Coherent Signals". In: *2018 International Conference on Smart Antennas and Signal Processing (IC-SASP)*. Accessed via TU Delft Library. IEEE. 2018.

[12] Zhimin Chen and Peng Chen. "Compressed Sensing-Based DOA and DOD Estimation in Bistatic Co-Prime MIMO Arrays". In: *2017 IEEE International Conference on Antenna Measurements & Applications (CAMA)*. IEEE. 2017, pp. 297–300. DOI: 10.1109/CAMA.2017.8273412.

[13] Mobien Shoaib et al. "Comparison of DOA Algorithms for Target Localization in UCA FM Bi-Static Passive Radar". In: *2023 IEEE International Radar Conference (RADAR)*. IEEE. 2023, pp. 1–6. DOI: 10.1109/RADAR54928.2023.10371076.

[14] Anusha Ravish Suvarna. "Fusion of radar data from multiple MIMO systems to achieve higher angular resolution". Confidential until August 31, 2022. Master's thesis. Delft, The Netherlands: Delft University of Technology, 2021. URL: https://repository.tudelft.nl/.

[15] Yaqi Liu et al. "Three Dimensional Compressive Sensing in MIMO Radar". In: *Proceedings of the IEEE International Conference on Signal Processing, Communications and Computing (ICSPCC)*. IEEE. 2015, pp. 1–5. DOI: 10.1109/ICSPCC.2015.7338715.

[16] Ignacio Roldan et al. "Low Complexity Single-Snapshot DoA Estimation via Bayesian Compressive Sensing". In: *2023 IEEE Radar Conference (RadarConf23)*. IEEE. 2023, pp. 1–6. DOI: 10.1109/RADARCONF2351548.2023.10149589.

[17] M. Umut Bahçeci and Berkan Kılıç. "Transmitter and Receiver Design in Compressive Sensing based Direction of Arrival Estimation". In: *Proceedings of the 2023 European Radar Conference (EuRAD)*. Published under EurAAP license; also available via IEEE Xplore. EurAAP. 2023.

[18] Xiaowei Hu et al. "Fast SL0 Algorithm for 3D Imaging Using Bistatic MIMO Radar". In: *IET Signal Processing* 12.8 (2018), pp. 1017–1022. DOI: 10.1049/iet-spr.2017.0376.

[19] Wenhua Hu et al. "A Bistatic ISAR Sparse Aperture High Resolution Imaging Algorithm Based on ROMP Algorithm". In: *2019 IEEE 3rd Information Technology, Networking, Electronic and Automation Control Conference (ITNEC)*. IEEE. 2019, pp. 490–495. DOI: 10.1109/ITNEC.2019.8729431.

[20] Abdi T. Abdalla and Ali H. Muqaibel. "Single-view Bistatic Sparse Reconstruction in TWRI Exploiting Ghost's Aspect Dependence Feature". In: *2016 IEEE Wireless Communications and Networking Conference (WCNC)*. IEEE, 2016. DOI: 10.1109/WCNC.2016.7564742.

[21] Fuyu Lu et al. "FMCW SAR Imaging via Two-Dimension Hybrid OMP". In: *2021 IEEE International Conference on Signal Processing, Communications and Computing (ICSPCC)*. IEEE. 2021, pp. 1–5. DOI: 10.1109/ICSPCC52875.2021.9564488.

[22] Sangdong Kim, Daegun Oh, and Jonghun Lee. "Joint DFT-ESPRIT Estimation for TOA and DOA in Vehicle FMCW Radars". In: *IEEE Antennas and Wireless Propagation Letters* 14 (2015), pp. 1710–1713. DOI: 10.1109/LAWP.2015.2420579.

[23] Wanjun Zhi and Michael Yan-Wah Chia. "Near-Field Source Localization via Symmetric Subarrays". In: *IEEE Signal Processing Letters* 14.6 (June 2007), pp. 409–412. DOI: 10.1109/LSP.2006.888390.

[24] Jian Li and Petre Stoica. *MIMO Radar Signal Processing*. Hoboken, NJ, USA: Wiley–IEEE Press / John Wiley and Sons, 2008. ISBN: 978-0-470-17898-0. DOI: 10.1002/9780470391488.

[25] M. Chen et al. "Underdetermined passive localisation of emitters based on multi-step processing". In: *IET Radar, Sonar & Navigation* 11.11 (2017), pp. 1769–1776. DOI: 10.1049/iet-rsn.2017.0186.

[26] Thomas Lang and Darcy Dunne. "Application of particle filters in a hierarchical data fusion system". In: *2005 8th International Conference on Information Fusion*. 2005, 6 pp.–. DOI: 10.1109/ICIF.2005.1591893.

[27] Le Zheng, Yu Zhang, and Xiaodong Wang. "Feature-aided NN-JPDAF Algorithm for Multiple Target Tracking". In: *IEEE Transactions on Aerospace and Electronic Systems* 54.6 (2018), pp. 2677–2690. DOI: 10.1109/TAES.2018.2799780.

[28] M. Bekar, C. J. Baker, and M. S. Gashinova. "Distributed Automotive Radar Multi-Modal Sensing". In: *2021 IEEE Radar Conference (RadarConf21)*. 2021, pp. 1–6. DOI: 10.1109/RadarConf2147009.2021.9455205.

[29] I. F. Gorodnitsky and B. D. Rao. "Sparse Signal Reconstruction from Limited Data Using FOCUSS: A Re-weighted Minimum Norm Algorithm". In: *IEEE Transactions on Signal Processing* 45.3 (1997), pp. 600–616. DOI: 10.1109/78.558475.

[30] K. Xie, Z. He, and A. Cichocki. "Convergence Analysis of the FOCUSS Algorithm". In: *IEEE Transactions on Neural Networks and Learning Systems* 26.3 (2015), pp. 601–615. DOI: 10.1109/TNNLS.2014.2323985.

[31] Stefan Brisken and Joachim Ender. “Block-Sparse 3-D ISAR Image Reconstruction in a Non-Coherent Multistatic Scenario”. In: *2015 IEEE Radar Conference (RadarConf)*. IEEE. 2015, pp. 265–269. DOI: 10.1109/RADAR.2015.7131062.

[32] Per Christian Hansen. *Rank-Deficient and Discrete Ill-Posed Problems: Numerical Aspects of Linear Inversion*. Philadelphia, PA, USA: SIAM, 1998. DOI: 10.1137/1.9780898719697.

[33] T. Q. Xia et al. “Adaptive Regularized FOCUSS Algorithm”. In: *2007 IEEE International Conference on Acoustics, Speech and Signal Processing (ICASSP)*. IEEE. 2007, pp. 281–284. DOI: 10.1109/ICASSP.2007.366986.

[34] Jiacheng He et al. “Phase Correction Method for Coherent Processing of Quasi-coherent MIMO Radar Networks”. In: *2024 International Radar Conference (RADAR)*. IEEE. 2024. DOI: 10.1109/RADAR58436.2024.10993918.

[35] X. Zhu, G. Li, and M. Lin. “Window Function Design for Non-uniform MIMO Arrays”. In: *IEEE Transactions on Antennas and Propagation* 71.5 (2023), pp. 4123–4136. DOI: 10.1109/TAP.2023.3245678.

[36] J. Li, J. Zhang, and W. Liu. “Sidelobe Suppression for Time-domain Adaptive Broadband Beamforming with Sparse Constraint”. In: *IEEE Transactions on Audio, Speech, and Language Processing* 20.6 (2012), pp. 1689–1699. DOI: 10.1109/TASL.2012.2188336.

[37] S. Zhang, X. Zhang, and Z. Ye. “Robust Sidelobe Canceller Against DOA Mismatch”. In: *IEEE Transactions on Signal Processing* 63.2 (2015), pp. 437–447. DOI: 10.1109/TSP.2014.2368123.